Synthesis and Electrochemical Characterization of Magnesium-Ion Battery Electrolytes

by

Adam J. Crowe

A dissertation submitted in partial fulfillment
of the requirements for the degree of
Doctor of Philosophy
(Chemistry)
in the University of Michigan
2019

Doctoral Committee:

Professor Bart Bartlett, Chair
Professor Nicolai Lehnert
Professor Stephen Maldonado
Assistant Professor Nirala Singh

Adam J. Crowe

ajcrowe@umich.edu

ORCID iD: 0000-0001-5364-8909

Dedication

To Alexandria, Tamara, and John Crowe.

Acknowledgements

Alex, thank you for making everything easy. With you I know there will always be someone on my side, supporting me through difficult times. Mom and Dad, you are the two greatest role models that I could ever ask for and I am forever grateful for the sacrifices that you made for me. Your hard work and determination will always be something I admire. Without your love and support none of this would be possible, thank you.

Bart, thank you for providing me with the opportunity to work within your group. You taught me not only how to approach difficult science questions but how to communicate the results more effectively. I cannot thank you enough for your patience and extensive feedback that you have provided me during my graduate studies. I would also like to thank the rest of my committee for their guidance throughout the years– Professor Lehnert, Professor, Maldonado, Professor Singh, and Professor Thompson.

Professor Allen– thank you introducing me to research during my undergraduate studies and always pushing me to become a better chemist. I extremely grateful for the assistance you provided as I prepared to begin my graduate studies. I would also like to thank Dr. Akhila Kuda-Wedagedara for providing my initial training and mentorship during my time in the Allen group. My preparation for graduate school was largely due to our time spent together.

I am grateful for the opportunity to work with outstanding scientists during the past few years. Emily, thank you for the guidance during my first years here at the University of Michigan as well as your pioneering work on magnesium-ion battery electrolytes within our group. John you are an outstanding scientist and an even better friend. I am forever grateful for your patience

while you passed on your electrochemistry expertise. Thank you for all of the edits and feedback that you provided through the years. Kyle, your hard work and eagerness to learn was inspiring and I truly enjoyed the time we had to work together. Ben, Kayla, Charles, Jimmy, and Sam– thank you for the helpful suggestions and guidance that you all provided during my initial years within the group. Aaron, Andy, Kori, Brad, and Christian– thank you for the helpful science (and non-science) discussions. It was a great feeling to know there were always people I could talk to. I will sincerely miss working alongside all of you.

Table of Contents

Dedication ii

Acknowledgements iii

List of Tables viii

List of Figures ix

Abstract xiv

Chapter 1 Introduction 1

1.1 Renewable Energy Storage 1

1.2 Current and Future Rechargeable Battery Technologies 2

1.3 Magnesium-Ion Battery Electrolytes 6

1.4 Solid State Cathode Materials for Secondary Magnesium-Ion Batteries That Are Compatible with Magnesium Metal Anodes in Water-Free Electrolyte 7

1.4.1 Mo_6S_8 8

1.4.2 MoS_2 10

1.4.3 WSe_2 12

1.4.4 MoO_3 14

1.4.5 α-MnO_2 14

1.5 Outline 16

1.6 References 16

Chapter 2 Influence of Steric Bulk on the Oxidative Stability of Phenolate-Based Magnesium-Ion Battery Electrolytes 22

2.1 Introduction 22

2.2 Experimental 23

2.2.1 Synthesis of Electrolyte Solutions 23

2.2.2 Electrolyte Solution Characterization 24
2.2.3 Electrochemical Cell Preparation and Measurements 25
2.3 Results and Discussion 25
2.3.1 *Para*-Alkyl Substituted Phenolate-Based Electrolyte Solutions 25
2.3.2 Effect of *Ortho*-Substituents on *Para*-Alkyl Substituted Phenolate-Based Electrolyte Solutions 28
2.3.3 Electrochemical Cycling of Chevrel-phase Mo_6S_8 vs Mg-foil in 0.5 M ^{R}PhOMgCl (R = 2,4,6-Me_3) and 0.25 M $AlCl_3$ electrolyte in THF 31
2.4 Conclusion 33
2.5 References 33
Chapter 3 Fluorinated Alkoxide-Based Magnesium-Ion Battery Electrolytes that Demonstrate Li-Ion-Battery-Like High Anodic Stability and Solution Conductivity 35
3.1 Introduction 35
3.2 Experimental 36
3.2.1 DFT Calculations 36
3.2.2 Synthesis of Electrolyte Solutions 37
3.2.3 Electrolyte Solution Characterization 37
3.2.4 Electrochemical Cell Preparation and Measurements 38
3.3 Results and Discussion 39
3.3.1 Density Functional Theory Guided Electrolyte Design 39
3.3.2 Effect of Fluorination on Solution Speciation and Electrochemical Stability 42
3.3.3 The Role of Solvation on Solution Speciation and Electrochemical Properties 47
3.3.4 Electrochemical Cycling of Chevrel-phase Mo_6S_8 vs Mg-foil in 1.2 M $((CF_3)_2(CH_3))COMgCl$ and 0.2 M $AlCl_3$ in THF 49
3.4 Conclusions 51
3.5 References 52
Chapter 4 Kinetics of Magnesium Deposition and Stripping from Non-Aqueous Electrolytes 55
4.1 Introduction 55
4.2 Experimental 56

4.2.1 Synthesis of Electrolyte Solutions 56
4.2.2 Electrolyte Solution Characterization 57

4.3 Results and Discussion 58

4.3.1 Tafel Analysis of Magnesium Deposition-Dissolution 60
4.3.2 Morphology and X-Ray Diffraction of Mg^0 Deposits 61
4.3.3 Estimation of Cationic Transference Numbers 67
4.3.4 Electrochemical Impedance Spectroscopy of Magnesium Electrodeposition 69
4.3.5 Electrochemical Studies on Diluted F_6-*t*-Butoxide Electrolyte Solutions 73

4.4 Conclusions 75

4.5 References 76

Chapter 5 Adsorption of Aromatic Decomposition Products from Phenyl-Containing Magnesium-Ion Battery Electrolyte Solutions 78

5.1 Introduction 78

5.2 Experimental 79

5.2.1 Synthesis of Electrolyte Solutions 79
5.2.2 Electrolyte Solution Characterization 79

5.3 Results and Discussion 81

5.3.1 Electrochemical Analysis of PhMgCl Containing Solutions 81
5.3.2 Chemical Identity of Adsorbed Decomposition Products 86
5.3.3 Charge-Transfer Properties of Adsorbed Species on Working Electrode Surfaces 95

5.4 Conclusion 98

5.5 References 99

Chapter 6 Conclusions and Potential Future Directions 101

6.1 Summary of Presented Work 101

6.2 Determination of Electrochemically Active Species 102

6.3 Magnesium Metal Conditioning to Pre-Generate a Mg^{2+} Permeable Solid-Electrolyte Interphase (SEI) 103

6.4 Summary and Concluding Remarks 107

6.5 References 108

List of Tables

Table 1.1. Parameters for cathode material performance. 8

Table 2.1. Anodic stability (potential vs $Mg^{2+/0}$), conductivity, Taft's steric substituent constant and Coulombic efficiency for deposition–dissolution of *para*-substituted (top) and multi-substituted phenol-based electrolytes (bottom). 28

Table 3.1. Summary of HOMO, LUMO, and energy difference in eV for organochloroaluminates in THF. 42

Table 3.2. Anodic stability (potential vs $Mg^{2+/0}$), solution conductivity, and Coulombic efficiency for deposition–dissolution of the fluorinated alkoxide-based electrolytes. 43

Table 4.1. Compilation of electrochemical values determined through Tafel analysis. 60

Table 4.2. Compilation of transference values 67

Table 4.3. Fits to the EIS model circuit while holding a Pt-disk working electrode at −1 V (vs $Mg^{2+/0}$). 69

List of Figures

Figure 1.1. Standard configuration for an intercalation-based electrochemical cell. Device represented in fully discharged state with ions (black spheres) occupying insertion sites within the solid-state cathode material (blue and yellow spheres). 2

Figure 1.2. Energy diagram of an electrochemical cell, depicting the thermodynamic stability window of the electrolyte before and after SEI layer formation. 4

Figure 1.3. Magnesium intercalation cavities within CP-Mo_6T_8. Reprinted (adapted) with permission from Ref. 36. Copyright (2009) American Chemical Society. 9

Figure 1.4. (a) Capacity vs cycle number and (b) capacity vs rate curves of various $Mg_xMo_6S_{8-y}Se_y$ (y=0, 1, 2). Reprinted (adapted) with permission from Ref. 26. Copyright (2007) WILEY-VCH Verlag GmbH & Co. KGaA, Weinheim. 10

Figure 1.5. Theoretical model of Mg^{2+} intercalation within a MoS_2 single-layered nano-ribbon. Reprinted (adapted) with permission from Ref. 41. Copyright (2011) WILEY-VCH Verlag GmbH & Co. KGaA, Weinheim. 11

Figure 1.6. Cycling behavior of G-MoS_2 (graphene-like MoS_2), N-Mg (magnesium nanoparticle anode), B-MoS_2 (bulk MoS_2), and B-Mg (bulk magnesium). Reprinted (adapted) with permission from Ref. 41. Copyright (2011) WILEY-VCH Verlag GmbH & Co. KGaA, Weinheim. 12

Figure 1.7. Comparison of cycling behavior between bulk WSe_2 and WSe_2 nanowire-based electrodes. Reprinted (adapted) with permission from Ref. 45. Copyright (2013) American Chemical Society. 13

Figure 1.8. Structure of MoO_3 viewed along [0 1 0]. 14

Figure 1.9. Structure of α-MnO_2 viewed along [0 1 0]. 15

Figure 2.1. Cyclic voltammograms of 0.5 M ^{R}PhOMgCl and 0.25 M $AlCl_3$ (R = 4-Me, 4-Et, 4-^{i}Pr, 4-^{s}Bu, and 4-^{t}Bu). 26

Figure 2.2. ^{27}Al NMR chemical shifts and assignments for 0.5 M ^{R}PhOMgCl and 0.25 M $AlCl_3$ (R = 4-Me, 4-Et, 4-^{i}Pr, 4-^{s}Bu, and 4-^{t}Bu) in THF: 74 ppm $[(^{R}PhO)_2AlCl_2]^-$, 87 ppm $[(^{R}PhO)AlCl_3]^-$, and 102 ppm Al_2Cl_6. 26

Figure 2.3. Anodic stability defined as the potential for the onset of 5 μA anodic current vs Taft's steric bulk parameter ($-E_s$) of *para*-substituted phenols (relative to unsubstituted phenol). The linear fit is shown in red. 27

Figure 2.4. Cyclic voltammograms of 0.5 M ^{R}PhOMgCl and 0.25 M $AlCl_3$ electrolyte solutions, substitutions designated in the figure legend. 30

Figure 2.5. ^{27}Al NMR chemical shifts and assignments for 0.5 M ^{R}PhOMgCl and 0.25 M $AlCl_3$ (R = 2,4,6-Me_3 and 2,6-Me_2) in THF: 42 ppm $[(^{R}PhO)_4Al]^-$, 55 ppm $[((^{R}PhO)_3AlCl]^-$, 68 ppm $[(^{R}PhO)_2AlCl_2]^-$, and 84 ppm $[((^{R}PhO)AlCl_3]^-$. 30

Figure 2.6. ^{27}Al NMR chemical shifts and assignments for 0.5 M ^{R}PhOMgCl and 0.25 M $AlCl_3$ (R = 2,4,6-$^{t}Bu_3$ and 2,6-$^{t}Bu_2$) in THF: 79 ppm $[((^{R}PhO)AlCl_3]^-$. 31

Figure 2.7. Reversible galvanostatic cycling of Mo_6S_8 vs Mg-foil at *C*/10 in 0.5 M ^{R}PhOMgCl and 0.25 M $AlCl_3$ (R = 2,4,6-Me_3) in THF electrolyte. 32

Figure 2.8. Charge–discharge curves of Mo_6S_8 vs Mg-foil in 0.5 M ^{R}PhOMgCl and 0.25 M $AlCl_3$ (R = 2,4,6-Me_3) in THF electrolyte at *C*/10. 32

Figure 3.1. Anodic stability vs calculated HOMO of $ROAlCl_3^-$ in THF for our previously reported electrolytes. 39

Figure 3.2. (a) Visualization of the HOMO for $^{R}PhOAlCl_3^-$ (R = 2,4,6-Me_3), and (b) $((CF_3)_2(CH_3))COAlCl_3^-$. 40

Figure 3.3. Lewis structures of alkoxide precursors. 41

Figure 3.4. Cyclic voltammograms of the optimized concentrations for R = 1–3-CF_3 electrolyte solutions in THF. 43

Figure 3.5. (a) SEM image and (b) EDX spectrum of deposited magnesium on Cu foil from 1.2 M$((CF_3)_2CH_3)COMgCl$ and 0.2 M $AlCl_3$ in THF electrolyte at 2 mA cm^{-2} (0.8 C cm^{-2}). 44

Figure 3.6. ^{27}Al NMR chemical shifts and assignments for THF solutions composed of (a) 0.8 M $((CF_3)(CH_3)_2)COMgCl$ and 0.13 M $AlCl_3$: 68 $[(^{R3}CO)_4Al]^-$; (b) 1.2 M $((CF_3)_2(CH_3))COMgCl$ and 0.2 M $AlCl_3$: 71 $[(^{R3}CO)_3AlCl]^-$, 65 $[(^{R3}CO)_4Al]^-$, and 62 $AlCl_3$; (c) 1.2 M $((CF_3)_3)COMgCl$ and 0.2 M $AlCl_3$: 78 $[(^{R3}CO)_2AlCl_2]^-$ and 61 $[(^{R3}CO)_4Al]^-$. 45

Figure 3.7. Cyclic voltammogram of varied concentration of *y* M $((CF_3)_2CH_3COMgCl)$ and *y*/6 M $AlCl_3$ (*y* = 0.8, 0.6, and 0.4 M) in THF solutions, as designated in the figure legend. 46

Figure 3.8. ^{27}Al NMR chemical shifts and assignments for *y* M $((CF_3)_2(CH_3))COMgCl$ and *y*/6 M $AlCl_3$ (*y* = 0.8, 0.6, and 0.4 M) in THF: 71 $[(^{R3}CO)_3AlCl]^-$, 65 $[(^{R3}CO)_4Al]^-$, and 62 $AlCl_3$. . 47

Figure 3.9. Comparison of cyclic voltammograms of 1.2 M $(CF_3)_2CH_3COMgCl$ and 0.2 M $AlCl_3$ in THF and 75% THF and 25% 2-methyl-THF solutions. 48

Figure 3.10. ^{27}Al NMR chemical shifts and assignments for 1.2 M $((CF_3)_2(CH_3))COMgCl$ and 0.2 M $AlCl_3$ in 75% THF and 25% 2-methyl-THF solution: 71 $[(^{R3}CO)_3AlCl]^-$, 65 $[(^{R3}CO)_4Al]^-$, and 62 $AlCl_3$..... 49

Figure 3.11. (a) Chronopotentiometric charge–discharge curves for a 2016 Mg coin-cell composed of 1.2 M $((CF_3)_2(CH_3))COMgCl$ and 0.20 M $AlCl_3$ in THF solvent and (b) data plotted as gravimetric capacity. 50

Figure 4.1. Structures of electrolyte components used in this work. 56

Figure 4.2. Cyclic voltammogram traces recorded using a Pt-disk working electrode of F_6-*t*-butoxide (black), 2,4,6-Me_3 phenolate (red), and APC (blue). 59

Figure 4.3. Tafel plot for Mg deposition and stripping from F_6-*t*-butoxide (black), 2,4,6-Me_3 phenolate (red), and APC (blue) electrolyte solutions in THF. 60

Figure 4.4. SEM images of Mg^0 deposits from F_6-*t*-butoxide (a and b), APC (c and d), and 2,4,6-Me_3 phenolate (e and f) solutions in THF..... 62

Figure 4.5. Cross-sectional SEM image of Mg^0 deposits from F_6-*t*-butoxide electrolyte in THF. 62

Figure 4.6. SEM images of Mg^0 deposits from (a) 0.5 M ^{R}PhOMgCl and 0.25 M $AlCl_3$ where R = 4-CF_3, (b) 0.5 M ^{R}PhOMgCl and 0.25 M $AlCl_3$ where R = 4-F, and (c) 0.4 M ^{R}PhMgCl and 0.2 M $AlCl_3$ where R = 4-F..... 63

Figure 4.7. X-ray diffraction patterns of Mg deposits from F_6-*t*-butoxide (black), 2,4,6-Me_3 phenolate (red), and APC (blue). The Cu-foil substrate (green) is presented for reference. 64

Figure 4.8. Pole figures about the (100) diffraction plane for Mg^0 deposits resulting from (a) F_6-*t*-butoxide, (b) APC, and (c) 2,4,6-Me_3 phenolate. The highest diffraction intensity is shown in red. 65

Figure 4.9. Pole figures collected about the (101), (002) and (110) for (a) F_6-*t*-butoxide, (b) APC, and (c) 2,4,6-Me_3 phenolate. The highest diffraction intensity is shown in red. 66

Figure 4.10. Nyquist plots of EIS results obtained using a Pt-disk working electrode of F_6-*t*-butoxide (black), 2,4,6-Me_3 phenolate (red), and APC (blue). The gray lines represent fits to the data using the model circuit illustrated in the inset..... 69

Figure 4.11. Nyquist plots of EIS results obtained using a bare Pt-disk (black) and a pre-treated Pt-disk electrode (red) of F_6-*t*-butoxide, including the fit (gray). 71

Figure 4.12. Cyclic voltammogram traces recorded using a Pt-disk working electrode of the diluted F_6-*t*-butoxide solutions, concentrations designated within the figure legend..... 72

Figure 4.13. Nyquist plots of EIS results obtained using a Pt-disk working electrode of diluted F_6-*t*-butoxide electrolyte solutions, concentrations designated within the figure legend, including the fit (gray). 73

Figure 4.14. Tafel plot for Mg deposition and stripping from diluted F_6-*t*-butoxide solutions, concentrations designated within the figure legend. 74

Figure 5.1. Cyclic voltammogram traces recorded using a Pt-disk working electrode of (a) 0.5 M PhMgCl and 0.125 M $Al(OPh)_3$ in THF and (b) 0.4 M PhMgCl and 0.2 M $AlCl_3$ in THF. Cycles 1 (black), 5 (red), and 10 (blue) are illustrated. 82

Figure 5.2. Cyclic voltammogram traces recorded using a Pt-disk cycled between –1 and 1.5 V (vs $Mg^{2+/0}$) of 0.5 M PhMgCl and 0.125 M $Al(OPh)_3$ in THF solution at cycle 1 (black) and 5 (red) and 10 (blue). 83

Figure 5.3. Cyclic voltammogram traces recorded using a Pt-disk of 0.5 M PhMgCl and 0.125 M $Al(OPh)_3$ in THF after soaking for 22 h in 0.5 M PhMgCl and 0.125 M $Al(OPh)_3$ in THF at open circuit. 83

Figure 5.4. Cyclic voltammogram traces recorded using a Pt-disk working electrode of (a) 0.5 M PhMgCl and 0.25 M $MgCl_2$ in THF and (b) 0.5 M PhMgCl in THF. Cycles 1 (black), 5 (red), and 10 (blue) are illustrated. 85

Figure 5.5. Cyclic voltammogram traces recorded using a Pt-disk working electrode of 0.5 M EtMgCl in THF solution at cycle 1 (black) and 5 (red) and 10 (blue). 86

Figure 5.6. Possible degradative pathway resulting in the adsorption of aromatic species. 87

Figure 5.7. Cyclic voltammogram traces recorded using a Pt-disk working electrode of PhMgCl–$AlCl_3$ with the addition of PhLi at cycles 1 (black) and 2 (red). 88

Figure 5.8. Cyclic voltammogram traces recorded using a glassy carbon disk working electrode of 0.5 M PhMgCl and 0.125 M $Al(OPh)_3$ in THF. Cycles 1 (black), 5 (red), and 10 (blue) are illustrated. 89

Figure 5.9. Raman spectroscopy of Pt-disk electrodes post 4 V (vs $Mg^{2+/0}$) for 16 hours within 0.5 M PhMgCl (black), 0.5 M PhMgCl and 0.125 M $Al(OPh)_3$ (red), 0.5 M PhMgCl and 0.25 M $MgCl_2$ (blue), and 0.4 M PhMgCl and 0.2 M $AlCl_3$ (green) in THF solutions. 90

Figure 5.10. ^1H NMR spectrum from the dissolved electrode decomposition products on Pt-disk electrodes. (a) Full spectrum, (b) increased baseline to show low concentration aromatic product. 91

Figure 5.11. ^1H–^1H COSY NMR spectrum from the dissolved electrode decomposition products on Pt-disk electrodes. 91

Figure 5.12. Cyclic voltammogram traces using a passivated Pt-disk, generated from a 4 V (vs $Mg^{2+/0}$) electrolysis for 5 minutes, after soaking 72 hours in 0.5 M PhMgCl and 0.125 M $Al(OPh)_3$ (red) and in neat THF (black). 92

Figure 5.13. GPC traces of dissolved electrolysis products resulting from PhMgCl containing electrolyte solutions on Pt-disk electrodes (black, red, and navy) and glassy carbon disk electrodes (green, violet, orange) post 3 hour electrolysis..... 93

Figure 5.14. (a) Electrolysis profile of a 5 minute, 4 V (vs $Mg^{2+/0}$), electrolysis and (b) GPC traces of dissolved electrolysis products resulting from PhMgCl containing electrolyte solutions on Pt-disk electrodes (black, red, and navy) and glassy carbon disk electrodes (green, violet, orange) post 5 minute electrolysis. 94

Figure 5.15. AC impedance spectroscopy results obtained using a (a) Pt-disk electrode and (b) glassy carbon-disk electrode in THF solutions of 0.4 M PhMgCl and 0.2 M $AlCl_3$ poised at 3.5 V (vs $Mg^{2+/0}$). Data from a pristine electrode are shown in black. Other electrodes were pre-electrolyzed in solutions of 0.5 M PhMgCl and 0.125 M $Al(OPh)_3$ (red), 0.5 M PhMgCl and 0.25 M $MgCl_2$ (blue), and 0.5 M PhMgCl (green). 96

Figure 5.16. SEM images of Pt-foil post 4 V (vs $Mg^{2+/0}$) electrolysis from THF solutions composed of (a) 0.5 M PhMgCl and 0.125 M $Al(OPh)_3$, (b) 0.5 M PhMgCl and 0.25 M $MgCl_2$, and (c) 0.5 M PhMgCl. 97

Figure 5.17. Bode Plots of bare Pt-disk (black, OCP 1.8 V vs $Mg^{2+/0}$) and bare glassy carbon disk (red, OCP 1.6 V vs $Mg^{2+/0}$) electrodes at their respective open circuit potentials. 97

Figure 6.1. SEM images of Mg working electrodes prior to cycling (left), after cycling between -3 and 1.5 V (vs Pt) in 0.5 M $Mg(ClO_4)_2$ (middle) and -3.5 and 1 V (vs Pt) in 1 M $LiPF_6$ (right). 105

Figure 6.2. Nyquist plots of EIS results obtained from an untreated Mg (black), pretreated $Mg_{Mg(ClO4)2}$ (red), and pretreated Mg_{LiPF6} (blue) when poised about –1 V vs $Mg^{2+/0}$ within 0.4 M PhMgCl and 0.2 M $AlCl_3$ in THF; applied frequencies 1 MHz–1 Hz..... 106

Abstract

Magnesium-ion batteries are thought to be a viable successor to the current Li-based systems owing to high elemental abundance (Mg, 2.3%), environmental benignity, and a two-fold volumetric capacity increase over lithium metal. However, moving beyond today's lithium-ion technology requires advances in fundamental electrolyte science as magnesium-based congeners of the typical salts and solvents used in Li-ion electrolyte solutions result in electrode passivation, which ceases any reversible battery cycling.

Initial magnesium-ion electrolyte solutions were composed of Grignard reagents such as PhMgCl, due to their ability to electrochemically deposit magnesium. Unfortunately the widespread use in battery manufacturing remains hindered by air and moisture sensitivity. With this limitation in mind, researchers began to investigate phenolate-based electrolyte solutions, which show reduced deleterious reactivity with air and moisture. With the systematic substitution of both the nature and number of substituents about the aromatic ring within the standard 0.5 M ^{R}PhOMgCl and 0.25 M $AlCl_3$ in tetrahydrofuran (THF) solvent, two design principles were determined: (1) electron withdrawing groups increase anodic stability and (2) increasing steric bulk of the organic moiety improves solution conductivity. While focusing entirely on sterics, an electrolyte solution starting from 2,4,6-trimethylphenol exhibits high solution conductivity (2.56 mS/cm).

Guided by the aforementioned design principles and density functional theory calculations, a series of highly soluble fluorinated alkoxide-based electrolytes were prepared, examined electrochemically, and reversibly cycled. Most notably, the electrolyte composed of

1.2 M $((CF_3)_2CH_3)COMgCl$ and 0.2 M $AlCl_3$ in THF (F_6-*t*-butoxide) exhibits high anodic stability (3.2 V vs $Mg^{2+/0}$) and solution conductivity (3.5 mS/cm). Additionally, the F_6-*t*-butoxide solution shows excellent galvanostatic cycling and capacity retention (94%) with more than 300 h of cycle time while employing the standard Chevrel phase-Mo_6S_8 cathode material. Overall, suggesting that fluorinated alkoxide-based electrolytes are promising candidates for practical high voltage magnesium-ion batteries.

The resulting electrode-electrolyte interface was further examined for three magnesium-ion electrolyte solutions to understand the influence an *in situ* deposited Mg layer has on continued electrodeposition. Comparing the deposition morphologies of three previously reported electrolyte solutions, the F_6-*t*-butoxide solution shows the most uniform and crystalline deposits growing along [100], normal to the electrode surface. Overall, this work illustrates that sporadic deposition and lower solution conductivities of the phenolate- and Grignard-based electrolytes hinder the deposition rate.

Additionally, a thorough investigation of possible decomposition products formed from a series of solutions containing PhMgCl in THF was performed. Solutions containing no additional salt, as well as those containing added $MgCl_2$ or $Al(OPh)_3$, demonstrate an initial anodic current response between 2 and 4 V (vs $Mg^{2+/0}$) which results in the adsorption of an aromatic polymer decomposition product on the working electrode surface. Once this adsorbed layer is formed, electrode impedance increases by ~100 Ω with no additional growth of the insulating film. A phenyl radical is deemed the culprit, as adding a phenyl anion source (Ph^-) insulates electrodes even for originally non-passivating electrolyte solutions. Overall, this work highlights many of the key advancements in electrolyte design and magnesium electrodeposition as well as presents

many of the remaining challenges for continued development of magnesium-ion battery technology.

Chapter 1

Introduction

Portions of this chapter have been published:

Crowe, A. J.; Bartlett, B. M. *J. Solid State Chem.* **2016**, *242*, 102–106.

1.1 Renewable Energy Storage

While the combustion of fossil fuels has and continues to provide suitable energy for many residential and industrial applications, the rate for exploitation surpasses that of formation.[1,2] With this disparity in the rates of generation and consumption of fossil fuels, developing new sustainable forms of energy continues to be of interest. This is especially true considering the world energy consumption is expected to grow 28% by 2040.[3] Continued reliance on coal-based fuels as our primary source of electricity generation[4] will continue to produce global warming contributing greenhouse gases. Specifically, every kWh of electricity generated from burning coal coproduces an average of 1 kg lifecycle CO_2 emission.[5,6] While solar and wind are two leaders for zero-emission sources of electricity for meeting the energy demands of our future society, their intermittent behavior requires the development of novel high energy storage technologies.[7] Of the proposed energy storage systems, electrochemical energy storage offers many desirable features such as pollution-free operation, the ability to manipulate power and energy characteristics for different applications, long cycle life and low maintenance.[8]

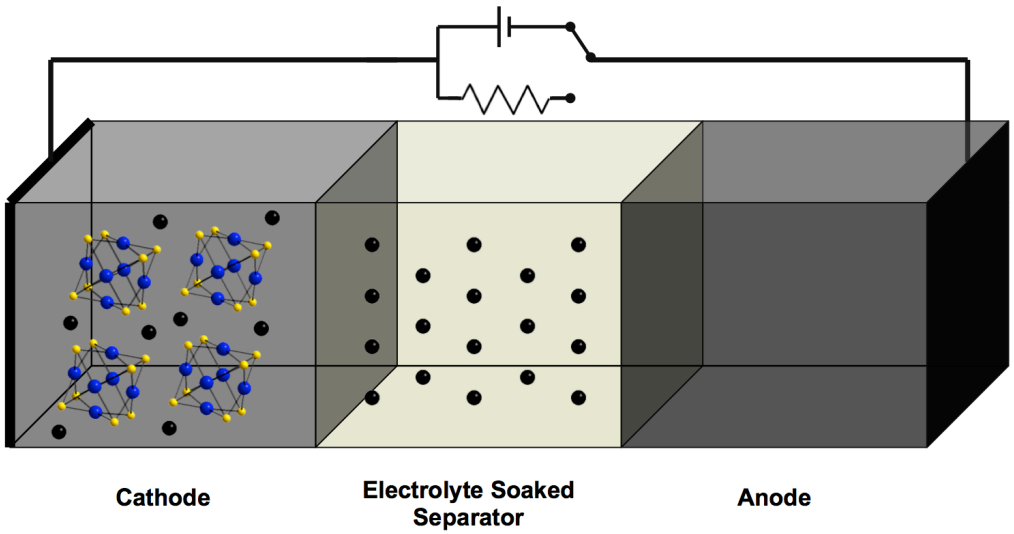

Figure 1.1. Standard configuration for an intercalation-based electrochemical cell. Device represented in fully discharged state with ions (black spheres) occupying insertion sites within the solid-state cathode material (blue and yellow spheres).

1.2 Current and Future Rechargeable Battery Technologies

Batteries are devices constructed from several electrochemical cells connected in series and/or parallel to provide a desired voltage and capacity, respectively, that store chemical energy and convert it to electrical energy. A secondary cell has the additional ability to be recharged, as electrical energy can drive chemical reactions to store chemical energy. Since Gaston Planté invented the rechargeable lead-acid battery in 1859, batteries have been deeply rooted within society.[9] While there have been considerable improvements made for the internal battery design since the original lead coils separated by sulfuric acid soaked linen, lead-acid systems remain the prevalent battery within automobiles for starting, lighting, and ignition. However, the environmental hazard due to the large presence of lead and relatively low energy density (approximately 90 Wh/L) requires further development of electrochemical energy systems.[10,11] Another example are intercalation-based systems, which currently power devices ranging from portable electronics to hybrid electric vehicles. The standard configuration of these

electrochemical cells is similar to the lead-acid cell discussed previously: two electrodes (cathode and anode) separated by an electrolyte soaked membrane (Figure 1.1).

Once a charged device is connected through an external circuit, chemical reactions proceed at each electrode simultaneously with the subsequent flow of electrical charge. Here, electrons leave the anode via an external circuit where they do useful work before reducing the cathode material as subsequent ion intercalation occurs. For standard Li-ion batteries employing a $LiCoO_2$ cathode and graphite anode, the half-reaction occurring at the cathode (equation 1), anode (equation 2), and overall reaction (equation 3) can be described by the following equations:

$$(1)\ Li_{1-x}CoO_2 + xLi^+ + xe^- \rightleftharpoons LiCoO_2$$

$$(2)\ Li_xC_6 \rightleftharpoons 6C + xLi^+ + xe^-$$

$$(3)\ Li_{1-x}CoO_2 + Li_xC_6 \rightleftharpoons LiCoO_2 + 6C$$

As outlined above, current rechargeable Li-ion cells require intercalation-deintercalation processes to occur at both the cathode and anode. Attempts to develop rechargeable Li-based cells employing a metallic anode have been unsuccessful as dendritic deposition of Li metal during charging results in short-circuiting of the device.[12]

Performance of an electrochemical cell can be quantified by the amount of electrical energy stored per weight (Wh/kg) or volume (Wh/L). As a result, we can increase this stored energy by increasing the chemical potential between the electrodes, decreasing the mass (or volume) of the reactants per transferred electron, and employing electrolyte solutions that are not consumed during use.[13] Further evaluation of an electrochemical cell is possible by highlighting the electrochemical potentials, where μ_A and μ_c correspond to the electrochemical potential of the

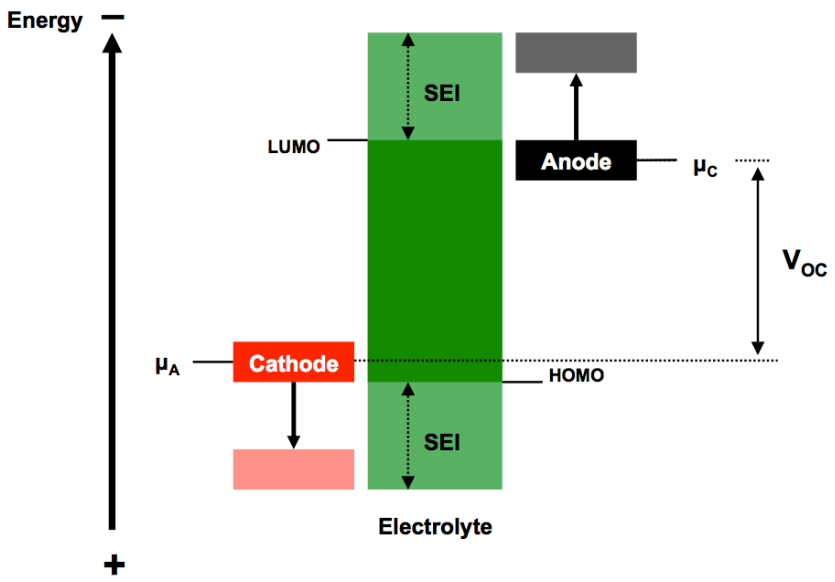

Figure 1.2. Energy diagram of an electrochemical cell, depicting the thermodynamic stability window of the electrolyte before and after SEI layer formation.

anode and cathode, respectively, within an energy diagram (Figure 1.2). As observed within the schematic, the cathode has a more positive electrochemical potential than the anode and therefore during discharge reduction of the cathode and subsequent ion intercalation occurs. The difference between these two electrochemical potentials will contribute to the cells open circuit voltage (V_{OC}). Within an electrochemical cell, the voltage window is also governed by the thermodynamic stability of the electrolyte solution, where anodic and cathodic stability are governed by the electrolyte's highest occupied molecular orbital (HOMO) and lowest unoccupied molecular orbital (LUMO), respectively. However, in the case of a Li-ion cell, electrochemical decomposition of the electrolyte results in an *in situ* formed solid electrolyte interphase (SEI) that offers kinetic stability (Figure 1.2). While SEI formation may increase the cycling window of the electrochemical cell, the irreversible formation of this interphase

consumes 10% of the original capacity.[14] While the SEI is electron insulating and almost impenetrable to electrolyte species, gradual capacity fade may occur if the interphase thickens.[15]

While Li-ion batteries remain ubiquitous energy storage systems for portable electronics, power tools, and limited range electric vehicles, the low elemental abundance (0.0017% in the earth's crust)[16] of lithium metal is expected to compromise future use as batteries expand in a global market,[17] an undesirable aspect also characteristic of fossil fuel driven technologies. Researchers are beginning to investigate post lithium-ion systems, defined as batteries with a theoretical energy density greater than that of current systems containing a $LiCoO_2$ cathode and carbon-based anode (2000 Wh/L).[18] Amongst the new battery chemistries, magnesium is an attractive choice since it ranks seventh in elemental abundance (2.4%, behind oxygen, silicon, aluminum, iron, calcium, and sodium),[16] but sharing some chemical properties with lithium as a reasonable starting point. For example, the $Mg^{2+/0}$ couple is comparatively negative (−2.37 V vs NHE), and magnesium metal as an anode allows for high volumetric capacity (3,832 mAh cm^{-3}). Additionally, magnesium metal is advantageous over lithium in that dendrite growth is suppressed and magnesium is environmentally benign.[19]

Despite the widespread commercial success of lithium-ion technologies, adapting its components for the rapid propulsion of magnesium-ion batteries has not been successful. There is little correlation between the chemistry of the two metal anodes besides the formation of passivation layers in the presence of many common inorganic salts and solvents.[20] As described above, in the case of lithium-based systems electrolyte decomposition results in the growth of a SEI layer. Subsequent stabilization of charge–discharge cycles is achieved since ions diffuse through while electron transfer is inhibited.[21] An analogous passivation film develops on magnesium with the notable difference that Mg^{2+} diffusion is also restricted,[22] prohibiting

magnesium anode–electrolyte compositions from including simple commercially available magnesium salts ($Mg(ClO_4)_2$, $Mg(TFSI)_2$, and $Mg(BF_4)_2$) or aprotic solvents besides ethers.[23]

1.3 Magnesium-Ion Battery Electrolytes

T. D. Gregory pioneered using Mg coordination compounds as electrolytes in 1990 at Dow Chemical,[24] and since then, Aurbach and co-workers expanded the scope to include organohaloaluminates, $Mg(AlCl_{4-n}R'_nR''_n)_2$.[25] In their 2000 report, they demonstrated reversible deposition–dissolution of magnesium with moderate anodic stability (2.5 V vs $Mg^{2+/0}$) and chemical compatibility with the Chevrel-phase Mo_6S_8 cathode material. Removing possible β-H elimination degradation pathways by replacing the aliphatic hydrocarbons with phenyl in the electrolyte composed of 0.4 M PhMgCl and 0.2 M $AlCl_3$ in THF (termed APC for all phenyl complexes) resulted in electrochemical window expansion to 3.2 V vs $Mg^{2+/0}$.[26] Unfortunately, the widespread use in battery manufacturing of the *in situ* generated organohaloaluminate is hindered by air and moisture sensitivity.

One way to overcome electrolyte sensitivity is to employ phenolate instead of phenyl—replacing the more reacting aluminum carbon bond with a more stable aluminum oxygen bond. First recognized in 2012 by Hirano, phenolate-based magnesium precursors allow for electrolytes with anodic stabilities comparable to those prepared from Grignard reagents, while also showing reversible magnesium deposition and stripping.[27] Most notably, an electrolyte composed of 2-*tert*-butyl-4-methyl-phenolate showed an anodic stability of 2.6 V vs $Mg^{2+/0}$ with the ability to deposit and strip magnesium after 3 hours of exposure to ambient air.

Magnesium monocarborane salts ($Mg(CB_{11}H_{12})_2$) are another series of electrolyte solutions that show high anodic stability (3.6 V vs $Mg^{2+/0}$).[28] However, these salts are only

accessible through a complicated recrystallization-based synthesis from relatively expensive starting materials. Additionally, an electrolyte solution composed of 0.534 M $MgCl_2$ and 0.267 M $AlCl_3$ in THF (MACC electrolyte) shows anodic stability near 3 V on a platinum electrode without the use of Grignard precursors.[29] However, the as-prepared MACC electrolyte does not support Mg electrodeposition and requires extended electrochemical conditioning (electrolyte cycling between –1.2 and 2.8 V vs $Mg^{2+/0}$ at 5 mV s^{-1} for ~50 cycles). Electrochemical conditioning renders an electrolyte composition with an increased Mg:Al ratio (from 2:1 to 2.6:1) after the irreversible electrodeposition of Al on the working electrode. Additionally, the conditioning results in free Cl within the electrolyte solution that adsorbs on the electrode surface and enhances Mg electrodeposition.[30] As a result, moving beyond today's lithium-ion technology to the more abundant metal magnesium requires advances in the fundamental science of electrolytes.

1.4 Solid State Cathode Materials for Secondary Magnesium-Ion Batteries That Are Compatible with Magnesium Metal Anodes in Water-Free Electrolyte

Despite the added complexity of magnesium anode–electrolyte compatibility, cathode design and synthesis continues to be of interest amongst researchers. The outcome of these pursuits has generated many advancements that are compiled within several recent review articles[31–34]. Here, I will highlight the specific challenge of cycling solid-state cathodes against a magnesium metal anode without using a water-contaminated electrolyte. This section serves as a guide for designing cathodes that harness the maximum capacity of magnesium metal anodes (3.8 Ah/L for Mg vs 2.1 Ah/L for Li). In addition, I will discuss existing materials that

Cathode Material	Voltage Window / V vs $Mg^{2+/0}$	Gravimetric Capacity / mAh g^{-1}	Cycle Rate	Capacity Retention / Cycle Number	Ref.
CP-Mo_6S_8	0.2–2.0	100	15 mA g^{-1} [a]	95 % / 100	[26]
MoS_2	0.5–3.0	170	20 mA g^{-1}	95 % / 50	[42]
WSe_2	0.3–3.0	203	50 mA g^{-1}	100 % / 160	[45]
MoO_3	1.4–2.7	150	0.01–0.02 mA g^{-1}	67 % / 4	[47]
α-MnO_2	0.8–3.0	240	1.5 mA g^{-1} [b]	50 % / 3	[54]

Converting *C*-rate to mA g^{-1} using the following stoichiometric formulas [a] $Mg_2Mo_6S_8$ [16] and [b] $Mg_4Mo_6S_{12}$ [12]

Table 1.1. Parameters for cathode material performance.

have already demonstrated such compatibility with magnesium metal anodes, which will aid the search for new electrolytes. A selection of parameters for the electrode materials featured in this section are presented within Table 1.1 and further discussed below.

1.4.1 Mo_6S_8

First recognized in 2000 by Aurbach and coworkers, the Chevrel-phase Mo_6S_8 (CP-Mo_6S_8) serves as an excellent host for reversible Mg^{2+} insertion and extraction[25]. Through a molten salt synthesis of $Cu_2Mo_6S_8$, followed by copper removal, the CP-Mo_6S_8 synthesis is easily scalable for manufacturing purposes[35]. The structure is composed of a cubic arrangement of sulfur atoms, where octahedral clusters of molybdenum present two possible cavities for insertion—labeled Cavity 1 and Cavity 2 by the authors in Figure 1.3.[36] Cavity 3 cannot be occupied due to strong electrostatic repulsion of molybdenum and magnesium. Upon insertion of Mg^{2+}, with the concomitant reduction of CP-Mo_6S_8 to form rhombohedral $MgMo_6S_8$, a high activation barrier exists for Mg^{2+} migration between alternate cavities. With additional Mg^{2+} insertion (when x is greater than 1 in $Mg_xMo_6S_8$), both ionic transport and insertion rates are enhanced due to cationic repulsion.[36] In the initial report, the salt identified as $Mg(AlCl_2BuEt)_2$

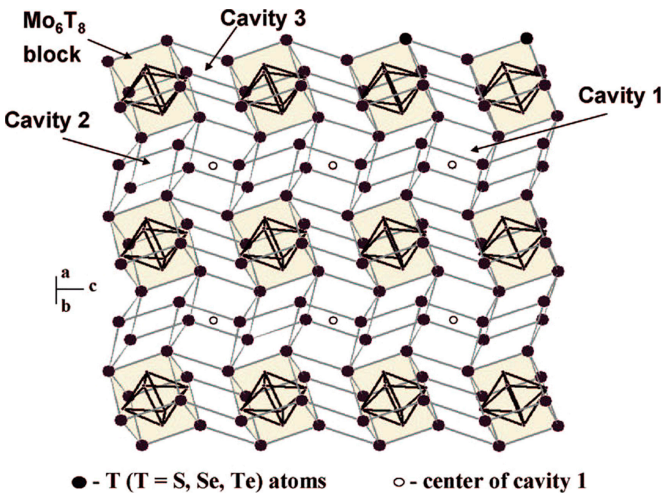

Figure 1.3. Magnesium intercalation cavities within CP-Mo_6T_8. Reprinted (adapted) with permission from Ref. 36. Copyright (2009) American Chemical Society.

in THF (0.25 M) facilitated the insertion/extraction processes with more than 2000 cycles demonstrated, at current densities between 0.1 and 1 mA cm^{-2} with <15% capacity fade observed. [25] Despite a low voltage window (0.2–2.0 V vs $Mg^{2+/0}$) and irreversible capacity loss, CP-Mo_6S_8 has been and continues to be featured in many electrolyte reports; it serves as the standard cathode material for demonstrating reversible Mg^{2+} insertion and extraction from new electrolyte formulations.

With partial substitution of sulfur with selenium in $Mo_6S_{8-x}Se_x$ ($0<x<2$), the increase in framework polarizability gives rise to improved battery electrochemistry, illustrated in Figure 1.4.[26] As the selenium content increases, the specific capacity and rate capability follow. Reduction in partial ion-trapping is also observed with sulfide substitution, arising from the distortion of the Mg^{2+} coordination sites with the larger chalcogenides. Selenide allows for enhanced ion hopping between Mg^{2+} sites.[37,38] The end member compositions $Mg_xMo_6Se_8$

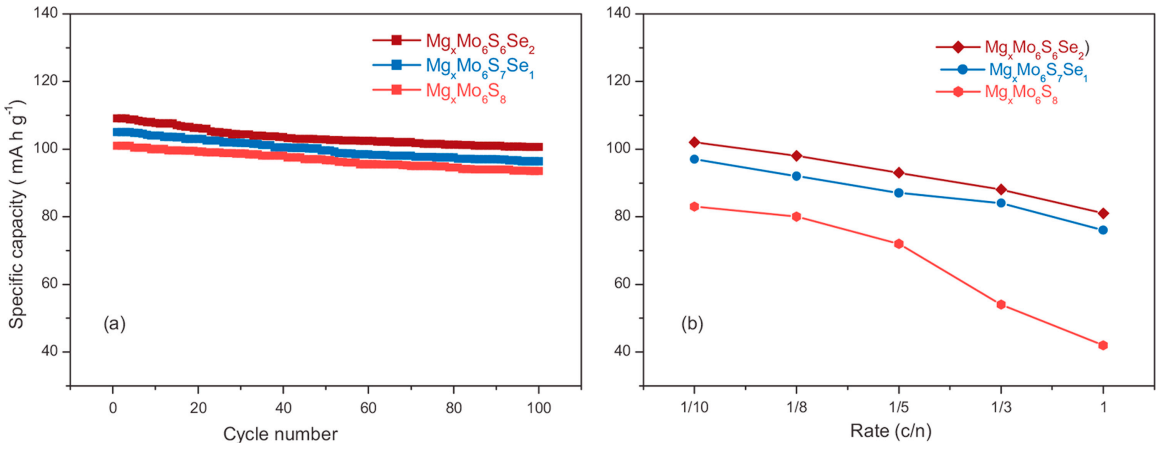

Figure 1.4. (a) Capacity vs cycle number and (b) capacity vs rate curves of various $Mg_xMo_6S_{8-y}Se_y$ (y=0, 1, 2). Reprinted (adapted) with permission from Ref. 26. Copyright (2007) WILEY-VCH Verlag GmbH & Co. KGaA, Weinheim.

($0<x<2$) show high Mg^{2+} mobility throughout the entire insertion process.[39] Additionally, electrodes composed of $Mg_xMo_6S_6Se_2$ demonstrate superior rate capabilities relative to $Mg_xMo_6S_8$ at 1 *C*, where observed losses in gravimetric capacities are 10% and 50% for $Mg_xMo_6S_6Se_2$ and $Mg_xMo_6S_8$ respectively.

1.4.2 MoS_2

With two layers of sulfur atoms sandwiching molybdenum cations, illustrated in Figure 1.6, MoS_2 represents a suitable framework for Mg^{2+} intercalation/deintercalation.[26] Initial nanostructured materials (hollow-cage fullerene-like particles, fibrous floccus, and spherical nanovesicles), prepared through solution-based chemical reactions demonstrate low insertion and extraction capacities: 2–25 mAh g^{-1} at 1.2 mA g^{-1} charging-discharging rates while using an electrolyte solution composed of 0.25 M $MgBu_2$ and 0.5 M $AlCl_3$ electrolyte in THF solvent.[40] However, MoS_2/C microspheres and an AZ31 (3 wt% Al, 1 wt% Zn, 96 wt% Mg) alloy anode show an initial discharge capacity of 213 mAh g^{-1} using $Mg(AlCl_3Bu)_2$ salt

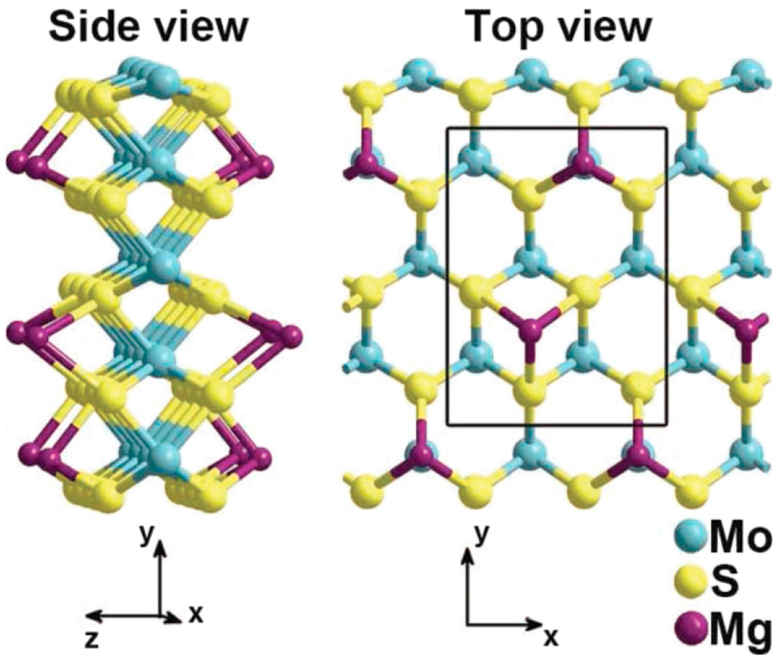

Figure 1.5. Theoretical model of Mg^{2+} intercalation within a MoS_2 single-layered nano-ribbon. Reprinted (adapted) with permission from Ref. 41. Copyright (2011) WILEY-VCH Verlag GmbH & Co. KGaA, Weinheim.

dissolved in THF solvent (at 50 mA g^{-1}). While the exact electrolyte concentrations were not specified, typical electrolyte solutions containing magnesium organohaloaluminate salts are 0.25 M in THF solvent. Subsequent cycles show a significant capacity fade (only 84.3 mAh g^{-1} after 50 cycles) due to the growth of passivating films on the Mg-anode. Nonetheless, the superior performance relative to bulk-MoS_2 is owed to the improved Mg^{2+} diffusivity through MoS_2 microspheres and enhanced electronic conductivity from the carbon coating.[41] Comparing the values of R_e (resistance from the electrolyte, electrode, and passivation film between the two) and R_{ct} (charge-transfer resistance), a decrease from 33.6 Ω and 1167 Ω to 17.82 Ω and 218 Ω is observed between annealed MoS_2 and the MoS_2/C composite, respectively. With emphasis on morphology control and design, a graphene-like MoS_2 cathode demonstrates an operating

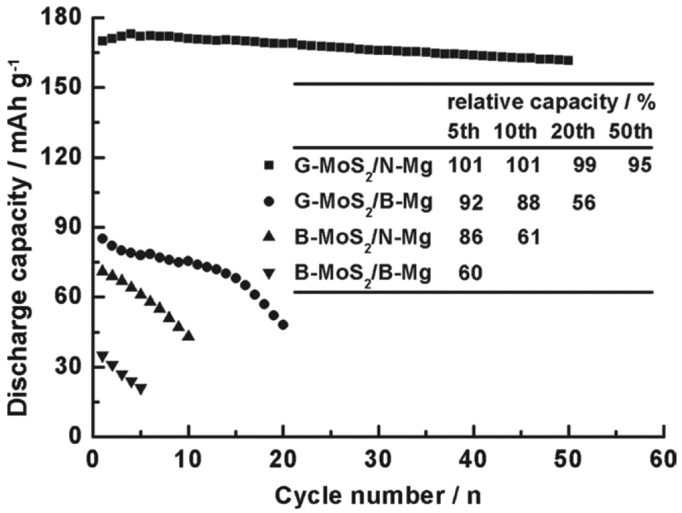

Figure 1.6. Cycling behavior of G-MoS_2 (graphene-like MoS_2), N-Mg (magnesium nanoparticle anode), B-MoS_2 (bulk MoS_2), and B-Mg (bulk magnesium). Reprinted (adapted) with permission from Ref. 41. Copyright (2011) WILEY-VCH Verlag GmbH & Co. KGaA, Weinheim.

voltage of 1.8 V vs $Mg^{2+/0}$ and a discharge capacity of 170 mAh g^{-1} at 20 mA g^{-1} when paired with a Mg nanoparticle anode and an electrolyte solution composed of 0.25 M $MgBu_2$ and 0.5 M $AlCl_3$ electrolyte in THF solvent. Most notably, Figure 1.6 illustrates that this combination shows minimal capacity fade, retaining 95% capacity after 50 discharge–charge cycles.[42] Cells constructed with magnesium nanoparticle anodes (N-Mg) demonstrate improved performance due to the generation of thinner passivation films relative to bulk magnesium metal anodes (B-Mg), since they possess substantially larger surface area than B-Mg.[43] It is clear that graphene-like MoS_2 (G-MoS_2) outperforms bulk-MoS_2 (B-MoS_2), likely due to the bifacial Mg intercalation into expanded MoS_2 single layers.[44]

1.4.3 WSe_2

The layered chalcogenide WSe_2, which is isostructural to MoS_2, has also been employed as a cathode material for rechargeable Mg^{2+} batteries. WSe_2 nanowires with an average diameter

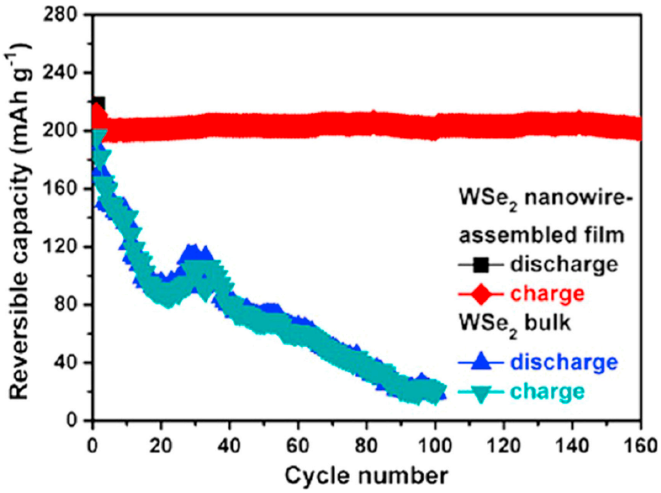

Figure 1.7. Comparison of cycling behavior between bulk WSe_2 and WSe_2 nanowire-based electrodes. Reprinted (adapted) with permission from Ref. 45. Copyright (2013) American Chemical Society.

of 100 nm, prepared via chemical vapor deposition, demonstrate a reversible specific capacity of 203 mAh g^{-1} (at 50 mA g^{-1}), when employing a $Mg(AlCl_2BuEt)_2$ electrolyte in THF (0.25 M) between 0.3 and 3 V vs $Mg^{2+/0}$ for over 160 cycles.[45] The rate capability was measured, and the nanowires show a capacity of 142 mAh g^{-1} at 800 mA g^{-1}. Further investigation showed that rates as high as 1500 and 3000 mA g^{-1} delivered capacities of 120 and 103 mAh g^{-1}, respectively. In the same report, bulk WSe_2 shows dramatically inferior cycling characteristics–only 10% capacity retention after 100 cycles (Figure 1.7).[45] One cause of battery failure is that the cells were operated at potentials greater than the anodic stability of the electrolyte (2.4 V vs $Mg^{2+/0}$).[25] Our group has recently demonstrated reversible Mg^{2+} intercalation–deintercalation with bulk WSe_2 using a 0.5 M PhMgCl and 0.125 M $Al(OPh)_3$ in THF solvent electrolyte, with average discharge capacities of 80 mAh g^{-1} (at *C*/5).[46]

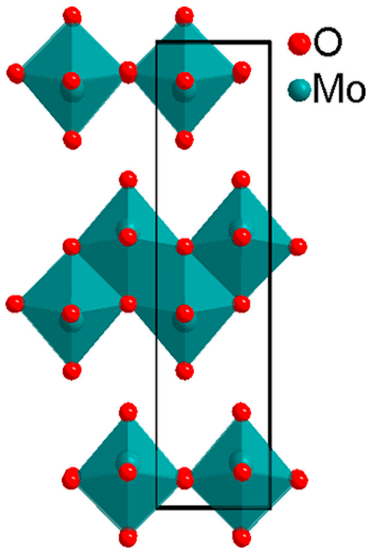

Figure 1.8. Structure of MoO_3 viewed along [0 1 0].

1.4.4 MoO_3

The layered molybdate, MoO_3 (Figure 1.8) demonstrates 0.50 mol of magnesium/moles of host with an optimal capacity of 143 mAh g^{-1} determined through the chemical intercalation of Mg^{2+} using an excess of a 0.7 M dibutylmagnesium/heptane solution.[24] An ionic liquid containing 56 wt% $AlCl_3$, 41 wt% 1-ethyl-3-methylimidazolium chloride (EMIC), and 3 wt% $MgCl_2$ at 80 °C facilitated an initial discharge capacity of 150 mAh g^{-1}. However significant capacity fade is observed, with discharge capacities falling below 100 mAh g^{-1} after subsequent galvanostatic cycles between 0.01 and 0.02 mA g^{-1}.[47] Further investigation of MoO_3 outside the use of water-containing (wet) organic-based electrolytes[48] has not been reported.

1.4.5 α-MnO_2

MnO_2, with its variety of crystalline polymorphs and microstructures[49] that have been used as successful host storage materials for lithium-ion batteries[50,51], has continued to be a target for divalent battery systems. With a (2x2) tunnel structure (Figure 1.9), α-MnO_2 contains

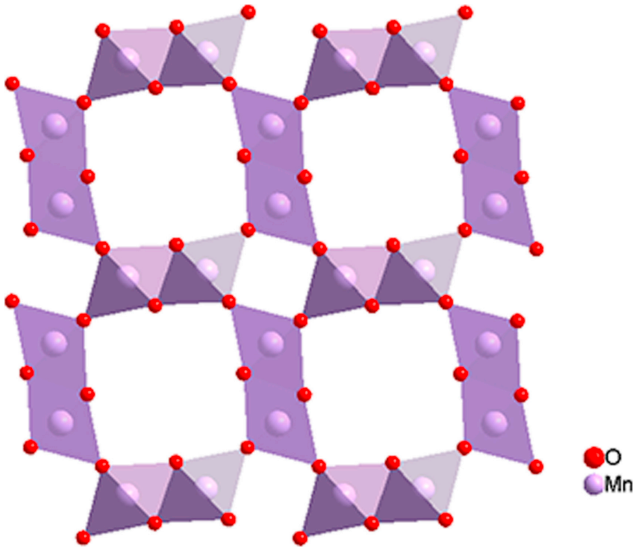

Figure 1.9. Structure of α-MnO_2 viewed along [0 1 0].

suitable channels for the insertion/extraction of Mg^{2+} upon subsequent reduction/oxidation of manganese ions. While initial reports demonstrated magnesium insertion/extraction, the electrolytes employed are not compatible with a magnesium metal anode.[52] Nonetheless, using a 0.2 M Mg-HMDS $(Mg_2(\mu\text{-}Cl)_3\bullet 6(OC_4H_8))((N(Si(CH_3)_3)_2)_nAlCl_{4-n})$ (n=1, 2) electrolyte in THF solvent[53] shows an initial specific capacity of 280 mAh g^{-1} (at 1.5 mA g^{-1} rates) while employing commercially available nano-sized α-MnO_2. Unfortunately upon successive cycles of magnesium insertion/extraction, the tunneled structure collapses, leading to irreversible capacity fade (50%).[54] Despite a large capacity fade α-MnO_2, allows for high voltage electrolyte compositions to be examined[28] since its electrochemical stability window exceeds that of CP-Mo_6S_8 (3.5 V vs $Mg^{2+/0}$) while maintaining comparable gravimetric capacities.

1.5 Outline

Within the field of Mg-ion batteries electrolyte development continues to govern the rate of progress, as many of the electrolyte properties will determine the employed cathode material within a battery device. As a result, the work presented in this thesis explores the synthesis and electrochemical characterization of Lewis acid stabilized magnesium-ion battery electrolyte solutions. Chapter 2 discusses the influence of steric bulk on the oxidative stability and solution conductivity of phenolate-based magnesium-ion battery electrolytes. With the combination of density functional theory (DFT) and the design principles outlined in Chapter 2 a series of highly soluble fluorinated alkoxide-based electrolytes were prepared, examined electrochemically, and reversibly cycled while employing the standard Chevrel phase-Mo_6S_8 cathode material within Chapter 3. Chapter 4 further probes the resulting electrode-electrolyte interface to determine the kinetics of Mg deposition as well as examine the deposition morphology onto a bulk metal working electrode. The chemical identity of electrolyte decomposition products from series of solutions containing PhMgCl in THF are determined and examined electrochemically within Chapter 5. The final chapter, Chapter 6, provides my outlook for future work that will result in the most impactful contributions to the field.

1.6 References

(1) Shafiee, S.; Topal, E. When will fossil fuel reserves be diminished? *Energy Policy* **2009**, *37*(1), 181– 189.

(2) Klass, D. L. Biomass for renewable energy, fuels, and chemicals; Academic Press: San Diego, 1998.

(3) *International Energy Outlook 2018*; Washington, D.C., 2018.

(4) Powell, C. A.; Morreale, B. D. Materials challenges in advanced coal conversion technologies *MRS Bull.* **2008**, *33*, 309– 315.

(5) Arunachalam, V. S.; Fleischer, E. L. The global energy landscape and materials innovation *MRS Bull.* **2008**, *33*, 264– 288.

(6) Meier, P. J.; Wilson, P. P. H.; Kulcinski, G. L.; Denholm, P. L. US electric industry response to carbon constraint: a life-cycle assessment of supply side alternatives *Energy Policy* **2005**, *33*, 1099– 1108.

(7) Yang, Z.; Zhang, J.; Kintner-Meyer, M. C. W.; Lu, X.; Choi, D.; Lemmon, J. P.; Liu, J. Electrochemical energy storage for green grid *Chem. Rev.* **2011,** *111*, 3577– 3613.

(8) Dunn, B.; Kamath, H.; Tarascon, J.-M. Electrical energy storage for the grid: a battery of choices *Science* **2011**, *334*, 928– 935.

(9) Planté, G. *C. R. Acad. Sci. Paris* **1860** *50*, 640– 642.

(10) Haefliger, P.; Mathieu-Nolf, M.; Lociciro, S.; Ndiaye, C.; Coly, M.; Diouf, A.; Faye, A. L.; Sow, A.; Tempowski, J.; Pronczuk, J.; Junior, A. P. F.; Bertollini, R.; Neira, M. Mass lead intoxication from informal used lead-acid battery recycling in Dakar, Senegal *Environ. Health Perspect.* **2009**, *117*(10), 1535– 1540.

(11) Huggins, R. A. Energy storage: fundamentals, materials and applications; Springer International, 2016.

(12) Liu, C.; Neale, Z. G.; Cao, G. Understanding electrochemical potentials of cathode materials in rechargeable batteries *Materials Today* **2016**, *19*(2), 109– 123.

(13) Armand, M.; Tarascon, J.-M. Building better batteries *Nature* **2008**, *451,* 652– 657.

(14) Patil, A.; Choi, J.-W.; Yoon, S.-J. Review of issue and challenges facing rechargeable nanostructured lithium batteries *Mater. Res. Bull*. **2006**, *43*, 1913– 1942.

(15) Verma, P.; Maire, P.; Novák, P. A review of the features and analyses of the solid electrolyte interphase in Li-ion batteries *Electrochim. Acta* **2010**, *55*, 6332– 6341.

(16) Greenwood, N.; Earnshaw, A. *Chemistry of the Elements*; Second, Ed.; Butterworth-Heinemann: Oxford, 1997.

(17) Speirs, J.; Contestabile, M.; Houari, Y.; Gross, R. The future of lithium availability for electric vehicle batteries *Renewable and Sus. Energy Rev.* **2014**, *35*, 183− 193.

(18) Muldoon, J.; Bucur, C. B.; Oliver, A. G.; Sugimoto, T.; Matsui, M.; Kim, H. S.; Allred, G. D.; Zajicek, J.; Kotani, Y. Electrolyte roadblocks to a magnesium rechargeable battery *Energy Environ. Sci.* **2012**, *5*(3), 5941– 5950.

(19) Matsui, M. Study on electrochemically deposited Mg metal *J. Power Sources* **2011**, *196*, 7048– 7055.

(20) Aurbach, D.; Gofer, Y.; Lu, Z.; Schechter, A.; Chusid, O.; Gizbar, H.; Cohen, Y.; Ashkenazi, V.; Moshkovich, M.; Turgeman, R.; Levi, E. A short review on the comparison between Li battery systems and rechargeable magnesium battery technology *J. Power Sources* **2001**, *97–98*, 28– 32.

(21) Crowther, O.; West, A. C. Effect of electrolyte composition on lithium dendrite growth *J. Electrochem. Soc.* **2008**, *155,* A806– A811.

(22) Aurbach, D.; Gofer, Y.; Schechter, A.; Chusid, O.; Gizbar, H.; Cohen, Y.; Moshkovich, M.; Turgeman, R. A comparison between the electrochemical behavior of reversible magnesium and lithium electrodes *J. Power Sources* **2001**, *97–98*, 269– 273.

(23) Aurbach, D.; Weissman, I.; Gofer, Y.; Levi, E. Nonaqueous magnesium electrochemistry and its application in secondary batteries *Chem. Rec.* **2003**, *3*, 61– 73.

(24) Gregory, T. D.; Hoffman, R. J.; Winterton, R. C. Nonaqueous electrochemistry of magnesium *J. Electrochem. Soc*. **1990**, *137*, 775– 780.

(25) Aurbach, D.; Lu, Z.; Schechter, A.; Gofer, Y.; Gizbar, H.; Turgeman, R.; Cohen, Y.; Moshkovich, M.; Levi, E. Prototype systems for rechargeable magnesium batteries *Nature* **2000**, *407*, 724– 727.

(26) Aurbach, D.; Suresh, G. S.; Levi, E.; Mitelman, A.; Mizrahi, O.; Chusid, O.; Brunelli, M. Progress in rechargeable magnesium battery technology *Adv. Mater.* **2007**, *19*(23), 4260– 4267.

(27) Wang, F.; Guo, Y.; Yang, J.; Nuli, Y.; Hirano, S. A novel electrolyte system without a Grignard reagent for rechargeable magnesium batteries *Chem. Commun.* **2012**, *48*, 10763– 10765.

(28) Tutusaus, O.; Mohtadi, R.; Arthur, T. S.; Mizuno, F.; Nelson, E. G.; Sevryugina, Y. V. An efficient halogen-free electrolyte for use in rechargeable magnesium batteries *Angew. Chem., Int. Ed.* **2015**, *54*, 7900– 7904.

(29) Doe, R. E.; Han, R.; Hwang, J.; Gmitter, A. J.; Shterenberg, I.; Yoo, H. D.; Pour, N.; Aurbach, D. Novel, electrolyte solutions comprising fully inorganic salts with high anodic stability for rechargeable magnesium batteries *Chem. Commun.* **2013**, *50*, 243– 245.

(30) See, K. A.; Chapman, K. W.; Zhu, L.; Wiaderek, K. M.; Borkiewicz, O. J.; Barile, C. J.; Chupas, P. J.; Gewirth, A. A. The interplay of Al and Mg speciation in advanced Mg battery electrolyte solutions *J. Am. Chem. Soc.* **2016**, *138*(1), 328– 337.

(31) Muldoon, J.; Bucur, C. B.; Gregory, T. Quest for nonaqueous multivalent secondary batteries: magnesium and beyond *Chem. Rev.* **2014**, *114*(23), 11683– 11720.

(32) Huie, M. M.; Bock, D. C.; Takeuchi, E. S.; Marschilok, A. C.; Takeuchi, K. J. *Coord. Chem. Rev.* Cathode materials for magnesium and magnesium-ion based batteries **2014**, *287*, 15– 27.

(33) Saha, P.; Datta, M. K.; Velikokhatnyi, O. I.; Manivannan, A.; Alman, D.; Kumta P. N. Rechargeable magnesium battery: current status and key challenges for the future *Prog. Mater. Sci.* **2014**, *66,* 1– 86.

(34) Shterenberg, I.; Salama, M.; Gofer, Y.; Levi, E.; Aurbach, D. The challenge of developing rechargeable magnesium batteries *MRS Bull.* **2014**, *39*, 453– 460.

(35) Lancry, E.; Levi, E.; Gofer, Y.; Levi, M.; Salitra, G.; Aurbach, D. Leaching chemistry and the performance of the Mo_6S_8 cathodes in rechargeable Mg batteries *Chem. Mater.* **2004**, *16*, 2832– 2838.

(36) Levi, E.; Gershinsky, G.; Aurbach, D.; Isnard, O.; Ceder, G. New insight on the unusually high ionic mobility in Chevrel phases *Chem. Mater.* **2009**, *21*, 1390– 1399.

(37) Levi, E.; Mitelman, A.; Aurbach, D.; Brunelli, M. Structural mechanism of the phase transitions in the Mg–Cu–Mo_6S_8 system probed by ex situ synchrotron X-ray diffraction *Chem. Mater.* **2007**, *19*, 5131– 5142.

(38) Mitelman, A.; Levi, M. D.; Lancry, E.; Levi, E.; Aurbach, D. New cathode materials for rechargeable Mg batteries: fast Mg ion transport and reversible copper extrusion in $Cu_yMo_6S_8$ compounds *Chem. Commun.* **2007**, *0*, 4212– 4214.

(39) Levi, E.; Mitelman, A.; Isnard, O.; Brunelli, M.; Aurbach, D. Phase diagram of Mg insertion into Chevrel phases, $Mg_xMo_6T_8$ (T = S, Se). 3. The crystal structure of triclinic $Mg_2Mo_6Se_8$ *Inorg. Chem.* **2008**, *47*, 1975– 1983.

(40) Li, X.-L.; Li, Y.-D. MoS_2 nanostructures: synthesis and electrochemical Mg^{2+} intercalation *J. Phys. Chem. B* **2004**, *108*, 13893– 13900.

(41) Liu, Y. C.; Jiao, L. F.; Wu, Q.; Du, J.; Zhao, Y. P.; Si, Y. C.; Wang, Y. J.; Yuan, H. T. Sandwich-structured graphene-like MoS_2/C microspheres for rechargeable Mg batteries *J. Mater. Chem. A* **2013**, *1*, 5822– 5826.

(42) Liang, Y. L.; Feng, R. J.; Yang, S. Q.; Ma, H.; Liang, J.; Chen, J. Rechargeable Mg batteries with graphene-like MoS_2 cathode and ultrasmall Mg nanoparticle anode *Adv. Mater.* **2011**, *23*, 640– 643.

(43) Lu, Z.; Schechter, A.; Moshkovich, M.; Aurbach, D. On the electrochemical behavior of magnesium electrodes in polar aprotic electrolyte solutions *J. Electroanal. Chem.* **1999**, *466,* 203– 217.

(44) Liu, Y.; Xue, J. S.; Zheng, T.; Dahn, J. R. Mechanism of lithium insertion in hard carbons prepared by pyrolysis of epoxy resins *Carbon* **1996**, *34*, 193– 200.

(45) Liu, B.; Luo, T.; Mu, G. Y.; Wang, X. F.; Chen, D.; Shen, G. Z. Rechargeable Mg-ion batteries based on WSe_2 nanowire cathodes *ACS Nano* **2013**, *7*, 8051– 8058.

(46) Nelson, E. G.; Brody, S. I.; Kampf, J. W.; Bartlett, B. M. A magnesium tetraphenylaluminate battery electrolyte exhibits a wide electrochemical potential window and reduces stainless steel corrosion *J. Mater. Chem. A* **2014**, *2*, 18194– 18198.

(47) Spahr, M. E.; Novak, P.; Haas, O.; Nesper, R. Electrochemical insertion of lithium, sodium, and magnesium in molybdenum(VI) oxide *J. Power Sources* **1995**, *54*, 346– 351.

(48) Gershinsky, G.; Yoo, H. D.; Gofer, Y.; Aurbach, D. Electrochemical and spectroscopic analysis of Mg^{2+}intercalation into thin film electrodes of layered oxides: V_2O_5 and MoO_3 *Langmuir* **2013**, *29*, 10964– 10972.

(49) Ghodbane, O.; Pascal, J.-L.; Favier, F. Microstructural effects on charge-storage properties in MnO_2-based electrochemical supercapacitors *ACS Appl. Mater. Interfaces* **2009**, *1*, 1130– 1139.

(50) Bach, S.; Pereira-Ramos, J. P.; Baffier, N. A new MnO_2 tunnel related phase as host lattice for Li intercalation *Solid State Ionics* **1995**, *80*, 151– 158.

(51) Johnson, C.; Dees, D.; Mansuetto, M.; Thackeray, M.; Vissers, D.; Argyriou, D.; Loong, C.-K.; Christensen, L. Structural and electrochemical studies of α-manganese dioxide (α-MnO_2) *J. Power Sources* **1997**, *68*, 570– 577.

(52) Kumar, G. G.; Munichandraiah, N. Solid-state rechargeable magnesium cell with poly(vinylidenefluoride)–magnesium triflate gel polymer electrolyte *J. Power Source*s **2001**, *102*, 46– 54.

(53) Kim, H. S.; Arthur, T. S.; Allred, G. D.; Zajicek, J.; Newman, J. G.; Rodnyansky, A. E.; Oliver, A. G.; Boggess, W. C.; Muldoon, J. Structure and compatibility of a magnesium electrolyte with a sulphur cathode *Nat. Commun.* **2011**, *2*, 422– 427.

(54) Zhang, R.; Yu, X.; Nam, K.-W.; Ling, C.; Arthur, T. S.; Song, W.; Knapp, A. M.; Ehrlich, S. N.; Yang, X.-Q.; Matsui, M. α-MnO_2 as a cathode material for rechargeable Mg batteries *Electrochem. Commun.* **2012**, *23*,110– 113.

Chapter 2

Influence of Steric Bulk on the Oxidative Stability of Phenolate-Based Magnesium-Ion Battery Electrolytes

Portions of this chapter have been published:

Crowe, A. J.; Bartlett, B. M. *J. Mater. Chem. A* **2016**, *4*, 368–371.

2.1 Introduction

While the electrolyte composed of 0.4 M PhMgCl and 0.2 M $AlCl_3$ in THF (APC) offers an electrochemical stability window of 3.2 V vs $Mg^{2+/0}$ the pyrophoric components warrant significant safety concern.[1] Additionally, the air and moisture sensitivity of the *in situ* generated organohaloaluminate renders the assembly of large-scale energy storage systems difficult. Phenolate-based magnesium precursors, within the typical 0.5 M ^{R}PhOMgCl and 0.25 M $AlCl_3$ in THF electrolyte system, offer improved air and moisture stability with anodic stabilities that are comparable to those composed of Grignard reagents. Within the original report on phenolate-based magnesium-ion battery electrolytes, a solution composed of 0.5 M 2-*tert*-butyl-4-methyl-phenolatemagnesium chloride and 0.25 M $AlCl_3$ in THF offers an anodic stability of 2.6 V vs $Mg^{2+/0}$. Most notably, this solution demonstrates the ability to deposit and strip magnesium after 3 hours of exposure to ambient air.[2] Depending on the nature and number of substituents about the phenol precursor, an approximate 500 mV difference in anodic stability was observed. However, no insight into the structure–function relationships to guide future electrolyte design was presented therein.

To begin developing a series of design principles for next generation magnesium-ion battery electrolytes we utilized this phenolate-based electrolyte system to demonstrate a strong electronic effect with *para*-substituted phenols. Specifically, we show within electrolyte salts composed of ^{R}PhOMgCl (R = CF_3, ^{t}Bu, H, Me, and OMe all in the *para*-position) and $AlCl_3$ that electron-withdrawing groups provide the greatest oxidative stability.[3] However, within this work an increased anodic stability of the 4-*tert*-butylphenolate salt could not be explained by electronic arguments alone, suggesting a separate steric influence.

In this chapter, we continue our efforts in investigating the structure-function relationships that govern the electrochemical performance of Lewis acid stabilized electrolyte solutions using physical organic chemistry principles. Through detailed electrochemical measurements, combined with NMR spectroscopy, we show while the incorporation of additional alkyl substituents at the 2 and 6 positions of a *para*–substituted phenol precursor offers an almost unchanged anodic stability, a nearly two-fold enhancement in solution conductivity results.

2.2 Experimental

2.2.1 Synthesis of Electrolyte Solutions

Tetrahydrofuran was purchased from EMD anhydrous and further dried by refluxing under N_2 over the ketyl radical produced by reacting sodium and benzophenone. Once loaded into the N_2 glovebox, 3 Å molecular sieves were added to the THF solvent. Aluminum chloride was purchased anhydrous and used as received from Alfa Aesar. All electrolyte solutions were prepared in a nitrogen-filled glovebox (Vacuum Atmospheres) prior to loading into an argon-filled glovebox (Vacuum Atmospheres) for electrochemical measurements. Electrolyte solutions were prepared analogous to the following procedure represented for 0.5 M ^{R}PhOMgCl and 0.25

M $AlCl_3$ (R = ^{t}Bu) in THF. 2 M ethylmagnesium chloride in THF (8 mmol, 4 mL) was slowly added via syringe to a solution of 4-*tert*-butylphenol (8 mmol, 1.20 g) dissolved in dry THF (4 mL). The mixture was allowed to stir overnight, forming ^{R}PhOMgCl (R = ^{t}Bu). Then, a 0.5 M solution of $AlCl_3$ (4 mmol, 8 mL) in THF (0 °C) was prepared in a 20 mL scintillation vial, warmed to room temperature, and added to the phenolatemagnesium chloride. This solution was then stirred for 8 hours, providing a clear colorless solution of 0.5 M ^{R}PhOMgCl and 0.25 M $AlCl_3$ (R = ^{t}Bu) in THF.

2.2.2 Electrolyte Solution Characterization

^{27}Al NMR was performed on a Varian VNMRS-700 MHz spectrometer in THF with chemical shifts reported relative to a solution of $AlCl_3$ in D_2O with a drop of concentrated HCl. Peak assignments were made with reference to previous work in the Bartlett group.[3] Cyclic voltammograms were recorded using a CH Instruments Electrochemical Workstation 1000A or 660C while using a Pt-disk working and Mg-foil counter- and reference electrodes. Measurements were performed starting at open circuit potential and scanned to more negative electrochemical potentials within a custom-designed, three-necked, sealed glass cell. Conductivity measurements were obtained using a YSI Model 3200 meter equipped with a 3253 conductivity cell at room temperature.

Transference numbers (t_+) were estimated assuming deposition directly from Mg^{2+}, as described in a previous report.[4] In brief, chronopotentiometry was used to deposit Mg metal using a Pt-disk working electrode, and Mg strips as reference and counter electrodes, with 1 mL of electrolyte. A controlled amount of charge was passed between the electrodes, and magnesium deposits were then digested in 10 mL of 0.1 M HNO_3 solution. The prepared solution was analyzed with ICP-AES for Mg^{2+} using a Perkin-Elmer Optima 2000DV. Samples were

referenced to an yttrium internal standard and concentrations of magnesium were determined from the maximum intensity compared to those of standard reference solutions.

2.2.3 Electrochemical Cell Preparation and Measurements

A slurry of Mo_6S_8 was prepared by mixing an 8:1:1 (by weight) ratio of Mo_6S_8, super-P carbon powder, and polyvinylidine fluoride (PVDF) binder, suspended in N-methyl-2-pyrrolidinone (NMP). The active material loading was approximately 2 mg cm^{-2}. The slurry was doctor bladed onto a stainless steel current collector and dried in an oven at 120 °C, placed in a 2016-type coin cell with a Mg-foil anode and a soaked glass fiber separator in 0.5 M ^{R}PhOMgCl and 0.25 M $AlCl_3$ (R = 2,4,6-Me_3) in THF electrolyte. Electrochemical cycling was carried out on a Vencon UBA4 battery analyzer charger and conditioner (Toronto, Canada) with cut-off voltages of 1.6 and 0.2 V vs $Mg^{2+/0}$.

2.3 Results and Discussion

2.3.1 *Para*-Alkyl Substituted Phenolate-Based Electrolyte Solutions

To begin this work, we probe the effects of steric bulk with respect to oxidative stability within the ^{R}PhOMgCl and $AlCl_3$ in a THF electrolyte system. We generated five solutions, R = Me, Et, ^{i}Pr, ^{s}Bu, and ^{t}Bu (again, all in the *para* position) by first reacting ethyl magnesium chloride with the respective phenol, followed by adding an $AlCl_3$–THF solution. Details of the synthesis are provided in the experimental section above.

By cyclic voltammetry of a THF solution composed of 0.5 M ^{R}PhOMgCl and 0.25 M $AlCl_3$, the *para*-substituted phenols show anodic stability that increases by 150 mV (2.58–2.73 V) in the order R = Me, Et, ^{i}Pr, ^{s}Bu, and ^{t}Bu (Figure 2.1), with solution conductivities comparable to those in previous reports.[2,3] The most anodically stable salt having R = ^{t}Bu also

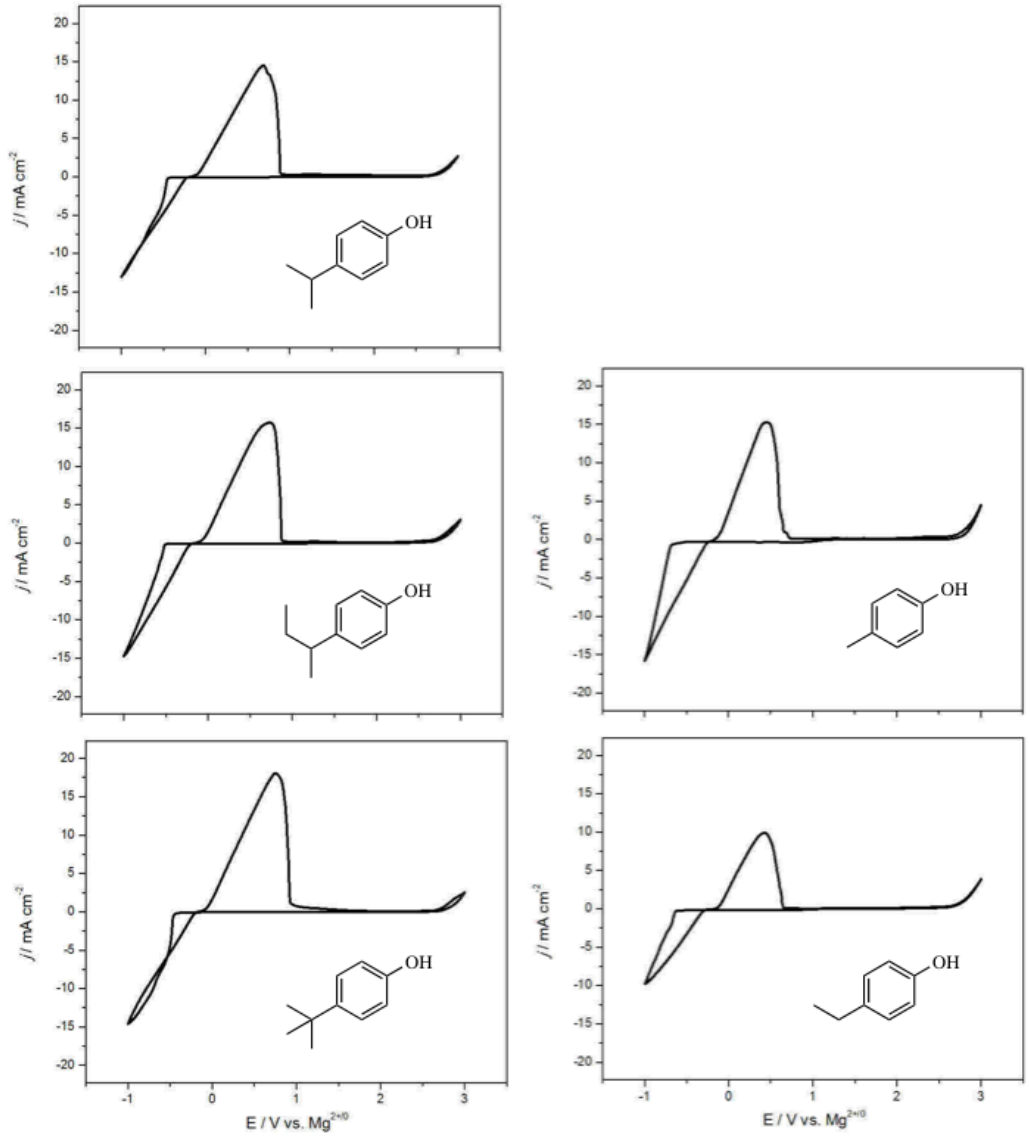

Figure 2.1. Cyclic voltammograms of 0.5 M ^{R}PhOMgCl and 0.25 M $AlCl_3$ (R = 4-Me, 4-Et, 4-^{i}Pr, 4-^{s}Bu, and 4-^{t}Bu).

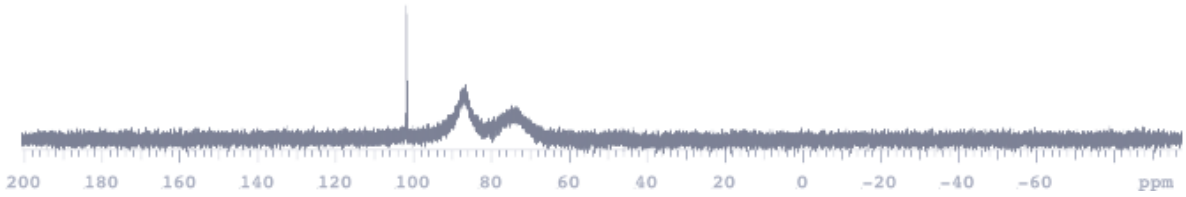

Figure 2.2. ^{27}Al NMR chemical shifts and assignments for 0.5 M ^{R}PhOMgCl and 0.25 M $AlCl_3$ (R = 4-Me, 4-Et, 4-^{i}Pr, 4-^{s}Bu, and 4-^{t}Bu) in THF: 74 ppm $[(^{R}PhO)_2AlCl_2]^{-}$, 87 ppm $[(^{R}PhO)AlCl_3]^{-}$, and 102 ppm Al_2Cl_6.

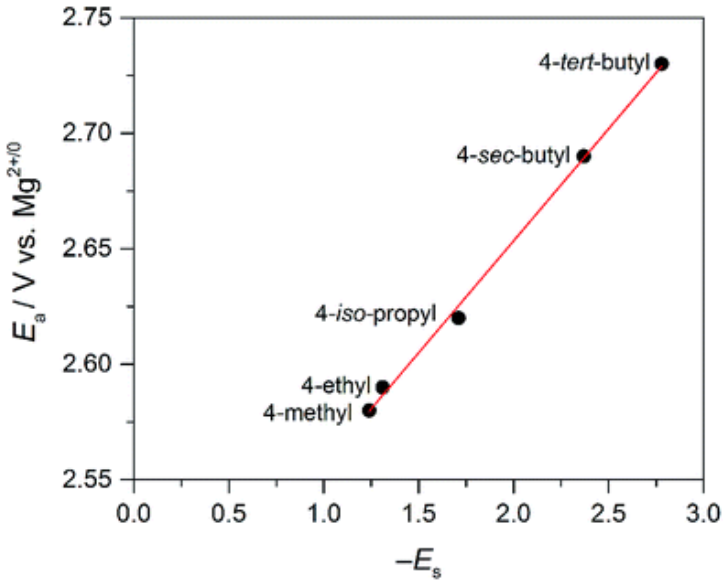

Figure 2.3. Anodic stability defined as the potential for the onset of 5 μA anodic current vs Taft's steric bulk parameter ($-E_s$) of *para*-substituted phenols (relative to unsubstituted phenol). The linear fit is shown in red.

shows high deposition/stripping efficiency on a Pt-disk working electrode (94%). The ^{27}Al NMR spectra display solution speciation dominated by $R_2AlCl_2^-$ and $RAlCl_3^-$ for all *para*-substituted electrolytes, consistent with our previous findings (Figure 2.2).[3] We surmise that in solution, magnesium is present as the typically observed $[Mg_2(\mu\text{-}Cl)_3(THF)_6]^+$ complex cation.[4–7]

With electrochemical results suggesting a steric influence, we sought quantification of steric bulk for direct comparison relative to oxidative stability. A linear relationship between anodic stability and Taft's steric bulk parameter ($-E_s$)[8,9] was observed (Figure 2.3), suggesting inductive charge dissipation from the site of oxidation of the coordinated phenol within the $(^{R}PhO)_xAlCl_{4-x}$ (x= 1–2) anion, allowing for an expansion of the electrochemical window. Consistent with previous studies, destabilization of the partial positive charge from the aluminum–oxygen bond increases the oxidative stability.[10–12]

Electrolyte/R	E_a[a]/V	σ/mS cm^{-1}	$-E_s$	CE/%
4-Me	2.58	1.25	1.24	81
4-Et	2.59	1.21	1.31	81
4-^{i}Pr	2.62	1.17	1.71	82
4-^{s}Bu	2.69	1.16	2.37	89
4-^{t}Bu	2.73	1.18	2.78	94
2,4,6-Me$_3$	2.56	2.56		92
2,4,6-^{t}Bu$_3$	2.72	1.29		70
2,6-Me$_2$	2.52	2.48		95
2,6-^{t}Bu$_2$	2.35	1.66		84

[a] E_a is defined as the potential at which 5 μA anodic current is observed.

Table 2.1. Anodic stability (potential vs $Mg^{2+/0}$), conductivity, Taft's steric substituent constant and Coulombic efficiency for deposition–dissolution of *para*-substituted (top) and multi-substituted phenol-based electrolytes (bottom).

2.3.2 Effect of *Ortho*-Substituents on *Para*-Alkyl Substituted Phenolate-Based Electrolyte Solutions

Further insight regarding the effects of steric bulk was gained by preparing electrolytes starting from 2,4,6-tri-methylphenol and 2,4,6-tri-*tert*-butylphenol to give R = Me$_3$ and ^{t}Bu$_3$ respectively, groups. Collective electrochemical properties and cyclic voltammetry results can be found in Table 2.1 (bottom) and Figure 2.4 (top), respectively.

Adding identical *ortho*-substituents to the *para*-phenol equivalent negligibly contributes to anodic stabilities. However, substitution at the *ortho* positions does lead to increased solution conductivity, presumably due to weaker ion pairing between the magnesium cations and the phenolic aluminum anions. A two-fold increase in solution conductivity is observed for electrolytes composed of 4-methylphenol and 2,4,6-trimethylphenol both at room temperature (Table 2.1) and at −10 °C (0.63 and 1.3 mS cm^{-1}, respectively). The steric bulk of the substituent plays a larger role than does the number of substituted sites. That is, the solution conductivity of the electrolytes comprising methyl-derivatized phenols is consistently greater than that of the *tert*-butyl-derivatized phenols. ^{27}Al NMR spectra reveal increased speciation in the R = Me$_3$-

and Me_2-containing electrolytes, consisting of each species $[^{R}PhO_xAlCl_{4-x}]^-$ (x = 1–4) (Figure 2.5). With a conductivity of 2.56 mS cm^{-1}, the electrolyte composed of 0.5 M ^{R}PhOMgCl and 0.25 M $AlCl_3$ (R = 2,4,6-Me_3) in THF is comparatively one of the most conductive electrolytes to date.[3,11,13] Further insight is provided from calculating the cation transference numbers (t_+) according to the equation:

$$t_+ = 1 - (z_+ F \Delta C^* V/q)$$

where z_+ is the cation valency (= 2), F is Faraday's constant 26.801 mAh $mmol^{-1}$, change in bulk magnesium ion concentration (ΔC^* / mmol L^{-1}), V is the volume of electrolyte (10^{-3} L), and q is the charge passed (0.13 mAh). From Faraday's law the theoretical change in Mg^{2+} concentration is 5.89 ppm for a divalent cation (z^+ = 2) and 23.58 ppm for a monovalent cation (z_+ = 1). With ICP-AES elemental analysis, 3.674 and 1.325 ppm of Mg^{2+} in solution for R = 4-Me and 2,4,6-Me_3, respectively, was measured. As a result, we find that electrolytes composed of R = 4-Me and 2,4,6-Me_3 demonstrate transference numbers of 0.38 and 0.78, respectively, assuming a divalent cation. As the size of the phenol increases, both the transference number and the solution conductivity increase. Notable is that only a divalent cation (z_+ = 2) gives rise to meaningful transference numbers. Thus, it is unlikely that $[Mg_2(\mu\text{-}Cl)_3(THF)_6]^+$ contributes directly to magnesium deposition and stripping. This phenomenon is an ongoing area of investigation for phenolate-based magnesium electrolytes with $AlCl_3$. Nevertheless, our higher transference numbers compared to those reported[4] suggest enhanced cation mobility due to looser ion pairing to the larger aluminate anion.

Electrolytes starting from 2,6-dimethylphenol (R = Me_2) and 2,6-di-*tert*-butylphenol (R = $^{t}Bu_2$) were also prepared for evaluating the specificity of the charge dissipation distance and its

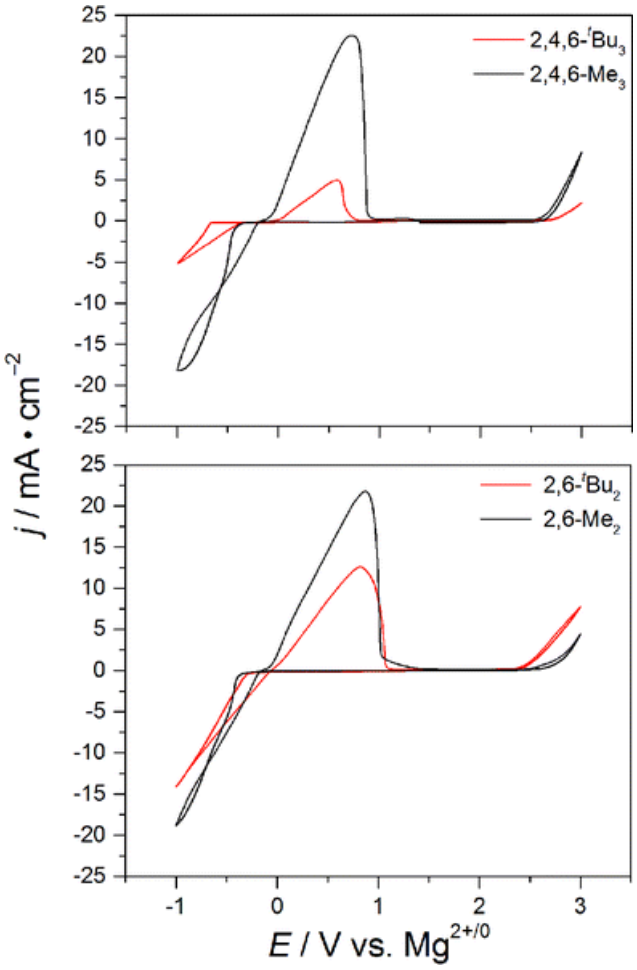

Figure 2.4. Cyclic voltammograms of 0.5 M ^{R}PhOMgCl and 0.25 M $AlCl_3$ electrolyte solutions, substitutions designated in the figure legend.

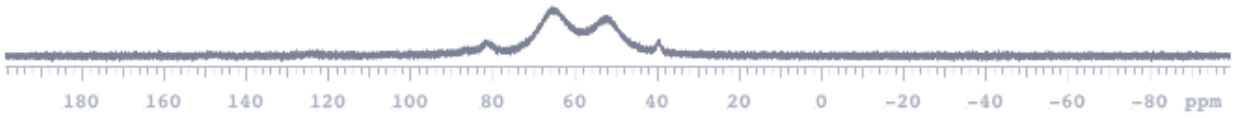

Figure 2.5. ^{27}Al NMR chemical shifts and assignments for 0.5 M ^{R}PhOMgCl and 0.25 M $AlCl_3$ (R = 2,4,6-Me_3 and 2,6-Me_2) in THF: 42 ppm $[(^{R}PhO)_4Al]^-$, 55 ppm $[((^{R}PhO)_3AlCl]^-$, 68 ppm $[(^{R}PhO)_2AlCl_2]^-$, and 84 ppm $[((^{R}PhO)AlCl_3]^-$.

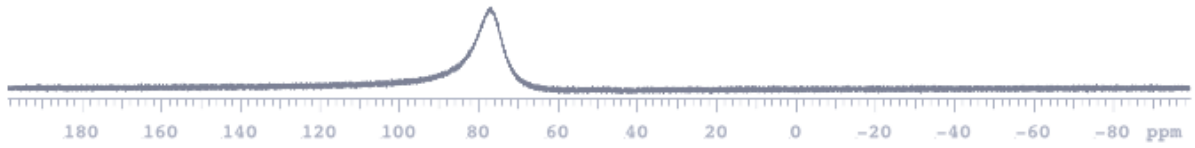

Figure 2.6. ^{27}Al NMR chemical shifts and assignments for 0.5 M ^{R}PhOMgCl and 0.25 M $AlCl_3$ (R = 2,4,6-$^{t}Bu_3$ and 2,6-$^{t}Bu_2$) in THF: 79 ppm $[(^{R}PhO)AlCl_3]^-$.

influence on anodic stability. Removing the *para*-substituents in both the methyl and *tert*-butyl systems results in decreased anodic stability (Figure 2.4, bottom). When R = $^{t}Bu_3$ or $^{t}Bu_2$, only $[^{R}PhOAlCl_3]^-$ is observed, likely due to the steric hindrance of the *tert*-butyl groups (Figure 2.6). This effect is more pronounced with *tert*-butyl than methyl being that its initial increased stabilization results from the large inductive contribution in *para*-equivalent systems. Accordingly, removing it proves to be more detrimental. Specifically, in the case of R = $^{t}Bu_2$, the combination of removing the *para*-substituent, which adds stability, and decreasing the number of aluminate anions in solution gives rise the lowest anodic stability of all our electrolytes.

2.3.3 Electrochemical Cycling of Chevrel-phase Mo_6S_8 vs Mg-foil in 0.5 M ^{R}PhOMgCl (R = 2,4,6-Me_3) and 0.25 M $AlCl_3$ electrolyte in THF

Chevrel-phase Mo_6S_8 containing batteries demonstrated the ability to facilitate ion insertion and extraction. We prepared Chevrel-phase Mo_6S_8 cathode materials by a known solid-state method.[14] 2016-type coin cells prepared in an argon-atmosphere (containing mechanically polished Mg foil as the anode and 0.5 M ^{R}PhOMgCl (R = 2,4,6-Me_3) and 0.25 M $AlCl_3$ electrolyte in THF solvent with a soaked glass fiber separator) were cycled at room temperature at *C*/10 current. The galvanostatic cycles in Figure 2.7 along with the charge–discharge curves (Figure 2.8) show gravimetric capacities consistent with reversible Mg^{2+} insertion into Chevrel-phase Mo_6S_8. Although our capacities (~63 mA h g^{-1}) are

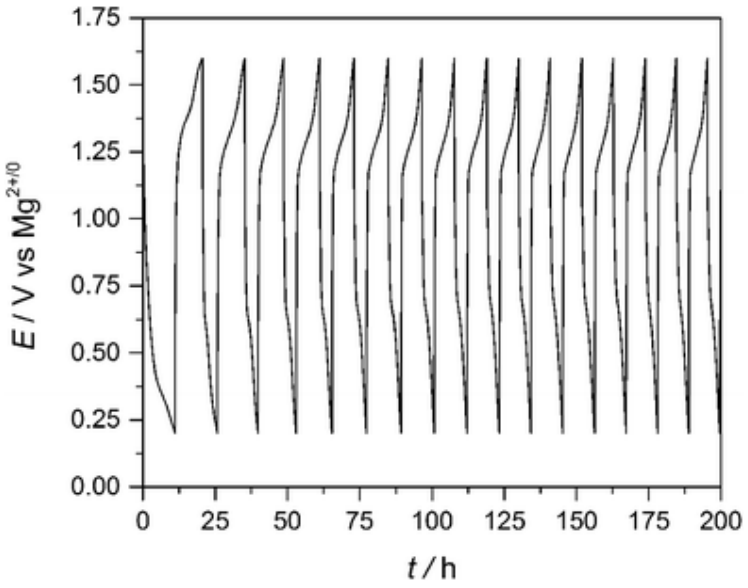

Figure 2.7. Reversible galvanostatic cycling of Mo_6S_8 vs Mg-foil at *C*/10 in 0.5 M ^{R}PhOMgCl and 0.25 M $AlCl_3$ (R = 2,4,6-Me_3) in THF electrolyte.

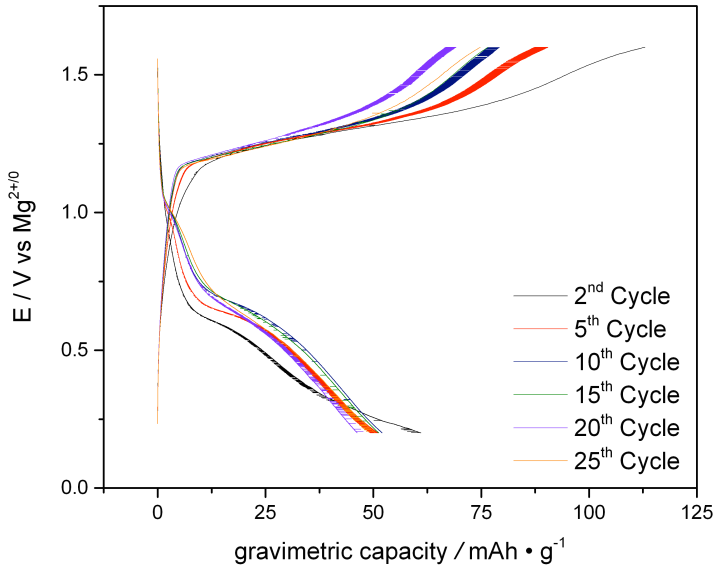

Figure 2.8. Charge–discharge curves of Mo_6S_8 vs Mg-foil in 0.5 M ^{R}PhOMgCl and 0.25 M $AlCl_3$ (R = 2,4,6-Me_3) in THF electrolyte at *C*/10.

significantly lower than the theoretical capacity of Mo_6S_8 (~130 mA h g^{-1}), they are on a par with those reported for Grignard-based Mg and $AlCl_3$ electrolytes. We also note that the

capacities we observe upon charging are greater than those observed upon discharge, likely due to parasitic corrosion of Chevrel or the current collector that occurs at higher potentials. Similar behavior is also observed in the original report.[15]

2.4 Conclusion

In summary, with the systematic substitution of a variety of alkyl-based phenols within the ^{R}PhOMgCl and $AlCl_3$ electrolyte system in THF solvent, we have demonstrated charge dissipation from the site of oxidation that results from the inductive effect of branching alkyl groups, allowing for an expansion of the electrochemical window to 2.73 V vs $Mg^{2+/0}$. Additionally, including alkyl substituents at the 2 and 6 positions yields similar anodic stabilities with a nearly two-fold enhancement in solution conductivity, allowing for future development of highly conductive and stable magnesium-ion electrolytes as we move beyond lithium-ion technologies.

2.5 References

(1) Aurbach, D.; Suresh, G. S.; Levi, E.; Mitelman, A.; Mizrahi, O.; Chusid, O.; Brunelli, M. Progress in rechargeable magnesium battery technology *Adv. Mater.* **2007**, *19*, 4260–4267.

(2) Wang, F.; Guo, Y.; Yang, J.; Nuli, Y.; Hirano, S. A novel electrolyte system without a Grignard reagent for rechargeable magnesium batteries *Chem. Commun.* **2012**, *48*, 10763– 10765.

(3) Nelson, E. G.; Kampf, J. W.; Bartlett, B. M. Enhanced oxidative stability of non-Grignard magnesium electrolytes through ligand modification *Chem. Commun.* **2014**, *50*, 5193– 5195.

(4) Benmayza, A.; Ramanathan, M.; Arthur, T. S.; Matsui, M.; Mizuno, F.; Guo, J.; Glans, P. A.; Prakash, J. Effect of electrolytic properties of a magnesium organohaloaluminate electrolyte on magnesium deposition *J. Phys. Chem. C* **2013**, *117*, 26881– 26888.

(5) Liu, T.; Cox, J. T.; Hu, D.; Deng, X.; Hu, J.; Hu, M. Y.; Xiao, J.; Shao, Y.; Tang, K.; Liu, J. A fundamental study on the $[(\mu\text{-}Cl)_3Mg_2(thf)_6]^+$ dimer electrolytes for rechargeable Mg batteries *Chem. Commun.* **2015**, *51*, 2312– 2315.

(6) Kim, H. S.; Arthur, T. S.; Allred, G. D.; Zajicek, J.; Newman, J. G.; Rodnyansky, A. E.; Oliver, A. G.; Boggess, W. C.; Muldoon, J. Structure and compatibility of a magnesium electrolyte with a sulphur cathode *Nat. Commun.* **2011**, *2*, 427– 432.

(7) Pour, N.; Gofer, Y.; Major, D. T.; Aurbach, D. Structural analysis of electrolyte solutions for rechargeable Mg batteries by stereoscopic means and DFT calculations *J. Am. Chem. Soc.* **2011**, *133*, 6270– 6278.

(8) Taft, R. W. Linear free energy relationships from rates of esterification and hydrolysis of aliphatic and ortho-substituted benzoate esters *J. Am. Chem. Soc.* **1952**, *74*, 2729– 2732.

(9) Datta, D. Taft's substituent constants, σ^* and σ_I, and Huheey's group electronegativity *Org. Chem.* **1991**, *4*(2), 96– 100.

(10) Muldoon, J.; Bucur, C. B.; Oliver, A. G.; Sugimoto, T.; Matsui, M.; Kim, H. S.; Allred, G. D.; Zajicek, J.; Kotani, Y. Electrolyte roadblocks to a magnesium rechargeable battery *Energy Environ. Sci.* **2012**, *5*(3), 5941– 5950.

(11) Guo, Y. S.; Zhang, F.; Yang, J.; Wang, F. F.; NuLi, Y. N.; Hirano, S. I. Boron-based electrolyte solutions with wide electrochemical windows for rechargeable magnesium batteries *Energy Environ. Sci.* **2012**, *5*, 9100– 9106.

(12) Breslow, R.; Höver, H.; Chang, H. W. The synthesis and stability of some cyclopropenyl cations with alkyl substituents *J. Am. Chem. Soc.* **1962**, *84*, 3168– 3174.

(13) Carter, T. J.; Mohtadi, R.; Arthur, T. S.; Mizuno, F.; Zhang, R.; Shirai, S.; Kampf, J. W. Boron clusters as highly stable magnesium-battery electrolytes *Angew. Chem., Int. Ed.* **2014**, *53*(12), 3173– 3177.

(14) Lancry, E.; Levi, E.; Gofer, Y.; Levi, M.; Salitra, G.; Aurbach, D. Leaching chemistry and the performance of the Mo_6S_8 cathodes in rechargeable Mg batteries *Chem. Mater.* **2004**, *16*, 2832– 2838.

(15) Aurbach, D.; Lu, Z.; Schechter, A.; Gofer, Y.; Gizbar, H.; Turgeman, R.; Cohen, Y.; Moshkovich, M.; Levi, E. Prototype systems for rechargeable magnesium batteries *Nature* **2000**, *407*, 724– 727.

Chapter 3

Fluorinated Alkoxide-Based Magnesium-Ion Battery Electrolytes that Demonstrate Li-Ion-Battery-Like High Anodic Stability and Solution Conductivity

Portions of this chapter have been published:

Crowe, A. J.; Stringham, K. K.; Bartlett, B. M. *ACS Appl. Mater. Interfaces* **2016**, *8*(35), 23060–23065.

3.1 Introduction

Despite the promising characteristics of a metal Mg anode, such as the comparatively negative reduction potential (−2.37 V vs NHE), high volumetric capacity (3,832 mAh cm^{-3}), and dendrite free electrodeposition[1], we do not yet buy rechargeable magnesium batteries as the accessible cell potential is low and not yet competitive with lithium. One chemistry challenge here is that electrolytes with suitable conductivity show much more narrow windows of electrochemical stability than their lithium counterparts.[2,3] Moreover, recently reported electrolytes that do show suitable anodic stabilities (>3 V vs $Mg^{2+/0}$) demonstrate low solution conductivities (<3 mS cm^{-1}).[4,5] Specifically, one promising class of electrolytes contain monocarborane salts ($Mg(CB_{11}H_{12})$) which show high anodic stability (3.6 V vs $Mg^{2+/0}$) with moderate solution conductivities (2.9 mS cm^{-1})[6] but are only accessible through a complicated recrystallization-based synthesis from relatively expensive starting materials.

As mentioned within Chapter 2, we utilized a phenolate-based electrolyte system[7] to first develop a series of structure-function relationships that would guide our future electrolyte

design. Specifically, we discovered a strong electronic effect for electrolytes composed of 0.5 M ^{R}PhOMgCl and 0.25 M $AlCl_3$ in THF.[8] Our data show that when R is strongly electron withdrawing (4-CF_3 or 2,3,4,5,6-F_5), we observe the largest stability window (out to 3.0 V vs $Mg^{2+/0}$). Next, we found that by increasing the steric bulk at the *ortho*-positions gives rise to higher solution conductivity (2.56 mS cm^{-1}).[9] Although this work harnessed the power of physical organic principles by employing the aromatic ring, the aromatic moiety is not a vital component to generate a good electrolyte. Aromatic rings were initially selected to avoid β-hydride elimination as a decomposition pathway after transmetallation. Of course, alkoxides based on ^{t}Bu could also be used to accomplish this goal. We note that electrolytes based on alkoxides (^{n}BuO) have shown modest anodic stability (2.0–2.5 V vs $Mg^{2+/0}$) with the advantage of a 2-fold increase in concentration over aromatic-based correspondents.[10]

In this chapter, we combine what we have learned regarding the importance of electron withdrawing groups with significant steric bulk to generate one of the highest anodic stability non-Grignard electrolyte to date, 3.2 V vs $Mg^{2+/0}$ starting from a readily synthesized compound, $((CF_3)_2CH_3)COMgCl$. We also show by DFT that transitioning from phenolates to alkoxides gives rise to higher anodic stability by moving the lowest energy electron from the π-system of the aromatic ring to the aluminum chloride framework.

3.2 Experimental

3.2.1 DFT Calculations

All aluminate optimizations were performed using B3LYP functionals with a 6-31+G* basis set[11–13] using Gaussian 09 package,[14] similar to methods described in previous reports.[15] Solvation was taken into account by the polarizable continuum model (THF, ε = 7.4257) using the integral equation formalism variant (IEFPCM).[16–18]

3.2.2 Synthesis of Electrolyte Solutions

All alcohols were purchased from Sigma-Aldrich and used as received. Tetrahydrofuran was purchased from EMD anhydrous and further dried by refluxing under N_2 over the ketyl radical produced by reacting sodium and benzophenone. Once loaded into the N_2 glovebox, 3 Å molecular sieves were added to the THF solvent. Aluminum chloride was purchased anhydrous and used as received from Alfa Aesar. All electrolyte solutions were prepared in a nitrogen-filled glovebox (Vacuum Atmospheres) prior to loading into an argon-filled glovebox (Vacuum Atmospheres) for electrochemical measurements. Solutions were prepared in similar fashion, with specific details provided here for the electrolyte composed of 1.2 M $((CF_3)_2CH_3)COMgCl$ and 0.2 M $AlCl_3$ in THF: 4 mL of 2 M ethylmagnesium chloride (8 mmol) in THF was slowly added to a solution 1,1,1,3,3,3-hexafluoro-2-methylpropan-2-ol (8 mmol, 0.98 mL) dissolved in dry THF (0.35 mL) by syringe. The resulting gray transparent solution was left to stir overnight, forming $((CF_3)_2CH_3)COMgCl$. Then, 1.3 mL of a 1.0 M solution of $AlCl_3$ (1.3 mmol) in THF was prepared in a 20 mL scintillation vial at 0 °C, warmed to room temperature, and then added to the alkoxidemagnesium chloride solution. This solution was stirred for 8 h, providing a clear colorless solution.

3.2.3 Electrolyte Solution Characterization

Cyclic voltammograms were recorded using a CH Instruments Electrochemical Workstation 660C while using a Pt-disk working electrode (CHI) and Mg-foil (MTI) counter- and reference electrodes. Measurements were performed in a custom-designed, three-necked, sealed glass cell starting at the open circuit potential (typically 2 V vs $Mg^{2+/0}$) and scanned to more negative electrochemical potentials. Conductivity measurements were obtained using a YSI model 3200 m equipped with a 3253 conductivity cell at room temperature.

^{27}Al NMR spectra were recorded on a Varian VNMRS-700 MHz spectrometer in J. Young NMR tubes in the University of Michigan–Ann Arbor Department of Chemistry NMR facility. Chemical shifts of solutions in THF were reported relative to a solution of $AlCl_3$ in D_2O with a drop of concentrated HCl.

Transference numbers (t_+) were estimated assuming deposition directly from Mg^{2+}, as described in a previous report.[19] In brief, chronopotentiometry was used to deposit Mg metal from 1 mL of electrolyte onto a Pt-disk working electrode, and metallic Mg strips were used as reference- and counter electrodes. A controlled quantity of charge was passed between the electrodes, and magnesium deposits were then digested in 10 mL of a 0.1 M HNO_3 solution. This solution was analyzed with ICP-AES for Mg^{2+} using a PerkinElmer Optima 2000DV. Samples were referenced to an yttrium internal standard and concentrations of magnesium were determined from the maximum intensity compared to those of standard reference solutions.

3.2.4 Electrochemical Cell Preparation and Measurements

Battery function was tested by galvanostatic cycling using Chevrel-phase Mo_6S_8. A slurry of Mo_6S_8 was prepared by mixing a 75:15:10 (by weight) ratio of Mo_6S_8, super-P carbon powder, and polyvinylidine fluoride (PVDF) binder, suspended in *N*-methyl-2-pyrrolidinone (NMP). The active material loading was approximately 2 mg cm^{-2}. The slurry was cast onto a Type 316 stainless steel current collector (McMaster-Carr) by the doctor blade method, then dried in an oven at 120 °C, placed in a 2016-type coin cell with a Mg-foil anode and a soaked glass fiber separator in 1.2 M $((CF_3)_2CH_3)COMgCl$ and 0.2 M $AlCl_3$ electrolyte dissolved in THF. Cycling was carried out on a Vencon UBA4 battery analyzer charger and conditioner (Toronto, Canada) with cutoff voltages of 1.6 and 0.2 V vs $Mg^{2+/0}$.

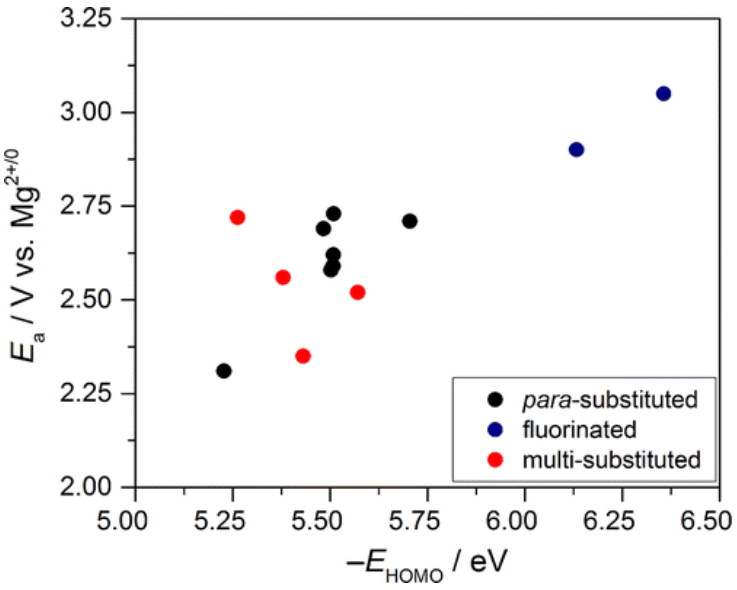

Figure 3.1. Anodic stability vs calculated HOMO of $ROAlCl_3^-$ in THF for our previously reported electrolytes.

3.3 Results and Discussion

3.3.1 Density Functional Theory Guided Electrolyte Design

Given our finding that electronic factors (the σ^+ Hammet parameter) govern anodic stability in substituted phenolate-based electrolytes, we turned to density functional theory (DFT) to guide our search for promising alkoxide electrolytes. We postulate that the most easily oxidized species in solution is the aluminate anion, and although several aluminates are observable by ^{27}Al-NMR spectroscopy,[8,9] we use the monosubstituted $[^{R}PhOAlCl_3]^-$ anion for comparative purposes. We use Becke, 3-parameter, Lee–Yang–Parr (B3LYP) exchange-correlation functionals, and note that for the C, H, O, Al, and Cl-containing anions, the 6-31+G* basis set including s, p, and d polarization is appropriate for accuracy.

To test predictive trends, we started by calculating the HOMO energies of the phenolate-based aluminate anions derived from previously synthesized electrolytes in our group. The

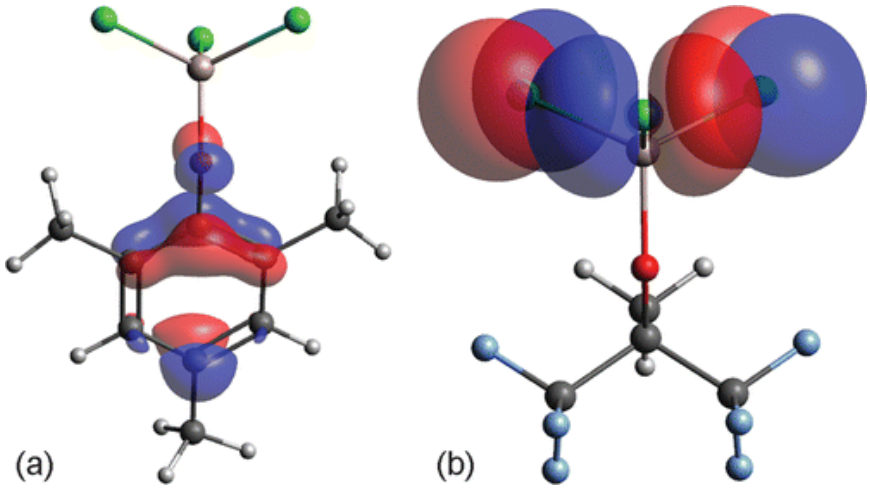

Figure 3.2. (a) Visualization of the HOMO for $^{R}PhOAlCl_3^-$ (R = 2,4,6-Me_3), and (b) $((CF_3)_2(CH_3))COAlCl_3^-$.

results in Figure 3.1 (black and blue data points) show the same general trend as we observed in our *E* vs σ^+ data in our previous manuscript.[8,9] Including sterics (red data points) adds some noise to the trend in the data, but in all of these anions, C–C π orbitals in the aromatic ring comprise the HOMO. As a specific example, 0.5 M $^{R}PhOMgCl$ and 0.25 M $AlCl_3$ (R = 2,4,6-Me_3) in THF shows moderate anodic stability (2.56 V vs $Mg^{2+/0}$) with high solution conductivity (2.56 mS cm^{-1}). The HOMO of the monosubstituted aluminate projected in Figure 3.2a shows electron density localized on the phenoxide ligand, with a calculated energy (approximate negative ionization potential) of −5.38 eV using THF solvent in a polarizable continuum model.

To expand the electrochemical stability window, we hypothesize that shifting electron density from the organic moiety to the inorganic aluminum chloride framework is necessary. With the aforementioned design principles in mind, fluorinated *tert*-butyl derivatives display all of the necessary components to do just that: (1) there are no β-hydrogens to introduce unwanted side reactions; (2) multiple electron-withdrawing trifluoromethyl groups can be incorporated for

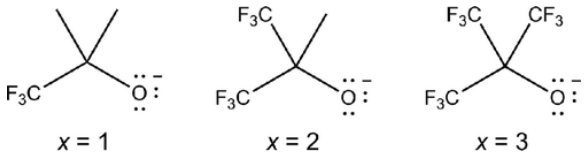

Figure 3.3. Lewis structures of alkoxide precursors.

high anodic stability; (3) the large steric bulk of the *tert*-butyl group should provide excellent solution conductivity because of weaker ion pairing between a magnesium cation and aluminate anion.

Encouraged by the correlation between HOMO energy and anodic stability observed in our previous data, we began exploring new potential electrolytes by carrying out similar DFT calculations to guide us. Again, we draw conclusions from the calculated monosubstituted aluminates $[((CF_3)_x(CH_3)_{3-x})COAlCl_3]^-$ (x = 1–3), where x designates the number of trifluoromethyl substituents encompassing the *tert*-butanol-based electrolyte precursor (Figure 3.3), because of the low computing power needed for these anions. The number of configurational degrees of freedom in the significantly larger $[(RO)_2AlCl_2]^-$ and $[(RO)_3AlCl]^-$ anions, likely due to the low barrier to rotation about the C–C σ bonds, posed a great computational challenge. Although several aluminates may be present in solution (confirmed *vide infra*), we posit that comparing the monosubstituted aluminates is a reasonable approach since there is good electronic correlation for the phenolate electrolytes. Table 3.1 summarizes the HOMO and LUMO energies, along with the HOMO–LUMO gap (Δ) for the various proposed *tert*-butoxide chloro–aluminates. In accord with our hypothesis, the HOMO of $[((CF_3)_2CH_3)COAlCl_3]^-$ in THF (Figure 3.2b) suggests initial electrooxidation begins with electron abstraction from the nonbonding electrons on the chloride ligands, instead of bonding electrons on the alkoxide ligand.

anion	E_{HOMO} (eV)	E_{LUMO} (eV)	Δ (eV)
$AlCl_4^-$	−7.64	0.04	7.69
$[((CF_3)\ (CH_3)_2)COAlCl_3]^-$	−7.14	0.19	7.33
$[((CF_3)_2(CH_3))COAlCl_3]^-$	−7.57	0.17	7.74
$[((CF_3)_3)COAlCl_3]^-$	−7.63	0.10	7.73
$[(((CF_3)_2(CH_3)CO)_4Al]^-$	−7.40	0.30	7.70

Table 3.1. Summary of HOMO, LUMO, and energy difference in eV for organochloroaluminates in THF.

The data show that increasing fluorination on the alkoxide results in increasingly stable ions (E_{HOMO} becomes larger in magnitude and more negative) and that all of these anions are more stable than the phenolates. Additionally, the similarity in E_{HOMO} to $[AlCl_4]^-$ suggests that these electrolytes approach the maximum stability for aluminum chloride Lewis acid-stabilized electrolyte compositions. For completeness, we did calculate the energies for the tetrakis-substituted $[Al(((CF_3)_2(CH_3))CO)_4]^-$ anion, and observe a slight decrease in expected stability when comparing it to the monosubstituted aluminate above, −7.40 and −7.57 eV, the last entry in Table 3.1. This energy difference is relatively small, and the decrease in E_{HOMO} with decreasing inorganic character has also been observed with the Grignard-based examples.[15] Therefore, we conclude from these DFT calculations that the degree of fluorination and the inorganic character are competing factors in describing stability.

3.3.2 Effect of Fluorination on Solution Speciation and Electrochemical Stability

Armed with our DFT results, we prepared these fluorinated electrolytes to measure their anodic stabilities as a function of number of CF_3 groups, x. We synthesized $((CF_3)_x(CH_3)_{3-x})COMgCl$ from ethylmagnesium chloride and the appropriate alcohol according the reaction:

$$(C_2H_5)MgCl + ((CF_3)_x(CH_3)_{3-x}COH \longrightarrow ((CF_3)_x(CH_3)_{3-x}COMgCl + C_2H_6$$

in accord with what has been previously described.[10] We then added an aluminum chloride in

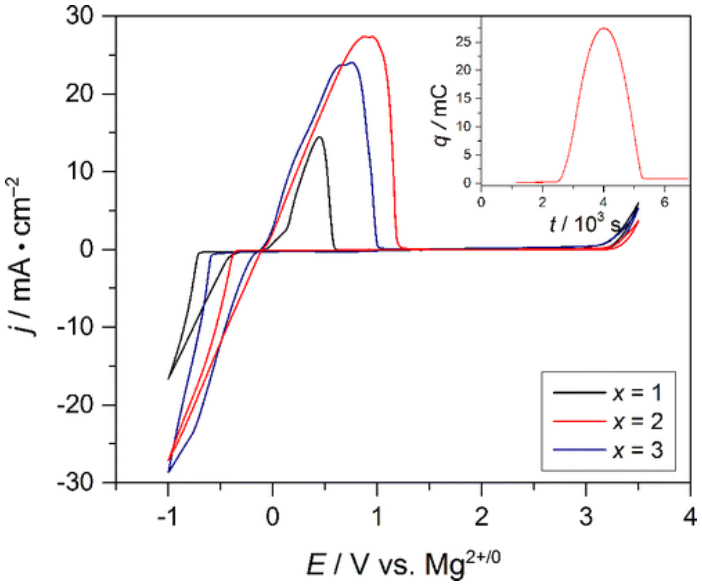

Figure 3.4. Cyclic voltammograms of the optimized concentrations for R = 1–3-CF_3 electrolyte solutions in THF.

magnesium salt[a]	E_a/V vs $Mg^{2+/0}$	σ (mS cm^{-1})	CE (%)
0.8 M $((CF_3)(CH_3)_2)CO$-MgCl	3.08	2.8	57
1.2 M $((CF_3)_2(CH_3))CO$-MgCl	3.20	3.5	98
1.2 M $((CF_3)_3)COMgCl$	3.11	2.5	85

[a]For a Mg^{2+} concentration of y M in THF, the electrolytes contain $y/6$ M $AlCl_3$.

Table 3.2. Anodic stability (potential vs $Mg^{2+/0}$), solution conductivity, and Coulombic efficiency for deposition–dissolution of the fluorinated alkoxide-based electrolytes.

THF solution to the alkoxidemagnesium chloride (x = 1, 2, and 3) and optimized the concentration for highest solution conductivity. When x = 2 or 3, solutions composed of 1.2 M Mg and 0.2 M Al are soluble. The solubility of the x = 1 complex, $((CF_3)(CH_3)_2)COMgCl$ is less, with a maximum concentration of 0.8 M Mg.

Figure 3.4 shows the cyclic voltammograms of the three prepared electrolytes, and we tabulate the experimentally measured anodic stabilities, solution conductivities, and Coulombic

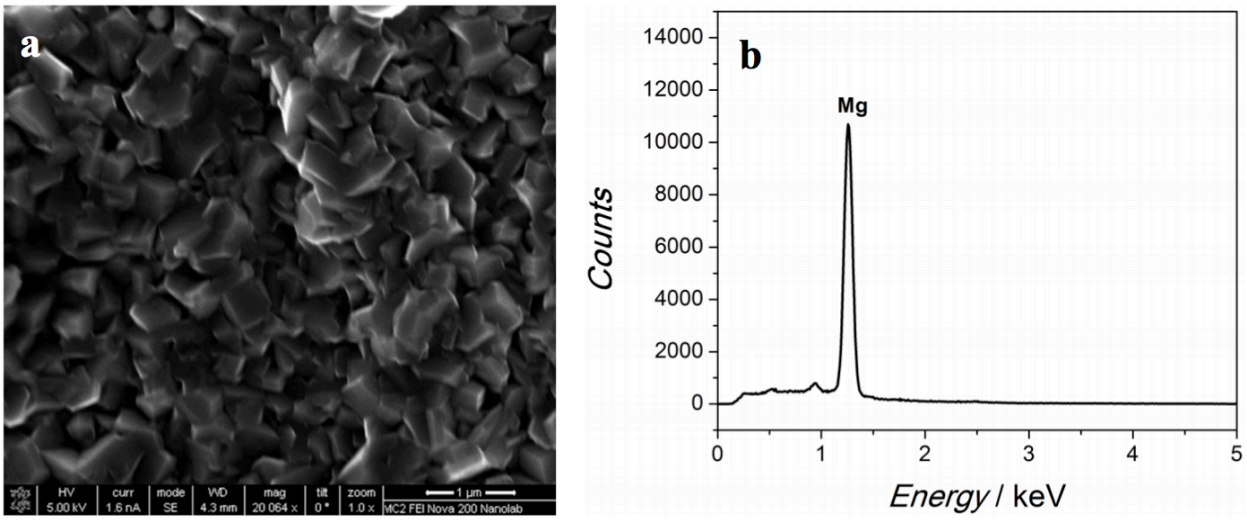

Figure 3.5. (a) SEM image and (b) EDX spectrum of deposited magnesium on Cu foil from 1.2 M$((CF_3)_2CH_3)$COMgCl and 0.2 M $AlCl_3$ in THF electrolyte at 2 mA cm^{-2} (0.8 C cm^{-2}).

efficiencies in Table 3.2. A solution composed of 1.2 M $((CF_3)_2(CH_3))$COMgCl and 0.20 M $AlCl_3$ exhibits an anodic stability of 3.2 V vs $Mg^{2+/0}$, on a par with the most anodically stable magnesium-ion electrolyte compositions previously reported.[6,20] We also observe low overpotentials for deposition and stripping from the $x = 2$ electrolyte, 0.35 and 0 V, respectively. This composition also shows a solution conductivity of 3.5 mS cm^{-1} at room temperature, which surpasses what has been reported for non-Grignard electrolytes.[2,6,21] Additionally, the $((CF_3)_2(CH_3))$COMgCl-based electrolyte shows 98% Coulombic efficiency for magnesium deposition and stripping on a Pt-disk working electrode in the inset of Figure 3.4. Mg^{2+} reduction to Mg^0 metal was confirmed by galvanostatic deposition (2 mA cm^{-2}, 0.8 C cm^{-2} total charge passed) on a copper foil electrode from 1.2 M $((CF_3)_2(CH_3))$COMgCl and 0.20 M $AlCl_3$ in THF solution. The SEM image in Figure 3.5a shows typical compact pyramid-shaped Mg crystals,[22] and EDX analysis (Figure 3.5b) confirms Mg-metal deposition.

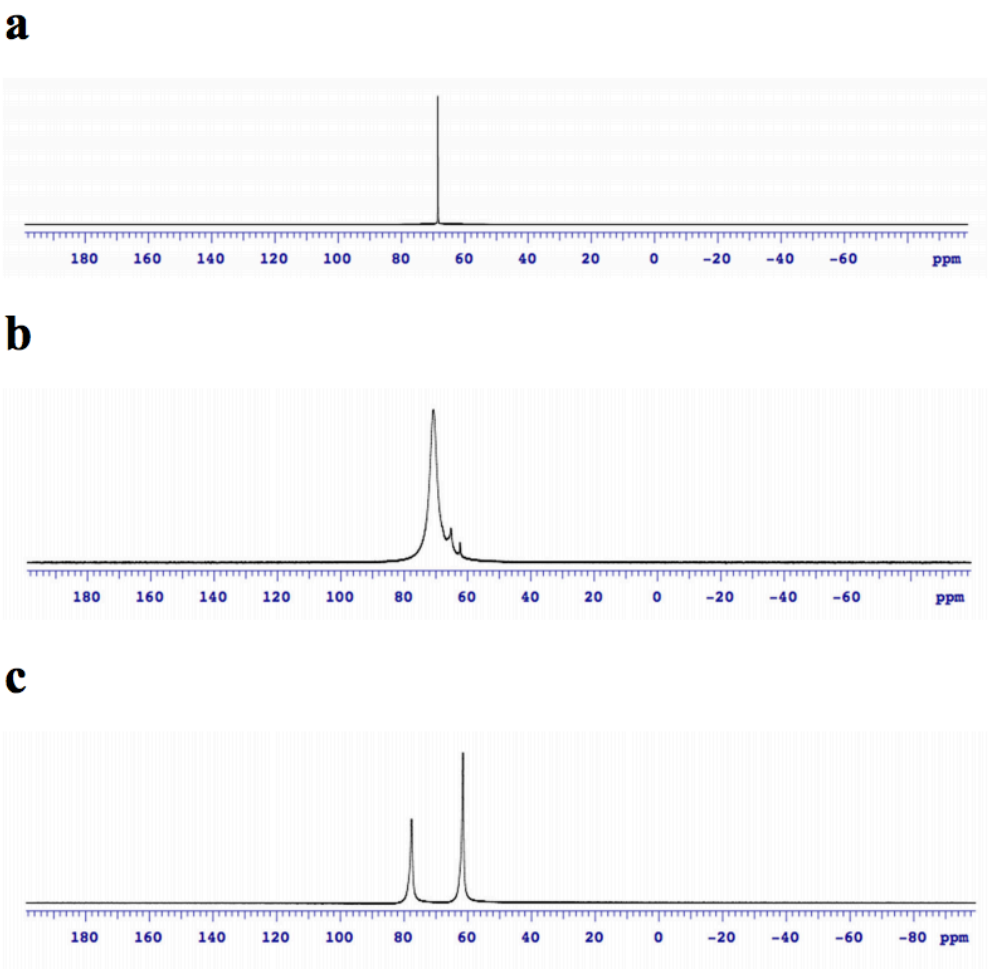

Figure 3.6. ^{27}Al NMR chemical shifts and assignments for THF solutions composed of (a) 0.8 M $((CF_3)(CH_3)_2)COMgCl$ and 0.13 M $AlCl_3$: 68 $[(^{R3}CO)_4Al]^-$; (b) 1.2 M $((CF_3)_2(CH_3))COMgCl$ and 0.2 M $AlCl_3$: 71 $[(^{R3}CO)_3AlCl]^-$, 65 $[(^{R3}CO)_4Al]^-$, and 62 $AlCl_3$; (c) 1.2 M $((CF_3)_3)COMgCl$ and 0.2 M $AlCl_3$: 78 $[(^{R3}CO)_2AlCl_2]^-$ and 61 $[(^{R3}CO)_4Al]^-$.

We note that the largest stability window results when $x = 2$, not 3. ^{27}Al-NMR spectroscopy (Figure 3.6) sheds some light on this 90 mV increase in anodic stability. We observe both the tris- and tetrakis-alkoxides in the NMR spectrum for $x = 2$ ($[(((CF_3)_2CH_3)CO)_3AlCl]^-$ and $[(((CF_3)_2(CH_3))CO)_4Al]^-$). But, we observe only the tetrakisalkoxide in the x = 3 case ($[(((CF_3)_3CO)_4Al]^-$), which is predicted to be less stable than its

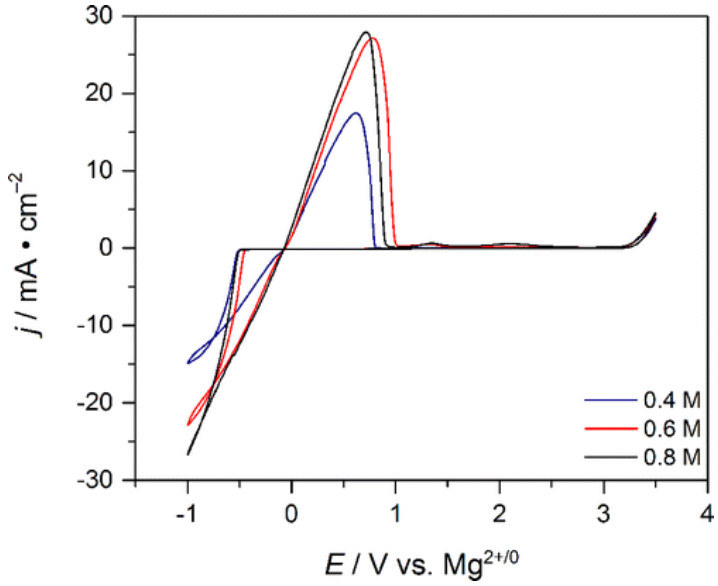

Figure 3.7. Cyclic voltammogram of varied concentration of *y* M ($(CF_3)_2CH_3COMgCl$) and *y*/6 M $AlCl_3$ (*y* = 0.8, 0.6, and 0.4 M) in THF solutions, as designated in the figure legend.

trisalkoxide congener. When *x* = 1, not only is the solubility worse, but the electrochemical characteristics are not suitable for battery applications. We surmise this is due to the increased basicity of the $[CF_3(CH_3)_2CO]^-$, which shows only the less soluble and less stable $[Al(((CF_3)(CH_3)_2)CO)_4]^-$ anion.[23] Additionally, we expect the strong ion-pairing with the accompanying cationic magnesium species to give rise to the low C**ou**l**o**mbic efficiency, only 57%.

To hone further the likely Mg^{2+} species responsible for Mg^0 deposition, we estimate the transference number (t_+) according to the equation:

$$t_+ = 1 - (z_+ F \Delta C^* V/q)$$

where z_+ is the cation valency (= 1), *F* is Faraday's constant 26.801 mAh $mmol^{-1}$, ΔC^* is the change in bulk magnesium ion concentration (2.69 mmol L^{-1}), *V* is the volume of electrolyte

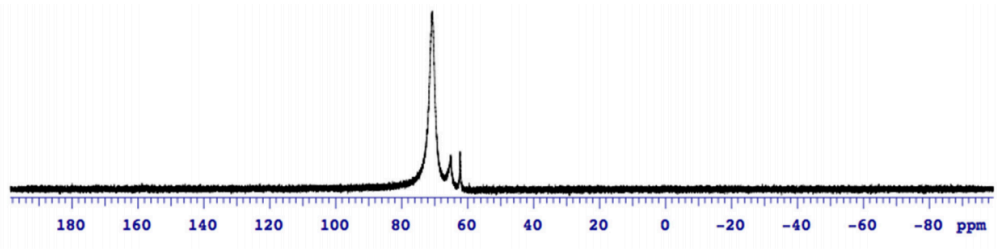

Figure 3.8. ^{27}Al NMR chemical shifts and assignments for y M $((CF_3)_2(CH_3))COMgCl$ and $y/6$ M $AlCl_3$ (y = 0.8, 0.6, and 0.4 M) in THF: 71 $[(^{R3}CO)_3AlCl]^-$, 65 $[(^{R3}CO)_4Al]^-$, and 62 $AlCl_3$.

(10^{-3} L), and q is the charge passed (0.13 mAh). We note from Faraday's law that the theoretical change in Mg^{2+} concentration is 5.89 ppm for a divalent cation (z^+ = 2) and 23.58 ppm for a monovalent cation (z_+ = 1). From ICP-AES elemental analysis, we find 6.535 ppm of Mg^{2+} in solution. Therefore, only a monovalent cation (z_+= 1) provides meaningful t_+ of 0.45. Consequently, this measurement suggests that the presumed cationic species $[Mg_2(\mu\text{-}Cl)_3(THF)_6]^+$ contributes directly to Mg deposition and stripping via two coupled 1-electron transfers.

3.3.3 The Role of Solvation on Solution Speciation and Electrochemical Properties

To better probe the solution speciation, we diluted the x = 2 electrolyte by preparing a series of y M $((CF_3)_2CH_3)COMgCl$ and $y/6$ M $AlCl_3$ (y = 0.8, 0.6, and 0.4) in THF and then measured their CVs. Figure 3.7 shows that for the entire series, the anodic stability is the same. As expected, the current density decreases with decreasing solution concentration. However, the ^{27}Al-NMR spectra in Figure 3.8 are the same for each of these compositions. With no expansion of the electrochemical window as the amount of THF increased, the formation of the more oxidatively stable $R_3Al{\cdot}THF$ (R = $((CF_3)_2CH_3)CO^-$ or Cl^-) appears unlikely.[15]

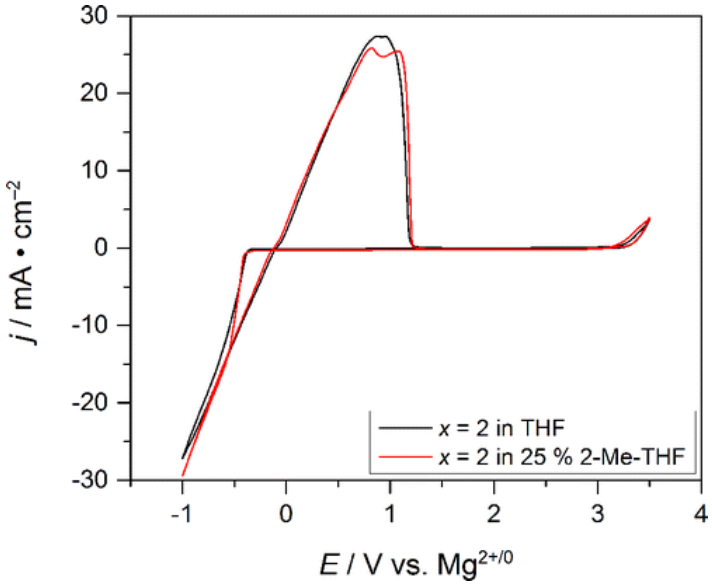

Figure 3.9. Comparison of cyclic voltammograms of 1.2 M $(CF_3)_2CH_3COMgCl$ and 0.2 M $AlCl_3$ in THF and 75% THF and 25% 2-methyl-THF solutions.

We are largely blind to the magnesium species present in solution. Although X-ray crystal structures of the famous $[Mg_2(\mu\text{-}Cl)_3(THF)_6]^+$ dimeric complex presented in the introduction abound, there is no way of knowing if this is the only species in solution or if it is merely one among several species in an equilibrium mixture that happens to be the one that supersaturates. Moreover, the I= 5/2 nucleus of ^{25}Mg with a low relative sensitivity (10^{-3} with respect to ^{1}H) makes NMR spectroscopy difficult to collect for magnesium electrolytes. In order to determine whether the THF solvent impacts solution conductivity or the Coulombic efficiency for magnesium deposition/stripping, we prepared electrolytes with 25% 2-methyltetrahydrofuran (2-Me-THF). Our idea is that the methyl group may impede dimer formation. The CV in Figure 3.9 shows that both deposition and dissolution occur with nearly the same current densities in THF and 2-Me-THF. The only difference is that the dissolution wave shows a reproducible dip at

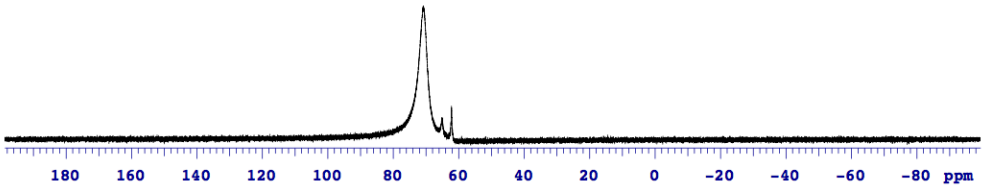

Figure 3.10. ^{27}Al NMR chemical shifts and assignments for 1.2 M $((CF_3)_2(CH_3))COMgCl$ and 0.2 M $AlCl_3$ in 75% THF and 25% 2-methyl-THF solution: 71 $[(^{R3}CO)_3AlCl]^-$, 65 $[(^{R3}CO)_4Al]^-$, and 62 $AlCl_3$.

~0.8 V vs $Mg^{2+/0}$. We surmise this phenomenon is due to an additional overpotential required for reforming the active cationic magnesium species with 2-Me-THF solvation vs THF solvation. Most important, the anodic stability is maintained for moving from THF to 25% 2-Me-THF solution, and the aluminate anions in solution are the same (Figure 3.10). We do note a 2% decrease in C**ou**l**o**mbic efficiency (96%) for 2-Me THF-containing electrolytes.

In attempt to determine the products formed at positive anodic bias, we carried out extended electrolysis (4 V vs $Mg^{2+/0}$ for 16 h) on the $x = 2$ electrolyte solution. The resulting solution was then distilled and we probed solvent identity by ^{1}H and ^{13}C NMR spectroscopy. Only peaks characteristic of THF solvent are apparent. We attempted to identify higher-boiling chlorinated solvents which could form if $Cl^{\bullet}$ radical were generated by performing fractional distillation. We see no such species. Overall, these results suggest that either Cl_2 or other chloroaluminates are the oxidized products, giving promise to examine fluorinated alkoxide-based electrolytes in other solvents, such as glymes.

3.3.4 Electrochemical Cycling of Chevrel-phase Mo_6S_8 vs Mg-foil in 1.2 M $((CF_3)_2(CH_3))COMgCl$ and 0.2 M $AlCl_3$ in THF

Finally, we demonstrate reversible Mg^{2+} insertion and extraction in a 2016-type coin cell

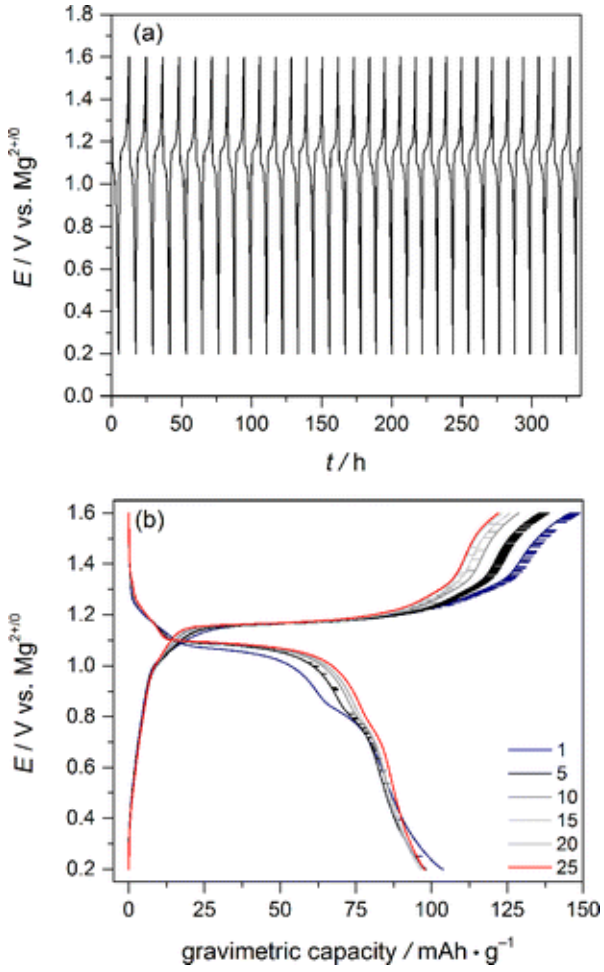

Figure 3.11. (a) Chronopotentiometric charge–discharge curves for a 2016 Mg coin-cell composed of 1.2 M $((CF_3)_2(CH_3))COMgCl$ and 0.20 M $AlCl_3$ in THF solvent and (b) data plotted as gravimetric capacity.

prepared under argon-atmosphere. The cell is composed of Chevrel-phase Mo_6S_8, which was prepared by a known solid-state method,[24] and mechanically polished Mg foil as the cathode and anode, respectively. The Chevrel-phase Mo_6S_8 is employed as a test material for cycling because the multidirectional channels allow for efficient transport of the small, but highly charged Mg^{2+} ion.

We use a glass fiber separator soaked in 1.2 M $((CF_3)_2(CH_3))COMgCl$ and 0.20 M $AlCl_3$ in THF solvent to complete the cell. Figure 3.11 shows reversible galvanostatic cycles,

with an initial discharge capacity of 104 mAh g^{-1} at C/5 current (40 mA). There is 94% capacity retention after the 25th cycle. We also note the greater capacity during charging is likely due to parasitic corrosion of the current collector as result of high chloride content in solution. This phenomena has been observed when comparing halogen-containing and halogen-free electrolytes under similar cycling conditions.[6] An additional voltage plateau was observed for the first discharge cycle, which is characteristic of intercalation within one of the two locations within the Chevrel Phase Mo_6S_8. Subsequent cycles demonstrate a loss of gravimetric capacity and the absence of the initial plateau, suggesting charge trapping due to the closely located ring arrangement for cation sites within the sulfide host.[25]

3.4 Conclusions

With use of the structure–function relationships previously developed in our group and DFT calculations, we have prepared a series of high performance electrolytes. The solution composed of 1.2 M $((CF_3)_2(CH_3))COMgCl$ and 0.20 M $AlCl_3$ in THF demonstrates stability to 3.2 V vs $Mg^{2+/0}$ on a Pt-disk working electrode with 3.5 mS cm^{-1} measured solution conductivity. Additionally, excellent galvanostatic cycling and capacity retention was observed with over 300 h of cycle time. Corrosion from the high chloride content limits longer-term cycling, so present work focuses on generating solutions with improved stainless steel compatibility. Overall our work suggests that fluorinated alkoxide-based electrolytes are promising candidates for practical magnesium-ion battery systems.

3.5 References

(1) Matsui, M. Study on electrochemically deposited Mg metal *J. Power Sources* **2011***, 196,* 7048– 7055.

(2) Mohtadi, R.; Mizuno, F. Magnesium batteries: current state of the art, issues and future perspectives *Beilstein J. Nanotechnol.* **2014**, *5*, 1291– 1311.

(3) Crowe, A. J.; Bartlett, B. M. Solid state cathode materials for secondary magnesium-ion batteries that are compatible with magnesium metal anodes in water-free electrolyte *J. Solid State Chem.* **2016**, *242*, 102– 106.

(4) Zhao-Karger, Z.; Zhao, X.; Fuhr, O.; Fichtner, M. Bisamide based non-nucleophilic electrolytes for rechargeable magnesium batteries *RSC Adv.* **2013**, *3*, 16330– 16335.

(5) Guo, Y.; Zhang, F.; Yang, J.; Wang, F. Electrochemical performance of novel electrolyte solutions based on organoboron magnesium salts *Electrochem. Commun.* **2012**, *18*, 24– 27.

(6) Tutusaus, O.; Mohtadi, R.; Arthur, T. S.; Mizuno, F.; Nelson, E. G.; Sevryugina, Y. V. An efficient halogen-free electrolyte for use in rechargeable magnesium batteries *Angew. Chem., Int. Ed.* **2015**, *54*, 7900– 7904.

(7) Wang, F.; Guo, Y.; Yang, J.; Nuli, Y.; Hirano, S. A novel electrolyte system without a Grignard reagent for rechargeable magnesium batteries *Chem. Commun.* **2012**, *48*, 10763– 10765.

(8) Nelson, E. G.; Kampf, J. W.; Bartlett, B. M. Enhanced oxidative stability of non-Grignard magnesium electrolytes through ligand modification *Chem. Commun.* **2014**, *50*, 5193– 5195.

(9) Crowe, A. J.; Bartlett, B. M. Influence of steric bulk on the oxidative stability of phenolate-based magnesium-ion battery electrolytes *J. Mater. Chem. A* **2016**, *4*, 368– 371.

(10) Liao, C.; Guo, B.; Jiang, D.; Custelcean, R.; Mahurin, S. M.; Sun, X.-G.; Dai, S. Highly soluble alkoxide magnesium salts for rechargeable magnesium batteries *J. Mater. Chem. A* **2014**, *2*, 581– 5840.

(11) Becke, A. D. Density-functional thermochemistry.III. The role of exact exchange *J. Chem. Phys.* **1993**, *98*, 5648– 5652.

(12) Lee, C.; Yang, W.; Parr, R. G. Development of the Colle-Salvetti correlation-energy formula into a functional of the electron density *Phys. Rev. B: Condens. Matter Mater. Phys.* **1988**, *37*, 785– 789.

(13) Hehre, W. J.; Radom, L.; Schleyer, P. V. R.; Pople, J. A. *Ab Initio Molecular Orbital Theory*; John Wiley & Sons: New York, **1986**.

(14) Frisch, M. J.; Trucks, G. W.; Schlegel, H. B.; Scuseria, G. E.; Robb, M. A.; Cheeseman, J. R.; Scalmani, G.; Barone, V.; Mennucci, B.; Petersson, G. A.; Nakatsuji, H.; Caricato, M.; Li, X.; Hratchian, H. P.; Izmaylov, A. F.; Bloino, J.; Zheng, G.; Sonnenberg, J. L.; Hada, M.; Ehara, M.; Toyota, K.; Fukuda, R.; Hasegawa, J.; Ishida, M.; Nakajima, T.; Honda, Y.; Kitao, O.; Nakai, H.; Vreven, T.; Montgomery, J. A., Jr.; Peralta, J. E.; Ogliaro, F.; Bearpark, M.; Heyd, J. J.; Brothers, E.; Kudin, K. N.; Staroverov, V. N.; Kobayashi, R.; Normand, J.; Raghavachari, K.; Rendell, A.; Burant, J. C.; Iyengar, S. S.; Tomasi, J.; Cossi, M.; Rega, N.; Millam, J. M.; Klene, M.; Knox, J. E.; Cross, J. B.; Bakken, V.; Adamo, C.; Jaramillo, J.; Gomperts, R.; Stratmann, R. E.; Yazyev, O.; Austin, A. J.; Cammi, R.; Pomelli, C.; Ochterski, J. W.; Martin, R. L.; Morokuma, K.; Zakrzewski, V. G.; Voth, G. A.; Salvador, P.; Dannenberg, J. J.; Dapprich, S.; Daniels, A. D.; Farkas, Ö.; Foresman, J. B.; Ortiz, J. V.; Cioslowski, J.; Fox, D. J. *Gaussian 09*, revision A.02; Gaussian, Inc.: Wallingford, CT, **2009**.

(15) Pour, N.; Gofer, Y.; Major, D. T.; Aurbach, D. Structural analysis of electrolyte solutions for rechargeable Mg batteries by stereoscopic means and DFT calculations *J. Am. Chem. Soc.* **2011**, *133*, 6270– 6278.

(16) Cancès, E.; Mennucci, B.; Tomasi, J. A new integral equation formalism for the polarizable continuum model: theoretical background and applications to isotropic and anisotropic dielectrics *J. Chem. Phys.* **1997**, *107*, 3032– 3041.

(17) Mennucci, B.; Cancès, E.; Tomasi, J. Evaluation of solvent effects in isotropic and anisotropic dielectrics and in ionic solutions with a unified integral equation method: theoretical bases, computational implementation, and numerical applications *J. Phys. Chem. B* **1997**, *101*, 10506– 10517.

(18) Tomasi, J.; Mennucci, B.; Cancès, E. The IEF version of the PCM solvation method: an overview of a new method addressed to study molecular solutes at the QM ab initio level *J. Mol. Struct.: THEOCHEM* **1999**, *464*, 211– 226.

(19) Benmayza, A.; Ramanathan, M.; Arthur, T. S.; Matsui, M.; Mizuno, F.; Guo, J.; Glans, P. A.; Prakash, J. Effect of electrolytic properties of a magnesium organohaloaluminate electrolyte on magnesium deposition *J. Phys. Chem. C* **2013**, *117*, 26881– 26888.

(20) Mizrahi, O.; Amir, N.; Pollak, E.; Chusid, O.; Marks, V.; Gottlieb, H.; Larush, L.; Zinigrad, E.; Aurbach, D. Electrolyte solutions with a wide electrochemical window for rechargeable magnesium batteries *J. Electrochem. Soc*. **2008**, *155*, A103– A109.

(21) Yoo, H. D.; Shterenberg, I.; Gofer, Y.; Gershinsky, G.; Pour, N.; Aurbach, D. Mg rechargeable batteries: an on-going challenge *Energy Environ. Sci.* **2013**, *6*, 2265– 2279.

(22) Aurbach, D.; Weissman, I.; Gofer, Y.; Levi, E. Nonaqueous magnesium electrochemistry and its application in secondary batteries *Chem. Rec.* **2003**, *3*, 61– 73.

(23) Aurbach, D.; Gizbar, H.; Schechter, A.; Chusid, O.; Gottlieb, H. E.; Gofer, Y.; Goldberg, I. Electrolyte solutions for rechargeable magnesium batteries based on organomagnesium chloroaluminate complexes *J. Electrochem. Soc.* **2002**, *149*, A115– A121.

(24) Lancry, E.; Levi, E.; Gofer, Y.; Levi, M.; Salitra, G.; Aurbach, D. Leaching chemistry and the performance of the Mo_6S_8 cathodes in rechargeable Mg batteries *Chem. Mater.* **2004**, *16*, 2832– 2838.

(25) Levi, E.; Lancry, E.; Mitelman, A.; Aurbach, D.; Ceder, G.; Morgan, D.; Isnard, O. Phase diagram of Mg insertion into Chevrel Phases, $Mg_xMo_6T_8$ (T = S, Se). 1. Crystal structure of the sulfides *Chem. Mater.* **2006**, *18*, 5492– 5503.

Chapter 4

Kinetics of Magnesium Deposition and Stripping from Non-Aqueous Electrolytes

Portions of this chapter have been published:

Crowe, A. J.; DiMeglio, J. L.; Stringham, K. K.; Bartlett, B. M. *J. Phys. Chem. C* **2017***, 121*(38), 20613–20620.

4.1 Introduction

Initial reports on Grignard-based electrolyte solutions showed that the metal employed as the working electrode dictates the resulting morphology of magnesium during electrodeposition.[1] While irregular deposits were observed on Ni and Cu substrates, Au and Ag working electrodes allowed for well-defined deposits with complete electrode coverage. Matsui further studied Grignard-based solutions while comparing the deposition properties of an alkyl-based electrolyte solution to $LiPF_6$ in ethylene carbonate and diethylcarbonate, emphasizing the lack of dendrite formation during Mg-ion cycling.[2] These results were attributed to the comparatively higher deposition overpotential for Mg, which suppresses the localization of what would result in dendritic growth.

While many research groups have put emphasis on designing new electrolyte solutions that show high anodic stability and solution conductivity,[3–5] few studies have been put forth that probe further than these basic properties. From a chemical analysis perspective, a recent report

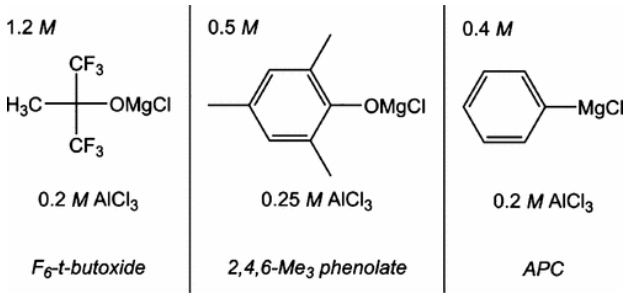

Figure 4.1. Structures of electrolyte components used in this work.

demonstrated that a simple electrolyte solution composed of magnesium bis(trifluoromethanesulfonyl)-imide result in magnesium deposits containing high quantities of Mg–O and Mg–H impurities.[6] In this chapter, we place a further emphasis on the electrochemical kinetics for the Mg deposition-dissolution process along with a comparison of the resulting morphologies from three previously reported electrolyte solutions in THF: 1.2 M $((CF_3)_2CH_3)COMgCl$ and 0.2 M $AlCl_3$ (herein referred to as F_6-*t*-butoxide),[7] 0.5 M ^{R}PhOMgCl and 0.25 M $AlCl_3$ where R = 2,4,6-Me_3 (2,4,6-Me_3 phenolate),[8] and 0.4 M PhMgCl and 0.2 M $AlCl_3$ (APC).[9] Structures of the magnesium starting materials are illustrated in Figure 4.1 for reference.

4.2 Experimental

4.2.1 Synthesis of Electrolyte Solutions

All Grignard reagents were purchased from Sigma-Aldrich and used as received. 2,4,6-trimethylphenol and anhydrous $AlCl_3$ were purchased and used as received from Sigma-Aldrich and Alfa Aesar, respectively. Tetrahydrofuran was purchased from EMD anhydrous and further dried by refluxing under N_2 over the ketyl radical resulting from sodium and benzophenone. Once loaded into a N_2 glovebox (Vacuum Atmospheres), 3 Å molecular sieves were added to the

THF solvent. All electrolyte solutions in THF were prepared in agreement with initial reports for 1.2 M $((CF_3)_2CH_3)COMgCl$ and 0.2 M $AlCl_3$ in THF (F_6-*t*-butoxide),[7] 0.5 M ^{R}PhOMgCl and 0.25 M $AlCl_3$ where R = 2,4,6-Me_3 in THF (2,4,6-Me_3 phenolate),[8] and 0.4 M PhMgCl and 0.2 M $AlCl_3$ in THF (APC).[9]

4.2.2 Electrolyte Solution Characterization

Cyclic voltammetry (CV) and controlled potential coulometry experiments were recorded using a CH Instruments Electrochemical Workstation 660C while using a Pt-disk (CHI) working electrode and Mg-foil (MTI) counter and reference electrodes. CV measurements were performed in a custom designed, three-necked, sealed glass cell starting at open circuit potential and scanned toward more negative electrochemical potentials at 25 mV s^{-1}. Tafel plots were performed within the same cell using a Pt-disk working electrode starting at 0 V (vs $Mg^{2+/0}$) and scanned in the negative direction at a rate of 0.1 mV s^{-1} to a final potential of −1.3 V (vs $Mg^{2+/0}$) while vigorously stirring such that current is not limited by mass transport. Next, the working electrode was repoised at 0 V (vs $Mg^{2+/0}$) and scanned in the positive direction at 0.1 mV s^{-1} to a final potential of +2 V (vs $Mg^{2+/0}$). The resulting Tafel slopes for Mg deposition and stripping, respectively, were determined from the first linear region after the onset of current in the linear sweep voltammogram. Electrochemical impedance spectroscopy was carried out with an Eco Chemie Autolab PGSTAT128N potentiostat. Measurements were recorded at −1 V (vs $Mg^{2+/0}$) within the electrolyte solution of interest. Analysis was done with a 5 mV amplitude. The upper limit frequency was 1 MHz and the lower limit was chosen to be the lowest frequency obtainable without significant diffusional noise (1 Hz). Conductivity measurements were obtained using a Mettler-Toledo FEP30 conductivity meter equipped with an InLab 710 probe at room temperature.

Transference numbers (t_+) were estimated as described in a previous report.[10] In brief, chronopotentiometry was used to deposit Mg metal from 1 mL of electrolyte onto a Pt-disk working electrode, while metallic Mg strips were used as reference and counter electrodes. A controlled quantity of charge was passed between the electrodes, and the resulting deposits were then digested in 10 mL of a 0.1 M HNO_3 solution. This solution was analyzed with ICP-OES for Mg^{2+} using a PerkinElmer Optima 2000DV. Samples were referenced to an yttrium internal standard and concentrations of magnesium were determined from the maximum intensity compared to those of standard reference solutions.

Scanning electron microscopy (SEM) samples were prepared by chronopotentiometry with an applied current of −10 mA for 100 s (1 C) using a 0.25 cm^2 Cu-foil working electrode. Images were collected using a JEOL-7800FLV FE SEM instrument in the University of Michigan—Michigan Center for Materials Characterization with an accelerating voltage of 15 kV and a working distance of 10 mm. Profile X-ray diffraction patterns were recorded on a Cameca SX100 EPMA Rigaku Ultima IV diffractometer using Cu Kα radiation. Patterns were collected in θ–θ geometry with a sampling step of 0.05° and scan rate of 3° min^{-1}. In-plane pole figures were then recorded at each characteristic Mg diffraction peak observed within the profile X-ray diffraction pattern. Here, a continuous scan method was applied from 0 to 360° with a step size of 3° at 180° min^{-1}.

4.3 Results and Discussion

Three Mg^{2+}-containing electrolyte solutions were chosen to explore the kinetics of the deposition-dissolution process: our recently reported 1.2 M $((CF_3)_2CH_3)COMgCl$ and 0.2 M

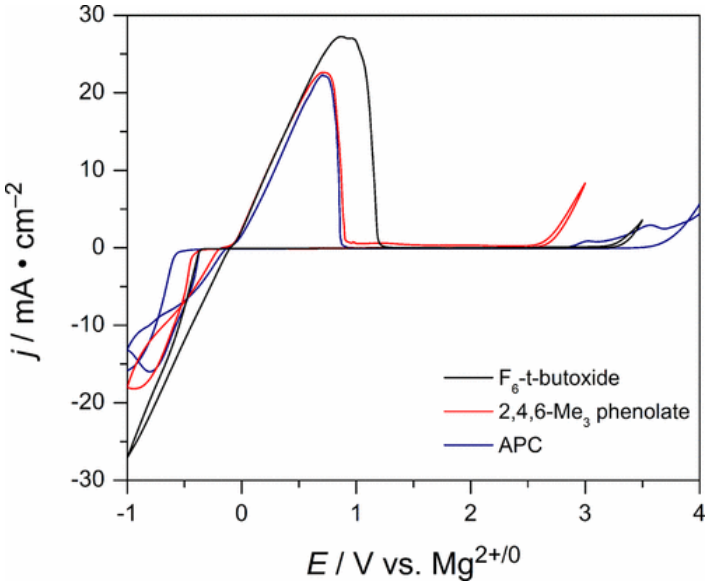

Figure 4.2. Cyclic voltammogram traces recorded using a Pt-disk working electrode of F_6-*t*-butoxide (black), 2,4,6-Me_3 phenolate (red), and APC (blue).

$AlCl_3$ in THF (F_6-*t*-butoxide) and 0.5 M ^{R}PhOMgCl and 0.25 M $AlCl_3$ where R = 2,4,6-Me_3 in THF (2,4,6-Me_3 phenolate), in addition to the longtime standard 0.4 M PhMgCl and 0.2 M $AlCl_3$ in THF (APC). Cyclic voltammetry, shown in Figure 4.2, was used to determine the current at which Mg deposition and stripping was carried out. Additionally, scanning the working electrode to potentials more positive than those required to reoxidize the previously deposited Mg^0 allows for assessment of the solution stability window. In agreement with the initial reports, the largest current density for Mg deposition results when the F_6-*t*-butoxide solution is employed (j_{max} = 27 mA cm^{-2}). Both the phenolate and APC electrolytes show similar current densities for the deposition-dissolution processes with a j_{max} ~ 20 mA cm^{-2}. Anodic stability increases when switching electrolytes in the order of phenolate, APC, and fluorinated alkoxide to a maximum of 3.2 V (vs $Mg^{2+/0}$) for the alkoxide solution.

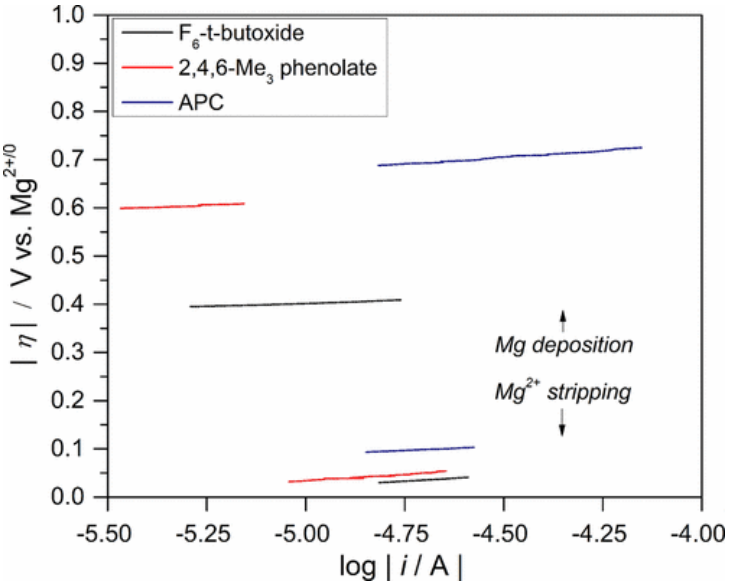

Figure 4.3. Tafel plot for Mg deposition and stripping from F_6-*t*-butoxide (black), 2,4,6-Me_3 phenolate (red), and APC (blue) electrolyte solutions in THF.

electrolyte	b_{dep}/mV dec^{-1}	η_{dep}/V vs Mg$^{2+/0}$	$j_{0,dep}$/mA cm^{-2}	b_{diss}/ mV dec^{-1}	η_{diss}/V vs Mg$^{2+/0}$	$j_{0,diss}$/mA cm^{-2}
F_6-*t*-butoxide	26.4	0.39	-1.94×10^{-16}	48.5	0.03	1.18×10^{-1}
2,4,6-Me_3 phenolate	32.1	0.60	-2.30×10^{-20}	53.3	0.03	7.36×10^{-2}
APC	56.2	0.69	-2.85×10^{-13}	35.6	0.09	1.10×10^{-3}
0.4 M F_6-*t*-butoxide	30.0	0.65	-5.14×10^{-23}	158	0.03	4.45×10^{-1}
0.1 M F_6-*t*-butoxide	40.5	0.97	-2.19×10^{-26}	425	0.04	1.98×10^{-1}

Table 4.1. Compilation of electrochemical values determined through Tafel analysis.

4.3.1 Tafel Analysis of Magnesium Deposition-Dissolution

In order to probe the electrochemical kinetics further, we carried out Tafel analysis of the *j*–*E* characteristics for both the magnesium deposition and dissolution processes. The deposition values were obtained using a Pt-disk electrode while scanning from 0 V (vs Mg$^{2+/0}$) toward negative potentials in order to reduce Mg-ions from the electrolyte, with the data presented in Figure 4.3. A compilation of the measured electrochemical values is represented in Table 4.1. More specifically, the smallest overpotential (η) is observed for F_6-*t*-butoxide (0.39 V vs Mg$^{2+/0}$). The overpotential for the 2,4,6-Me_3 phenolate and APC electrolytes are 0.60 and 0.69

V (vs $Mg^{2+/0}$), respectively. In addition to the smallest overpotential, the fluorinated alkoxide electrolyte also displayed the lowest Tafel slope of 26.4 mV dec^{-1}, followed by phenolate (32.1 mV dec^{-1}) and APC (56.2 mV dec^{-1}). In summary, the fluorinated alkoxide electrolyte shows the fastest electrochemical kinetics being both the magnitude of overpotential is smaller and that a smaller change in potential is required to increase the current density. Once a magnesium metal layer was deposited, the electrode was scanned toward positive potentials from 0 V (vs $Mg^{2+/0}$) to determine the kinetics of magnesium dissolution. Here, a much lower overpotential is detected across all solutions ($\eta < 100$ mV), with the smallest overpotential for F_6-*t*-butoxide and the 2,4,6-Me_3 phenolate electrolytes of $\eta = 30$ mV. However, Tafel slopes for the dissolution processes are more complicated, where APC shows the lowest slope at 35.6 mV dec^{-1}. While the electrochemical kinetics are fastest with this solution, it possesses the largest observed dissolution overpotential at 90 mV. However, the fluorinated alkoxide and 2,4,6-Me_3 phenolate show comparable Tafel slopes for Mg dissolution of 48.5 and 53.3 mV dec^{-1}, respectively. Overall, the Tafel analysis of the electrolyte solutions illustrate a larger range of overpotentials for Mg deposition (300 mV) compared to stripping (60 mV). We attribute this disparity in overpotentials to a difference in the active magnesium species responsible for deposition. Additionally, the magnitude of the overpotential for Mg deposition (>390 mV) is greater than Mg^{2+} stripping (<90 mV) across all solutions, likely due to the overpotential associated with magnesium deposition onto a platinum substrate.

4.3.2 Morphology and X-Ray Diffraction of Mg^0 Deposits

Since we observed different electrochemical kinetics, we surmised that the morphology of the resulting magnesium deposits from these selected electrolyte solutions may be different. The SEM images obtained after carrying out chronopotentiometry (10 mA, 100 s, 1 C charge

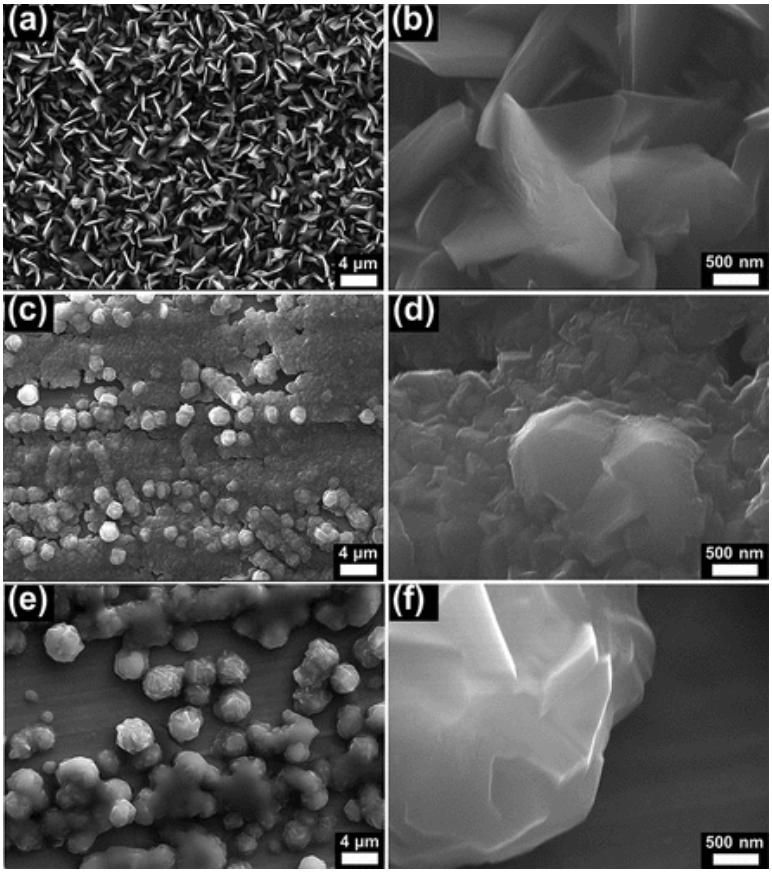

Figure 4.4. SEM images of Mg^0 deposits from F_6-*t*-butoxide (a and b), APC (c and d), and 2,4,6-Me_3 phenolate (e and f) solutions in THF.

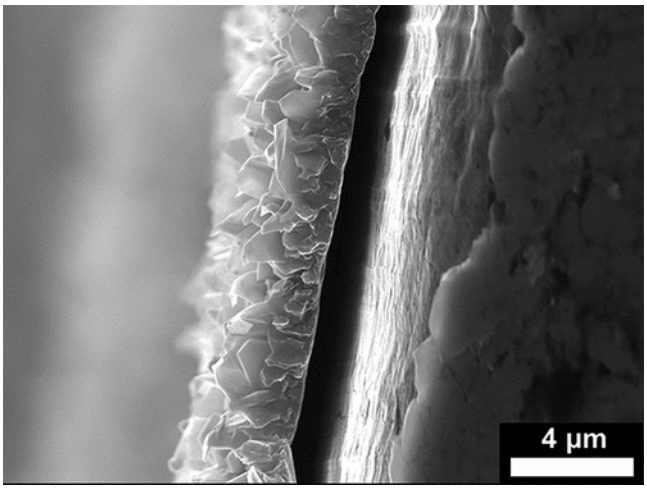

Figure 4.5. Cross-sectional SEM image of Mg^0 deposits from F_6-*t*-butoxide electrolyte in THF.

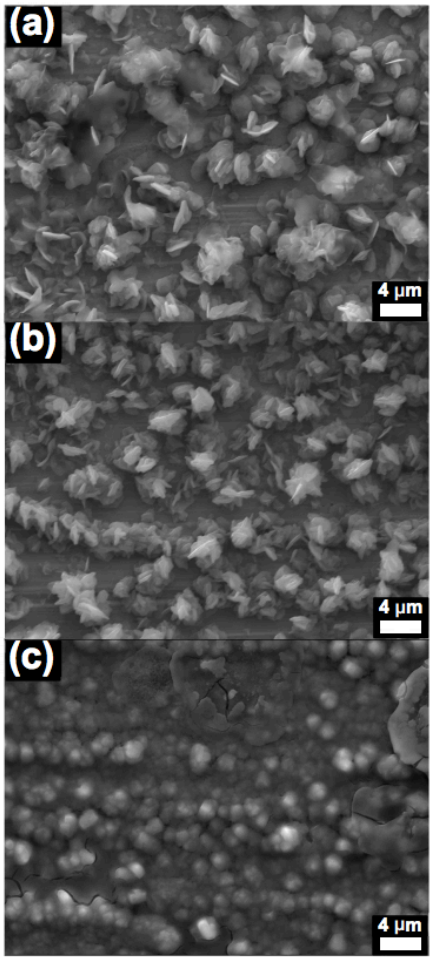

Figure 4.6. SEM images of Mg^0 deposits from (a) 0.5 M ^{R}PhOMgCl and 0.25 M $AlCl_3$ where R = 4-CF_3, (b) 0.5 M ^{R}PhOMgCl and 0.25 M $AlCl_3$ where R = 4-F, and (c) 0.4 M ^{R}PhMgCl and 0.2 M $AlCl_3$ where R = 4-F.

passed) are shown in Figure 4.4. We see a clear difference in both crystallinity and surface coverage between the fluorinated alkoxide and the two aromatic-based electrolytes. The F_6-*t*-butoxide solution gives rise to highly crystalline hexagonal platelets that are on average 3 µm in diameter and completely cover the working electrode. Additionally, the cross-sectional SEM image in Figure 4.5 further illustrates the dense and crystalline layer that forms on the electrode surface, with an overall thickness of approximately 3 µm. While similar-sized deposits are

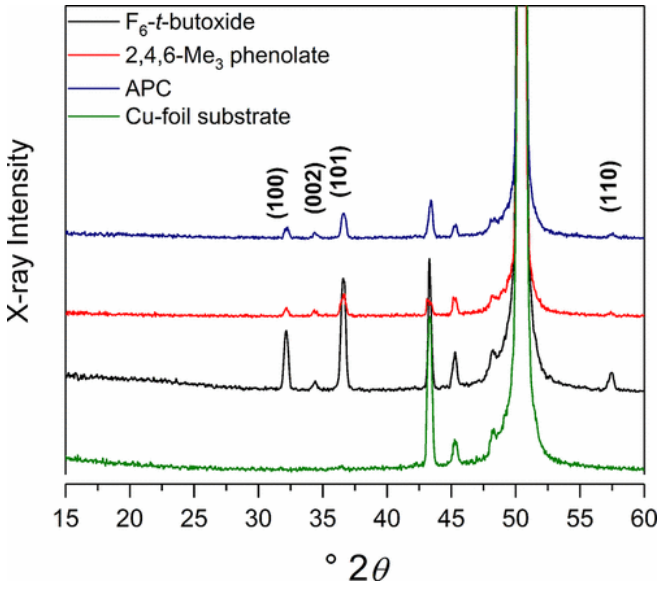

Figure 4.7. X-ray diffraction patterns of Mg deposits from F_6-*t*-butoxide (black), 2,4,6-Me_3 phenolate (red), and APC (blue). The Cu-foil substrate (green) is presented for reference.

observed when identical conditions are applied to the 2,4,6-Me_3 phenolate solution, the overall crystallinity decreases and the platelets agglomerate. The high degree of crystallinity and surface coverage observed from the fluorinated alkoxide solution is in stark contrast to the disperse 2 μm sized deposits obtained from the APC solution.

Since the electronics about the organic precursor differs greatly between the F_6-*t*-butoxide and aromatic-based electrolytes, we prepared THF solutions containing 0.5 M ^{R}PhOMgCl and 0.25 M $AlCl_3$ where R = 4-CF_3, 0.5 M ^{R}PhOMgCl and 0.25 M $AlCl_3$ where R = 4-F, and 0.40 M ^{R}PhMgCl and 0.20 M $AlCl_3$ where R = 4-F. From these solutions we examined the resulting Mg deposits after applying identical chronopotentiometric conditions as those above (Figure 4.6). The same general trend remains when comparing the deposits from nonfluorinated and fluorinated phenolate- and phenyl-based electrolyte solutions: phenolate-

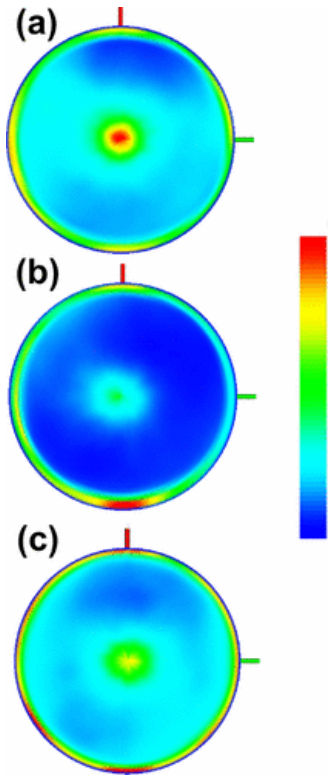

Figure 4.8. Pole figures about the (100) diffraction plane for Mg^0 deposits resulting from (a) F_6-*t*-butoxide, (b) APC, and (c) 2,4,6-Me_3 phenolate. The highest diffraction intensity is shown in red.

based solutions (whether R = 2,4,6-Me_3, 4-CF_3, or 4-F) show a slight increase in deposit crystallinity compared to phenyl-based solutions (where R = 4-H or 4-F), although the overall surface coverage is slightly improved when employing the phenyl-based electrolytes. However, adding electron-withdrawing substituents on any of the aromatic-based electrolyte solutions does not allow for the high crystallinity and surface coverage achieved from the F_6-*t*-butoxide solution.

The magnesium deposit crystallinity among the three solutions was further investigated using powder X-ray diffraction, illustrated in Figure 4.7. While the largest diffraction intensity

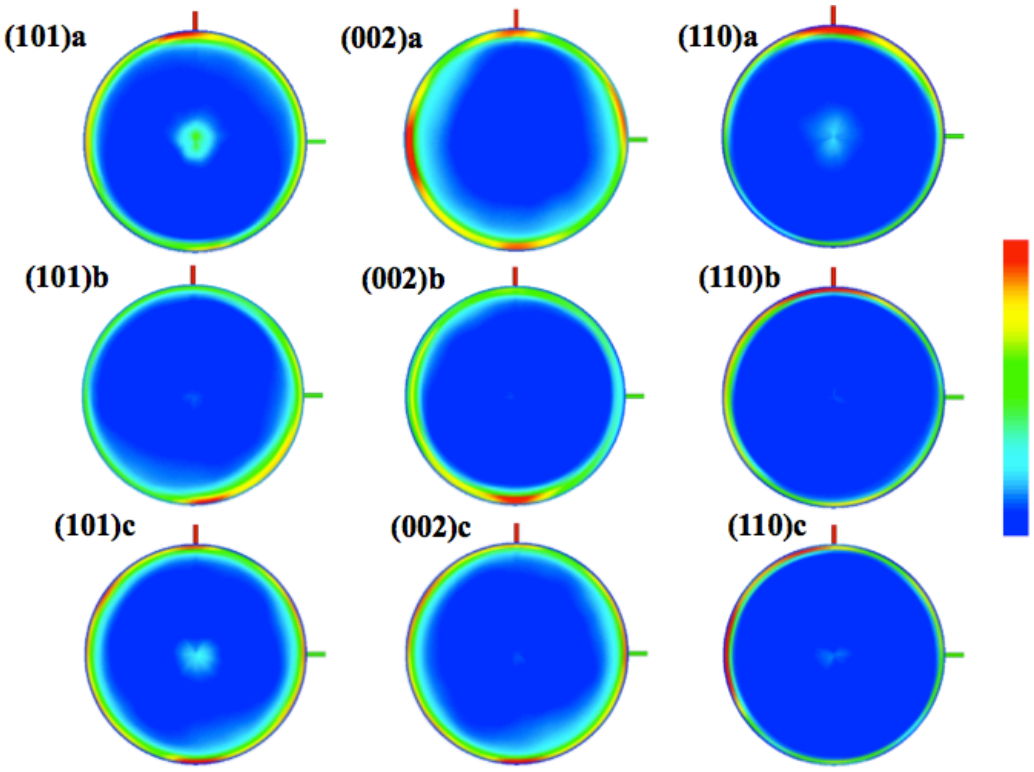

Figure 4.9. Pole figures collected about the (101), (002) and (110) for (a) F_6-*t*-butoxide, (b) APC, and (c) 2,4,6-Me_3 phenolate. The highest diffraction intensity is shown in red.

results from the Cu-foil sample substrate, four characteristic Bragg reflections of hcp magnesium deposits grow in between 15 and 60°2θ. The diffraction intensities are comparable between the deposits resulting from 2,4,6-Me_3 phenolate and APC solutions. However, when employing the F_6-*t*-butoxide solution, the intensity of Mg diffraction peaks increases 6-fold. In addition to the 2-D diffraction patterns (intensity vs °2θ), pole figure analysis was employed to probe preferred orientation of the deposits from the various electrolyte solutions. While pole figures have been previously used to characterize the deposits from magnesium-based chloride, sulfonylimide and tetraphenylaluminate electrolyte solutions, highly ordered Au (111) substrates were used, compared to the Cu electrodes with no distinct crystallographic texture employed in this study.[6] The pole figure collected while posing the diffractometer about the (100) diffraction

plane can be viewed within Figure 4.8. The highest diffraction intensity results at the center of the pole figure for the magnesium deposited from the F_6-*t*-butoxide electrolyte (Figure 4.8a), suggesting that the Mg grows along the [100] direction normal to the sample surface. Some preferred orientation is observed among deposits from the 2,4,6-Me_3 phenolate solution, although the highest intensity remains orthogonal to the sample surface (Figure 4.8c). Additionally, deposits generated from the APC solution shows the least amount of preferred orientation (Figure 4.8b). For completeness, the remaining three diffraction peaks observed in the diffraction pattern were examined while poising the diffractometer about their respective diffraction angles (Figure 4.9). Of the diffraction planes investigated, no preferred orientation normal to the sample surface was detected for the comparatively lower crystalline Mg deposits resulting from either 2,4,6-Me_3 phenolate or APC.

electrolyte	q/mAh	ΔC_{Mg}*/ppm	z_+	t_+
2,4,6-Me_3 phenolate	0.13	1.325	2	0.78
APC	0.13	3.160	2	0.46
F_6-*t*-butoxide	0.13	6.535	1	0.45

Table 4.2. Compilation of transference values

4.3.3 Estimation of Cationic Transference Numbers

Electrochemical experiments paired with X-ray adsorption spectroscopy,[10] subambient pressure ionization with nanoelectrospray mass spectrometry,[11] single-crystal X-ray diffraction,[12] and Raman spectroscopy[13] suggest the bimetallic complex $[Mg_2(\mu\text{-}Cl)_3(THF)_6]^+$ is the active cationic species formed in solution and the precursor for magnesium deposition. From here it is expected that dissociation of the dimer to a monometallic $[MgCl(THF)_5]^+$ complex that adsorbs onto the working electrode allows for a 2-electron transfer ($z_+ = 2$) to take place. On the contrary,

if electron transfer occurs directly from the bimetallic Mg complex, $z_+ = 1$ would be considered. Here, determining the transference number allows for the presumption of the charge on the final species prior to Mg-ion reduction and resulting deposition onto the working electrode surface. In our previous work, we determined the cationic transference number (t_+) of the 2,4,6-Me_3 phenolate solution to be 0.78 while assuming 2-electron transfer ($z_+ = 2$) (Table 4.2).[8] In this work, we have used ICP-OES analysis to calculate t_+ for APC to be 0.46, assuming $[MgCl(THF)_5]^+$ as the species responsible for magnesium deposition, according to the equation:

$$t_+ = 1 - (z_+ F \Delta C^* V/q)$$

where z_+ is the cation valency (=2), F is Faraday's constant 26.801 mAh mmol^{-1}, ΔC^* is the change in bulk magnesium ion concentration (1.30 mmol L^{-1}), V is the volume of electrolyte (10^{-3} L), and q is the charge passed (0.13 mAh). From Faraday's Law, the mass of magnesium liberated (m_{Mg}) at the electrode is (q/F) × (M/z) where M is the molar mass of the magnesium (24.305 g mol^{-1}). If a monovalent dimer is liberated, we expect 0.236 mg of magnesium to be liberated into a 10 mL solution (23.6 ppm). If a divalent monomer is liberated, we expect 0.0589 mg of magnesium to be liberated into a 10 mL solution (5.89 ppm). However, under identical conditions the Mg^{2+} content from the F_6-*t*-butoxide deposits (6.535 ppm) exceeded the maximum amount calculated from Faraday's law (5.89 ppm) while using $z_+ = 2$.[7] The mismatch between calculated and theoretical magnesium concentration suggests that the majority cationic charge carrier for the F_6-*t*-butoxide solution has a charge of $z_+ = 1$, with a calculated t_+ of 0.45. While both the 2,4,6-Me_3 phenolate and APC electrolytes deposit from a monomeric Mg species, the determined ionic species charge of 1 for the alkoxide-based solution implies that both adsorption and charge transfer take place in a single concerted step from the $[Mg_2(\mu\text{-}Cl)_3(THF)_6]^+$ dimeric complex.

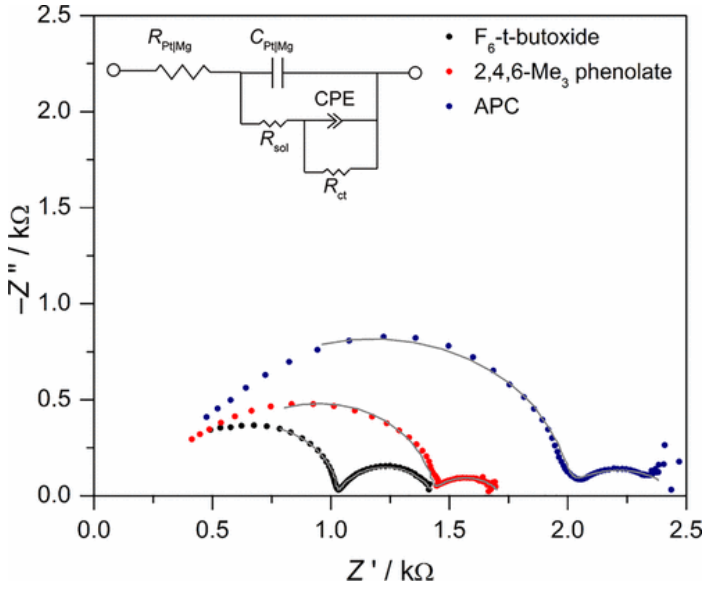

Figure 4.10. Nyquist plots of EIS results obtained using a Pt-disk working electrode of F_6-*t*-butoxide (black), 2,4,6-Me_3 phenolate (red), and APC (blue). The gray lines represent fits to the data using the model circuit illustrated in the inset.

electrolyte	R_{PtIMg}/Ω	R_{sol}/Ω	R_{ct}/Ω	$C_{PtIMg}/10^{-10}$ F	$CPE_{DL}/10^{-5}$ F
1.2 M F_6-*t*-butoxide	277.4 ± 6.6	748.3 ± 6.3	409.4 ± 2.2	3.872	0.8069
2,4,6-Me_3 phenolate	465.7 ± 8.8	960.4 ± 8.0	294.7 ± 8.6	5.947	1.490
APC	359.8 ± 8.6	1632 ± 8	468 ± 15	3.374	1.312
0.4 M F_6-*t*-butoxide	329.3 ± 8.2	825.4 ± 7.3	748 ± 13	5.446	2.667
0.1 M F_6-*t*-butoxide	631.5 ± 35.0	3354 ± 99	4785 ± 704	2.891	2.501

Table 4.3. Fits to the EIS model circuit while holding a Pt-disk working electrode at −1 V (vs $Mg^{2+/0}$).

4.3.4 Electrochemical Impedance Spectroscopy of Magnesium Electrodeposition

With distinct differences in deposition uniformity and solution electrochemical properties, we began investigating the charge transfer properties of these electrolyte solutions during the Mg deposition process. Electrochemical impedance spectroscopy was employed while poising a Pt-disk working electrode at −1 V vs $Mg^{2+/0}$. Figure 4.10 shows two distinct loops in the Nyquist plots, representing different charge transfer processes. Typically in impedance analysis, the high frequency intercept on the real axis (Z') corresponds to the solution resistance.

However, high frequency data (or shortest analysis time) also represents any impedance phenomena at or close to the electrode surface. Previous work carried out on decorated semiconductor[14,15] and polymer electrodes[16] have successfully distinguished the solution resistance from the impedance of their functionalized surfaces. In this study, the working electrode is poised at potentials more negative than the $Mg^{2+/0}$ equilibrium potential, therefore magnesium metal deposits onto the Pt working electrode at the start of the experiment. Consequently, we attribute the first semicircle to a combination of charge-transfer resistance at the Pt|Mg interface ($R_{Pt|Mg}$) and solution resistance (R_{sol}), using the model circuit in the inset of Figure 4.10. The lowest overall resistance for this first semicircle ($R_{Pt|Mg} + R_{sol}$) appears for the F_6-*t*-butoxide electrolyte (Table 4.3). These results are consistent with the alkoxide solution having both the highest solution conductivity and the most well-defined and compact deposition morphology (*vide supra*). Compared to the F_6-*t*-butoxide solution $R_{Pt|Mg}$ of 277 Ω, the resistance increases to 360 and 466 Ω for the APC and 2,4,6-Me_3phenolate electrolyte, respectively. While deposits resulting from the 2,4,6-Me_3 phenolate solution are slightly more crystalline, the overall film coverage is lower than that with APC, manifesting in the impedance analysis as a larger $R_{Pt|Mg}$. The correlation between observed Mg deposit coverage by SEM and $R_{Pt|Mg}$ values suggests that the interfacial impedance of bulk working electrodes are dominated by the surface coverage. However, when comparing the entire first charge-transfer loop, R_{sol} is a more prominent factor being that the combined resistance of the first semicircle for 2,4,6-Me_3 phenolate ($R_{Pt|Mg} + R_{sol}$ or 1426 Ω) is still lower than the R_{sol} of APC solution alone (1632 Ω). The high solution resistance of the APC electrolyte illustrates that solution conductivity is a key electrolyte design principle, as the determined R_{sol} values correlate well with the measured

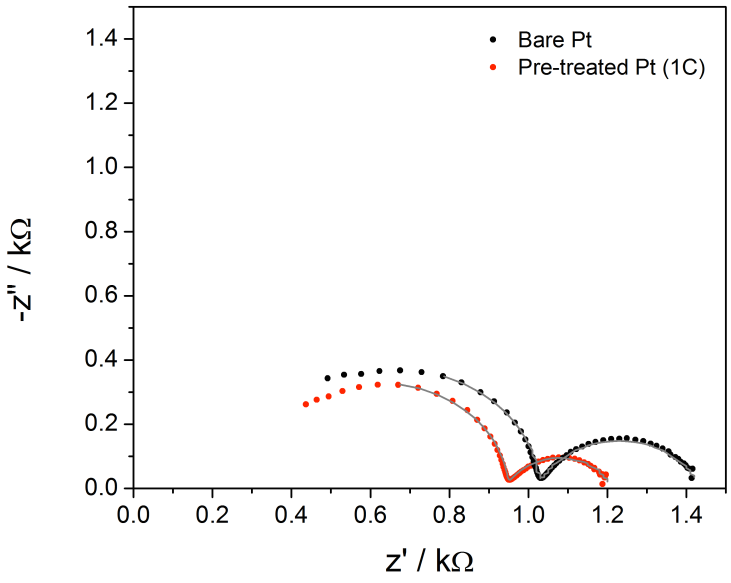

Figure 4.11. Nyquist plots of EIS results obtained using a bare Pt-disk (black) and a pre-treated Pt-disk electrode (red) of F_6-*t*-butoxide, including the fit (gray).

conductivity values: F_6-*t*-butoxide (3.5 mS cm^{-1}, 748 Ω), 2,4,6-Me_3 phenolate (2.6 mS cm^{-1}, 960 Ω), and APC (2.0 mS cm^{-1}, 1632 Ω).

The second semicircle is then assigned as charge transfer between the deposited Mg layer and solution (R_{ct}). Compared to the $R_{Pt|Mg}$ and R_{sol} values, the values for R_{ct} are more sporadic increasing in the order of 2,4,6-Me_3 phenolate, F_6-*t*-butoxide, and APC. It is remarkable that in these films the impedance due to the Pt|Mg interface and solution resistance is larger than the resistance to charge transfer. This disparity highlights the importance of high electrolyte conductivity and the formation of Mg deposits with low resistance as these phenomena dominate the impedance of the tested systems. $R_{Pt|Mg}$ is placed first, convoluting any additional circuit elements being that this resistance will be encountered regardless of the charge transfer event, followed by the accompanying capacitive portion ($C_{Pt|Mg}$) of this interface. Next is the solution

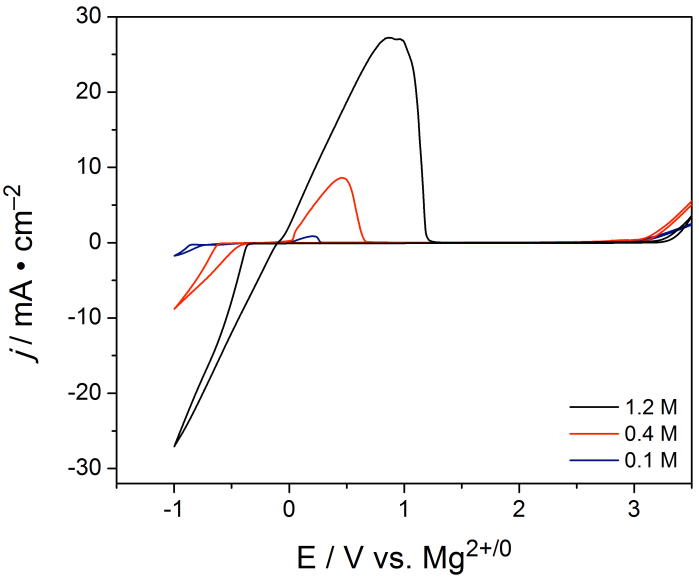

Figure 4.12. Cyclic voltammogram traces recorded using a Pt-disk working electrode of the diluted F_6-*t*-butoxide solutions, concentrations designated within the figure legend

resistance (R_{sol}), which trends with the solution conductivities as mentioned previously. Finally, charge transfer resistance (R_{ct}) is shown in parallel with a constant phase element (CPE) to represent electrochemical double layer charging. The constant phase element was chosen due to the depressed semicircular shape of the Nyquist plot, resulting from nonideal parallel plate capacitor behaviors due to the surface roughness of the Mg deposits across all solutions employed.[17,18]

To further illustrate the accuracy of the proposed circuit, we have performed a control experiment where a known quantity of Mg (0.13 mg based on 2-electron transfer from 1 C charge passed) was deposited onto the Pt-disk working electrode surface prior to any AC impedance analysis (Figure 4.11). As expected, the overall magnitude of the impedance response decreases with the pretreated electrode since it is kinetically easier to deposit Mg onto Mg rather

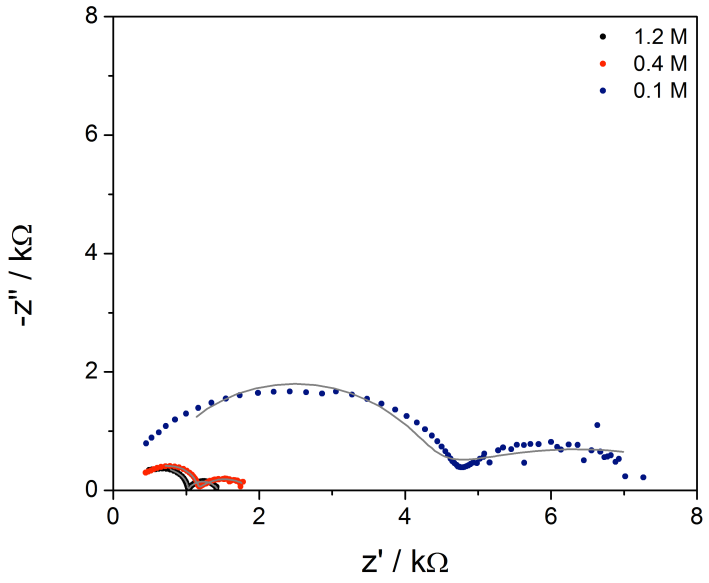

Figure 4.13. Nyquist plots of EIS results obtained using a Pt-disk working electrode of diluted F_6-*t*-butoxide electrolyte solutions, concentrations designated within the figure legend, including the fit (gray).

than onto Pt. Specifically, the combined $R_{Pt|Mg} + R_{sol}$ value decreases from 1026 to 947 Ω for the bare Pt and pretreated Pt, respectively.

4.3.5 Electrochemical Studies on Diluted F_6-*t*-Butoxide Electrolyte Solutions

Further support of the proposed circuit stems from performing similar analyses as those above on diluted solutions of the F_6-*t*-butoxide from the optimized value of 1.2 to 0.40 M $((CF_3)_2CH_3)COMgCl$ and 0.067 M $AlCl_3$ in THF and 0.1 M $((CF_3)_2CH_3)COMgCl$ and 0.017 M $AlCl_3$ in THF, maintaining a 6:1 alkoxide:$AlCl_3$ ratio. Prior to any EIS measurements, cyclic voltammetry was employed to ensure that at low concentrations, these solutions still have the ability to deposit and strip Mg-ions onto a Pt-disk working electrode (Figure 4.12). As the optimized solution is diluted, a decrease in solution conductivity (from 3.5 to 2.0 and 0.5 mS cm^{-1} for 1.2 to 0.4 and 0.1 M F_6-*t*-butoxide solutions, respectively) and kinetics of Mg

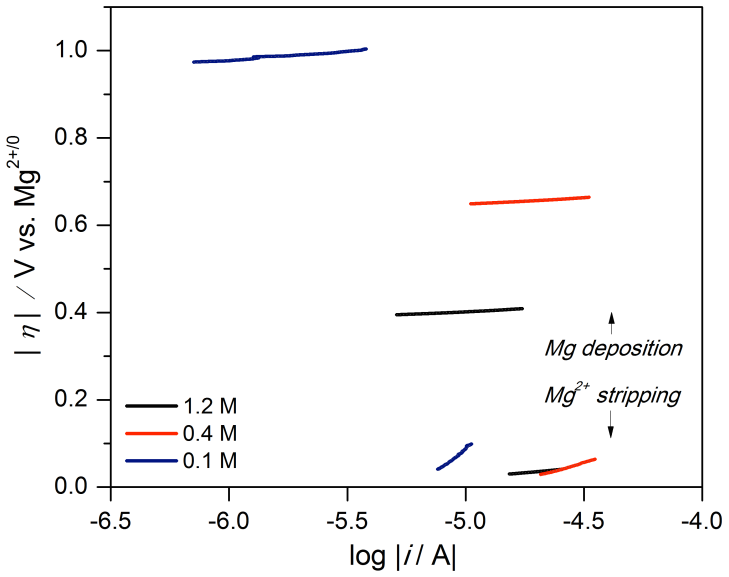

Figure 4.14. Tafel plot for Mg deposition and stripping from diluted F_6-*t*-butoxide solutions, concentrations designated within the figure legend.

deposition-dissolution is observed. Here, j_{max} of the cathodic peak <0 V (vs $Mg^{2+/0}$) decreases from 27 to 8.8 and 1.7 mA cm^{-2} for 1.2 to 0.4 and 0.1 M alkoxide solutions, respectively. The measured R_{sol} values of 409, 748, and 4785 Ω for the 1.2 to 0.4 and 0.1 M F_6-*t*-butoxide solutions, respectively, corroborate the conductivity and current density measurements. Additionally, the overall impedance for the plating of Mg increases as the electrolyte solution is diluted (Figure 4.13). While the $R_{Pt|Mg}$ does increase with electrolyte solution dilution, R_{ct} shows a more drastic increase. This observation is especially true for the 0.1 M F_6-*t*-butoxide solution, increasing from 409 to 4785 Ω (Table 4.3). Among the diluted samples $R_{Pt|Mg}$ is the most consistent value, suggesting that the dimeric coordination environment about the Mg^{2+}, rather than magnesium concentration, is strongly correlated with the metal–magnesium layer impedance.

Tafel analysis was performed identical to that shown above with the diluted F_6-*t*-butoxide solutions in THF (Figure 4.14). As shown in Table 4.1, while the Tafel slopes increase from the 1.2 M solution, they are all comparable to those of the other electrolyte solutions examined (2,4,6-Me_3 phenolate and APC). The overpotentials for magnesium deposition increase drastically, from 0.39 to 0.65 and 0.97 V (vs $Mg^{2+/0}$) for 1.2, 0.4, and 0.1 M solutions, respectively. While minimal differences exist between the diluted solutions when comparing the overpotential of magnesium reduction and subsequent adsorption, the Tafel slope for the dissolution process is greatly affected. Here, the lowest Tafel slope results with the most concentrated solution, 1.2 M (48.5 mV dec^{-1}), followed by 0.4 M (158 mV dec^{-1}) and 0.1 M (425 mV dec^{-1}). The drastic changes in the dissolution Tafel slope for the alkoxide solution postdilution corroborate the large resistances for charge transfer as we have determined through impedance.[19] The Tafel slopes at dilute concentrations suggest that with F_6-*t*-butoxide, electron transfer from the purported dimeric $[Mg_2(\mu\text{-}Cl)_3(THF)_6]^+$ complex is not as slow as the actual dissolution process.

4.4 Conclusions

Since the early demonstrations that Grignard solutions electrochemically deposit and strip Mg reversibly,[20,21] considerable advances have been made in developing Mg electrolytes. While comparing the deposition morphologies resulting from three proposed electrolyte solutions, the F_6-*t*-butoxide in THF solution prepared in our lab shows the most uniform and crystalline deposits growing along [100], normal to the electrode surface. The resulting deposits from 2,4,6-Me_3 phenolate and APC are less crystalline with sporadic growth. They also hinder the charge transfer properties at the electrode/electrolyte interface, since overcoming the resistance through

the Pt|Mg interface is necessary for overall Mg^{2+} reduction. Knowing the solution conductivity is shown to be an essential property for new electrolyte solutions as the combination of $R_{Pt|Mg}$ and R_{sol} accounts for the largest resistance during magnesium electrodeposition.

4.5 References

(1) Liebenow, C. Reversibility of electrochemical magnesium deposition from Grignard solutions *J. Appl. Electrochem.* **1997**, *27*, 221– 225.

(2) Matsui, M. Study on electrochemically deposited Mg metal *J. Power Sources* **2011***, 196,* 7048– 7055.

(3) Zhao-Karger, Z.; Zhao, X.; Fuhr, O.; Fichtner, M. Bisamide based non-nucleophilic electrolytes for rechargeable magnesium batteries *RSC Adv.* **2013**, *3*, 16330– 16335.

(4) Guo, Y.; Zhang, F.; Yang, J.; Wang, F. Electrochemical performance of novel electrolyte solutions based on organoboron magnesium salts *Electrochem. Commun.* **2012**, *18*, 24– 27.

(5) Nelson, E. G.; Kampf, J. W.; Bartlett, B. M. Enhanced oxidative stability of non-Grignard magnesium electrolytes through ligand modification *Chem. Commun.* **2014**, *50*, 5193– 5195.

(6) Bachhav, M. N.; Hahn, N. T.; Zavadil, K. R.; Nelson, E. G.; Crowe, A. J.; Bartlett, B. M.; Chu, P.; Araullo-Peters, V. J.; Marquis, E. A. Microstructure and chemistry of electrodeposited Mg films *J. Electrochem. Soc.* **2016**, *163*, D645– D650.

(7) Crowe, A. J.; Stringham, K. K.; Bartlett, B. M. Fluorinated alkoxide-based magnesium-ion battery electrolytes that demonstrate Li-ion-battery-like high anodic stability and solution conductivity *ACS Appl. Mater. Interfaces* **2016**, *8*, 23060– 23065.

(8) Crowe, A. J.; Bartlett, B. M. Influence of steric bulk on the oxidative stability of phenolate-based magnesium-ion battery electrolytes *J. Mater. Chem. A* **2016**, *4*, 368– 371.

(9) Aurbach, D.; Suresh, G. S.; Levi, E.; Mitelman, A.; Mizrahi, O.; Chusid, O.; Brunelli, M. Progress in rechargeable magnesium battery technology *Adv. Mater.* **2007**, *19*, 4260– 4267.

(10) Benmayza, A.; Ramanathan, M.; Arthur, T. S.; Matsui, M.; Mizuno, F.; Guo, J.; Glans, P. A.; Prakash, J. Effect of electrolytic properties of a magnesium organohaloaluminate electrolyte on magnesium deposition *J. Phys. Chem. C* **2013**, *117*, 26881– 26888.

(11) Liu, T.; Cox, J. T.; Hu, D.; Deng, X.; Hu, J.; Hu, M. Y.; Xiao, J.; Shao, Y.; Tang, K.; Liu, J. A fundamental study on the $[(\mu\text{-}Cl)_3Mg_2(THF)_6]^+$ dimer electrolytes for rechargeable Mg batteries *Chem. Commun.* **2015**, *51*, 2312– 2315.

(12) Kim, H. S.; Arthur, T. S.; Allred, G. D.; Zajicek, J.; Newman, J. G.; Rodnyansky, A. E.; Oliver, A. G.; Boggess, W. C.; Muldoon, J. Structure and compatibility of a magnesium electrolyte with a sulphur cathode *Nat. Commun.* **2011**, *2*, 427– 432.

(13) Pour, N.; Gofer, Y.; Major, D. T.; Aurbach, D. Structural analysis of electrolyte solutions for rechargeable Mg batteries by stereoscopic means and DFT calculations *J. Am. Chem. Soc.* **2011**, *133*, 6270– 6278.

(14) Klahr, B.; Gimenez, S.; Fabregat-Santiago, F.; Bisquert, J.; Hamann, T. W. Electrochemical and photoelectrochemical investigation of water oxidation with hematite electrodes *Energy Environ. Sci.* **2012**, *5*, 7626– 7636.

(15) Cueto-Gómez, L. F.; Garcia-Gómez, N. A.; Mosqueda, H. A.; Sánchez, E. M. Electrochemical study of TiO_2 modified with silver nanoparticles upon CO_2 reduction *J. Appl. Electrochem.* **2014**, *44*, 675– 682.

(16) Köleli, F.; Röpke, T.; Hamann, C. H. Electrochemical impedance spectroscopic investigation of CO_2 reduction on polyaniline in methanol *Electrochim. Acta* **2003**, *48*, 1595– 1601.

(17) Lvovich, V. F. Impedance spectroscopy applications to electrochemical and dielectric phenomena; John Wiley & Sons, Inc.: Hoboken, NJ, **2012**.

(18) Rammelt, U.; Reinhard, G. On the applicability of a constant phase element (CPE) to the estimation of roughness of solid metal electrodes *Electrochim. Acta* **1990**, *35*, 1045– 1049.

(19) Kear, G.; Walsh, F. C. The characteristics of a true Tafel slope *Corros. Mater.* **2005**, *30*, S1– S4.

(20) Connor, J. H.; Reid, W. E.; Wood, G. B. Electrodeposition of metals from organic solutions: electrodeposition of magnesium and magnesium alloys *J. Electrochem. Soc.* **1957**, *104*, 38– 41.

(21) Liebenow, C. Reversibility of electrochemical magnesium deposition from Grignard salt solutions *J. Appl. Electrochem.* **1997**, *27*, 221– 225.

Chapter 5

Adsorption of Aromatic Decomposition Products from Phenyl-Containing Magnesium-Ion Battery Electrolyte Solutions

Portions of this chapter have been published:

Crowe, A. J.; Stringham, K. K.; DiMeglio, J. L.; Bartlett, B. M. *J. Phys. Chem. C* **2017***, 121*(14), 7711–7717.

5.1 Introduction

The most extensively used electrolyte solution to date is the organohaloaluminate generated *in situ* from reacting 0.4 M PhMgCl with 0.2 M $AlCl_3$ in THF solvent.[1] The Lewis acid provides thermodynamic stability to 3.2 V (vs $Mg^{2+/0}$) while improving the kinetics of magnesium deposition and dissolution. However, the high chloride content in this electrolyte results in parasitic corrosion of stainless steel components commonly used as the battery can and current collector, thereby drastically hindering technology transfer from Li-ion predecessors.[2] In an effort to improve stainless steel compatibility, our group reported a solution with the ability to deposit/strip Mg after switching $AlCl_3$ with $Al(OPh)_3$. The optimized solution (0.5 M PhMgCl and 0.125 M $Al(OPh)_3$ in THF) offers *apparent* 5 V (vs $Mg^{2+/0}$) stability and demonstrates improved compatibility with stainless steel current collectors due to decreased chloride concentrations.[3] However, the electrochemical stability outside the typical region for the THF solvent (3–4 V vs $Mg^{2+/0}$) and the intermittent anodic signal spikes at higher applied potentials

suggest the presence of an electron-insulating layer forming on the electrode surface.[4] This chapter describes the nature of decomposition products in the PhMgCl–$Al(OPh)_3$ electrolyte system that adhere to a working electrode upon applying positive (oxidizing) potentials.

5.2 Experimental

5.2.1 Synthesis of Electrolyte Solutions

All Grignard reagents were purchased from Sigma-Aldrich and used as received. Anhydrous $MgCl_2$ and $AlCl_3$ were purchased and used as received from Amresco and Alfa Aesar, respectively. Tetrahydrofuran was purchased from EMD anhydrous and further dried by refluxing under N_2 over the ketyl radical resulting from sodium and benzophenone. Once loaded into a N_2 glovebox (Vacuum Atmospheres), 3 Å molecular sieves were added to the THF solvent. All electrolyte solutions in THF were prepared in agreement with initial reports for 0.4 M PhMgCl and 0.2 M $AlCl_3$ (PhMgCl–$AlCl_3$) in THF and 0.5 M PhMgCl and 0.125 M $Al(OPh)_3$ (PhMgCl–$Al(OPh)_3$) in THF.[1,3]

5.2.2 Electrolyte Solution Characterization

Cyclic voltammetry (CV) and controlled potential coulometry experiments were recorded using a CH Instruments Electrochemical Workstation 660C while using a Pt-disk (CHI) (or Pt-foil (Strem)) working electrode and Mg-foil (MTI) counter and reference electrodes. CV measurements were performed in a custom-designed, three-necked, sealed glass cell starting at open-circuit potential and scanned toward more negative electrochemical potentials at 25 mV s^{-1}. Conductivity measurements were obtained using a YSI model 3200 conductivity meter equipped with a 3253 conductivity cell at room temperature.

Gel permeation chromatography (GPC) samples were prepared via initial 4 V (vs $Mg^{2+/0}$) electrolysis for 3 h, unless noted otherwise, while employing a Pt-disk electrode in an Ar

glovebox (Vacuum Atmospheres). These electrolyzed Pt-disk electrodes were sonicated in 20 mL of THF for 2 h to give a clear colorless solution containing the adsorbed layer. The resulting solution was concentrated to a total volume of ~1 mL under a stream of nitrogen, followed by analysis using a photodiode array detector within a Shimadzu GPC System.

Scanning electron microscopy (SEM) samples were prepared via 4 V (vs $Mg^{2+/0}$) electrolysis of a 0.25 cm^2 Pt-foil working electrode for 3 h. Images were collected using an FEI Nova Nanolab 200 instrument in the University of Michigan–Michigan Center for Materials Characterization with an accelerating voltage of 10 kV, working distance of 5 mm, and beam current of 0.13 nA.

Raman spectroscopy samples were prepared with an initial 4 V (vs $Mg^{2+/0}$) electrolysis using a Pt-disk for 16 h. The electrodes were then removed from the Ar glovebox and placed directly within the spectrometer for analysis. Spectra were recorded using a Reinshaw inVia Raman microscope equipped with a 633 nm laser.

Nuclear magnetic resonance (NMR) samples were prepared via individual electrolysis (4 V vs Mg^{2+}) of 20 Pt-disk electrodes for 5 min, followed by sonication for 10 min in 5 mL of deuterated acetonitrile (Cambridge Isotope Laboratories). The solution volume was then decreased to ~1 mL with a stream of nitrogen. NMR spectra were recorded on a Varian VNMRS-700 MHz spectrometer in the University of Michigan Department of Chemistry NMR facility.

Electrochemical impedance spectroscopy was carried out with an Eco Chemie Autolab PGSTAT302N potentiostat with a frequency-response analysis (FRA) module. Measurements were recorded at 3.5 V (vs $Mg^{2+/0}$) within a 0.4 M PhMgCl and 0.2 M $AlCl_3$ in THF electrolyte. Analysis was done with a 5 mV amplitude perturbation after a 5 min equilibration time at each

potential. The upper limit frequency was 100 kHz, and the lower limit was chosen to be the lowest frequency obtainable without significant diffusional noise (0.01 Hz for Pt and 0.05 Hz for glassy carbon).

5.3 Results and Discussion

5.3.1 Electrochemical Analysis of PhMgCl Containing Solutions

To probe the electrochemistry and composition of the decomposition products formed upon cycling Mg-ion batteries, we examined both our recently reported 0.5 M PhMgCl and 0.125 M $Al(OPh)_3$ solution[3] and the traditional 0.4 M PhMgCl and 0.2 M $AlCl_3$ solution in THF. The CV traces of both electrolyte solutions recorded using a Pt-disk working electrode are shown in Figure 5.1. The current response of the 0.5 M PhMgCl and 0.125 M $Al(OPh)_3$ in THF solution depends on cycle number (Figure 5.1a). The initial cycle shows a broad anodic reaction occurring between 2 and 4 V (vs $Mg^{2+/0}$) that diminishes upon further cycling. The disappearance of this wide oxidation feature is accompanied by the appearance of irregular anodic spikes at potentials >2.5 V (vs $Mg^{2+/0}$). These intermittent anodic signals were observed in previous work and have been suggested to represent the break-and-repair of an electron-insulating layer on the electrode surface. Although the current densities for Mg deposition and dissolution decrease with successive cycling, the current is not completely diminished by the 10th cycle. This suggests that although the adsorbed layer may be electron insulating it remains semi-ion-permeable, which permits some Mg plating and stripping. Cycling a Pt-disk electrode between −1 and 1.5 V (vs $Mg^{2+/0}$) does not show diminishing current densities for Mg deposition stripping (Figure 5.2), suggesting that the electron-insulating layer forms at applied potentials >2 V (vs $Mg^{2+/0}$). To verify that the adsorbed layer is formed from an electrochemical process, we soaked a Pt-disk

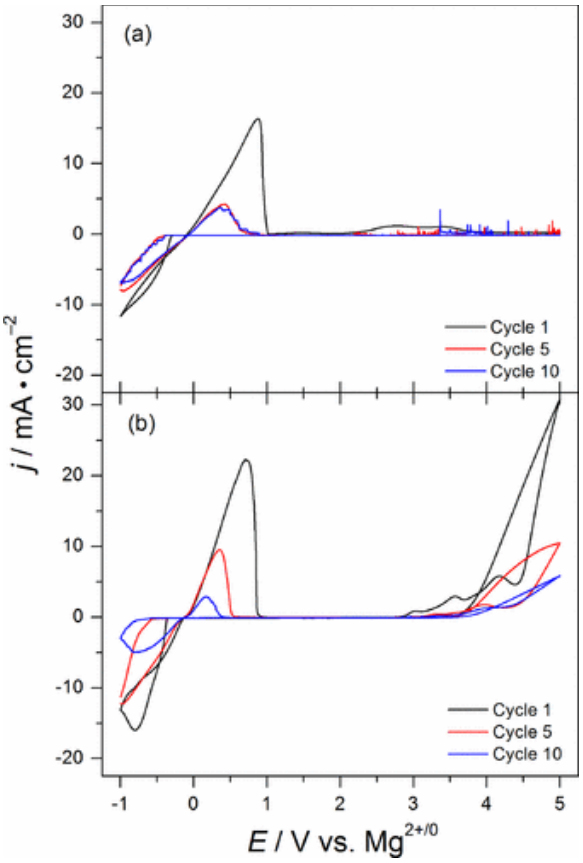

Figure 5.1. Cyclic voltammogram traces recorded using a Pt-disk working electrode of (a) 0.5 M PhMgCl and 0.125 M $Al(OPh)_3$ in THF and (b) 0.4 M PhMgCl and 0.2 M $AlCl_3$ in THF. Cycles 1 (black), 5 (red), and 10 (blue) are illustrated.

electrode in a solution of 0.5 M PhMgCl and 0.125 M $Al(OPh)_3$ in THF for 22 h at open circuit (under no applied potential). As shown in Figure 5.3, this pretreated electrode produces an identical anodic response between 2 and 4 V (vs $Mg^{2+/0}$) to a fresh Pt-disk, suggesting that the adsorbed layer is formed electrochemically, not chemically.

Subjected to equivalent electrochemical conditions, the traditional electrolyte, composed of 0.4 M PhMgCl and 0.2 M $AlCl_3$ in THF, demonstrates an anodic onset at ~3 V (vs $Mg^{2+/0}$) (Figure 5.1). Upon further cycling, this onset shifts to the reported anodic stability of 3.2 V (vs

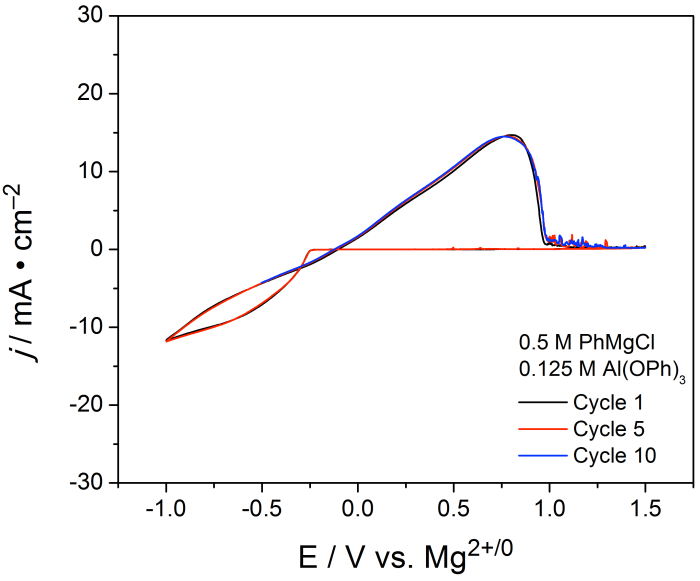

Figure 5.2. Cyclic voltammogram traces recorded using a Pt-disk cycled between –1 and 1.5 V (vs $Mg^{2+/0}$) of 0.5 M PhMgCl and 0.125 M $Al(OPh)_3$ in THF solution at cycle 1 (black) and 5 (red) and 10 (blue).

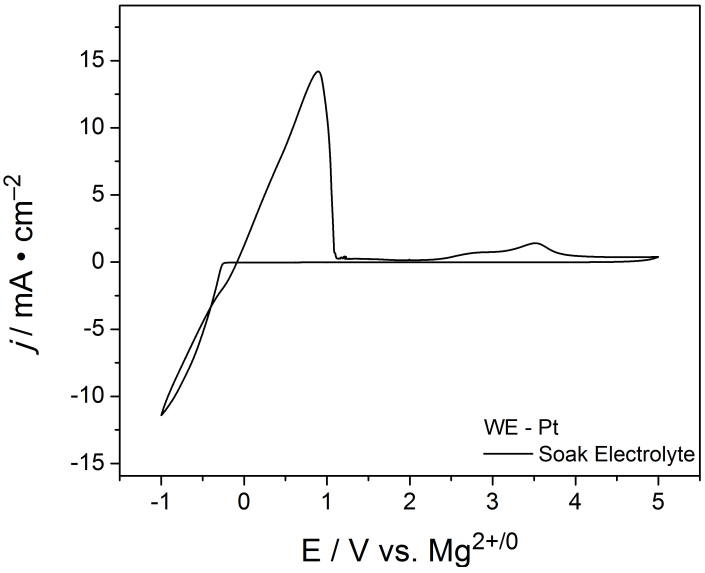

Figure 5.3. Cyclic voltammogram traces recorded using a Pt-disk of 0.5 M PhMgCl and 0.125 M $Al(OPh)_3$ in THF after soaking for 22 h in 0.5 M PhMgCl and 0.125 M $Al(OPh)_3$ in THF at open circuit.

$Mg^{2+/0}$).[5] While the slight expansion of the electrochemical window upon repeated cycling is observed with either Lewis acid, $AlCl_3$-stabilized solutions do not demonstrate electron insulation at applied potentials outside the expected stability region. Although the current density decrease for PhMgCl–$AlCl_3$ is similar for both deposition–dissolution at 0 V and for anodic processes >3 V (vs $Mg^{2+/0}$), we attribute this high potential anodic current to electrolyte decomposition. In fact, a black precipitate develops on the platinum at high applied bias using PhMgCl–$AlCl_3$, contrary to what we observe for PhMgCl–$Al(OPh)_3$.

In order to determine the role that the Lewis acid plays in electrolyte composition, a solution of 0.5 M PhMgCl and 0.25 M $MgCl_2$ in THF was examined electrochemically. The rate of Mg deposition–dissolution in PhMgCl–$MgCl_2$ electrolytes for cycle 1 is significantly decreased (Figure 5.4a) to j_{max} ~4 mA cm^{-2} compared to j_{max} ~15 mA cm^{-2} and ~20 mA cm^{-2} for PhMgCl–$Al(OPh)_3$ and PhMgCl–$AlCl_3$, respectively. This drop in deposition–dissolution current may be rationalized by the decreased conductivity of the electrolyte: 0.15 mS cm^{-1} for PhMgCl–$MgCl_2$ solutions compared to 1.2 mS cm^{-1} and 2.0 mS cm^{-1} for PhMgCl–$Al(OPh)_3$ and PhMgCl–$AlCl_3$ containing solutions, respectively.[3,4] Similar to PhMgCl–$Al(OPh)_3$, a broad anodic signal develops between 2 and 4 V (vs $Mg^{2+/0}$) within the first scan in PhMgCl–$MgCl_2$ solutions. After establishing that this anodic feature appears independent of having an aluminate anion present, a solution of 0.5 M PhMgCl without any additive in THF was prepared to determine the current response of unstabilized Grignard reagent in the same potential window. As Figure 5.4b demonstrates, similar electrochemical behavior is shown between PhMgCl, PhMgCl–$Al(OPh)_3$, and PhMgCl–$MgCl_2$ containing solutions. Additionally, we note that the anodic response occurring between 2 and 4 V (vs $Mg^{2+/0}$) reaches a consistent maximum current

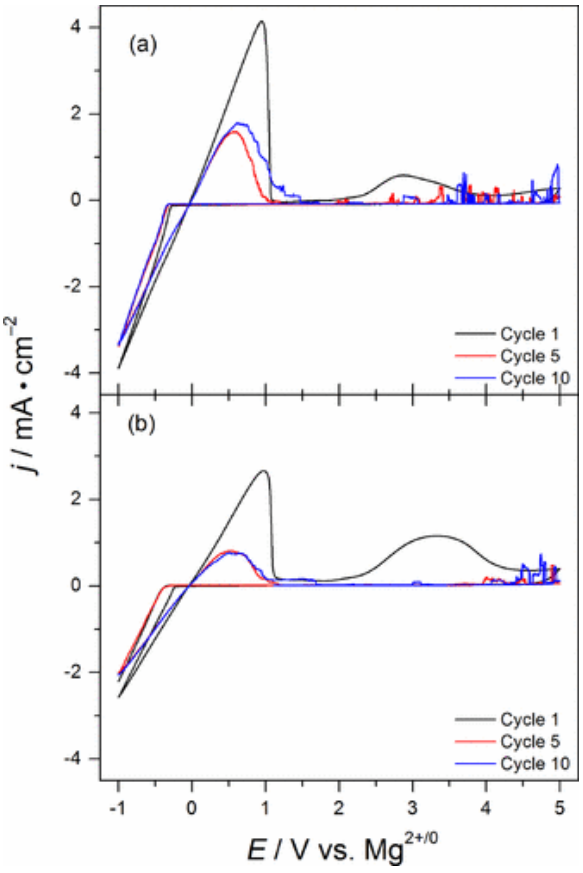

Figure 5.4. Cyclic voltammogram traces recorded using a Pt-disk working electrode of (a) 0.5 M PhMgCl and 0.25 M $MgCl_2$ in THF and (b) 0.5 M PhMgCl in THF. Cycles 1 (black), 5 (red), and 10 (blue) are illustrated.

density of ~1 mA cm^{-2} across all solutions that show passivated electrode surfaces. The major difference among these solutions is the observed current density for Mg deposition/dissolution, which trends with solution conductivity (*vide supra*). The consistent appearance and current density of the signal occurring between 2 and 4 V (vs $Mg^{2+/0}$) followed by its disappearance in subsequent sweeps for solutions containing PhMgCl, PhMgCl–$Al(OPh)_3$, and PhMgCl–$MgCl_2$ suggests the presence of an adsorbed decomposition product that prevents further electrochemical cycling once formed.

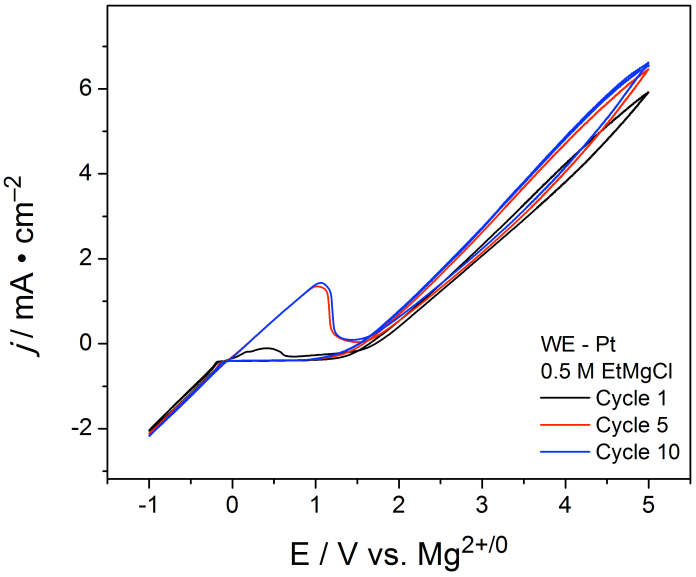

Figure 5.5. Cyclic voltammogram traces recorded using a Pt-disk working electrode of 0.5 M EtMgCl in THF solution at cycle 1 (black) and 5 (red) and 10 (blue).

5.3.2 Chemical Identity of Adsorbed Decomposition Products

A common chemical moiety to each passivating electrolyte is the phenyl group from the Grignard. We hypothesize that this phenyl group reacts to form the insulating layer. To show that this hypothesis is reasonable, we carried out a control experiment: a 0.5 M EtMgCl solution in THF (no phenyl) shows no decrease in the rate of solution oxidation with subsequent cycles (Figure 5.5). We attribute the current density *increase* for deposition–dissolution between the first and resulting cycles to electrolytic conditioning, similar to what has been described previously with other EtMgCl-containing solutions.[6]

Previous studies featuring ^{27}Al NMR spectroscopy show that PhMgCl–$AlCl_3$ electrolyte solutions develop a complex equilibrium of aluminates—existing as $[Ph_4Al]^-$, $[Ph_3AlCl]^-$, $[Ph_2AlCl_2]^-$, and $[Al_2Cl_6]$, where the thermodynamic stability depends on the degree of substitution. In contrast to observing multiple species under standard conditions with PhMgCl–

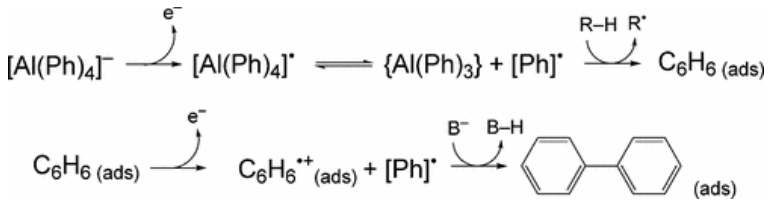

Figure 5.6. Possible degradative pathway resulting in the adsorption of aromatic species.

$AlCl_3$, only $[Ph_4Al]^-$, the least oxidatively stable species, is observed in PhMgCl–$Al(OPh)_3$ solutions.[3,4] The anion is the most oxidizable species in solution, and the HOMO of $[Ph_4Al]^-$ is composed of the π aromatic phenyl ligand. Electron flow from solution into the working electrode registers an anodic current and likely generates an aromatic-centered radical near the electrode surface (Figure 5.6, top). From here, ligand dissociation, driven by the regeneration of aromaticity within the oxidized phenyl substituent, provides an $\{Al(Ph_3)\}$ Lewis acid fragment and Ph-radical ($Ph^•$). H atom transfer, likely from the THF solvent, to $Ph^•$ allows for the adsorption of benzene to the electrode surface. Additionally, preadsorbed species can further react to generate higher molar mass compounds. Here, the adsorbed species is oxidized to generate an aromatic radical cation (Brønsted acid) that after deprotonation can further react with $Ph^•$ to yield biphenyl (Figure 5.6, bottom). We suspect that highly substituted adsorbed aromatics may be generated through the subsequent oxidation and deprotonation of biphenyl as well as the resulting higher molar mass adsorbed species. While Figure 5.6 (top) outlines the proposed pathway for solutions containing $Al(Ph)_4^-$, we surmise Ph^- to be the major aromatic species in aluminate-free solutions. Adsorption of benzene is accomplished with a Brønsted acid–base reaction to protonate Ph^-, which can be further substituted as outlined in Figure 5.6 (bottom). Electrooxidation of Ph^- to $Ph^•$, followed by H atom transfer, would also allow for benzene adsorption.

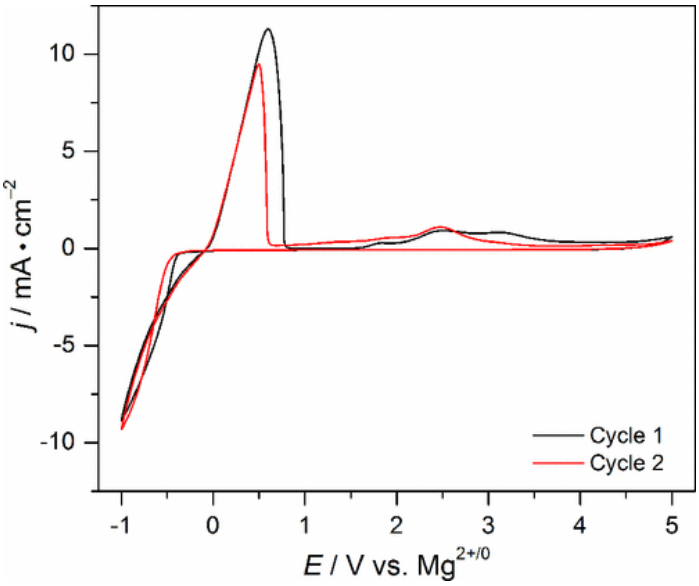

Figure 5.7. Cyclic voltammogram traces recorded using a Pt-disk working electrode of PhMgCl–$AlCl_3$ with the addition of PhLi at cycles 1 (black) and 2 (red).

We anticipate this cascade of reactions is continuous until the electrode is completely covered. With the decomposition of a Ph-substituent serving as the likely candidate for electrode adsorption, a solution combining the optimized PhMgCl–$AlCl_3$ solution (1 mL) with 1 mmol PhLi (1.8 M in dibutyl ether) was prepared. As shown by the large current density for Mg deposition/stripping in Figure 5.7, the solution containing excess Ph^- is still electrochemically active with a Pt-working electrode, suggesting that the purported active magnesium species[7] $[Mg_2(\mu\text{-}Cl)_3(THF)_6]^+$ is still present. From the first to second CV scan, the current density for Mg deposition/stripping is reduced, similar to what is observed for PhMgCl, PhMgCl–$Al(OPh)_3$, and PhMgCl–$MgCl_2$ containing solutions. At potentials outside the expected stability of PhMgCl–$AlCl_3$ (>3.2 vs $Mg^{2+/0}$), no anodic current indicative of electrolyte decomposition is observed. Being that the broad anodic wave between 2 and 4 V (vs $Mg^{2+/0}$)

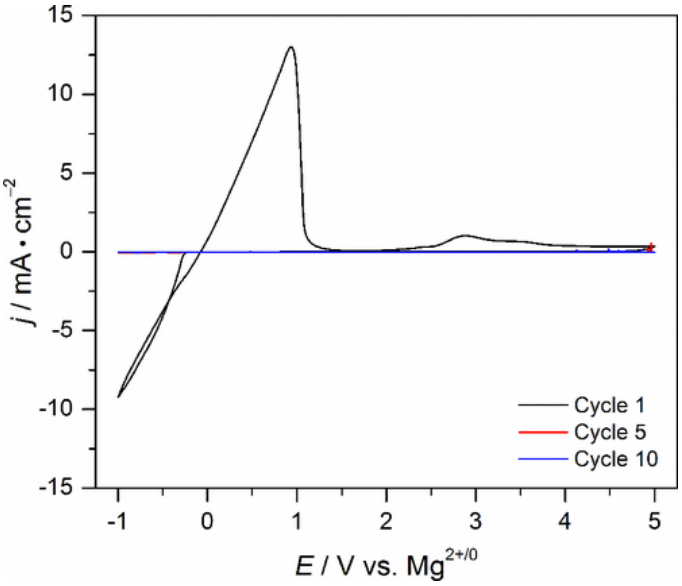

Figure 5.8. Cyclic voltammogram traces recorded using a glassy carbon disk working electrode of 0.5 M PhMgCl and 0.125 M $Al(OPh)_3$ in THF. Cycles 1 (black), 5 (red), and 10 (blue) are illustrated.

remains intact after the initial cycle, we surmise that the observed suppression of Mg deposition–dissolution is the result of the combined solution containing a significantly higher concentration of Ph^- near the electrode surface instead relying upon anodic decomposition.

We also investigated the passivation phenomena on non-noble metal working electrodes (Al, Cu, stainless steel, and glassy carbon). Due to the corrosive nature of electrolyte solutions in this investigation, we observed erratic anodic signals for Al, Cu, and stainless steel foil electrodes. This corrosion is corroborated by the visual degradation of the working electrode after electrolysis. Unlike metallic electrodes, glassy carbon disk electrodes show electrochemical stability for all electrolyte solutions examined (Figure 5.8). During the initial scans employing a glassy carbon electrode, the typical broad anodic onset remains between 2 and 4 V (vs $Mg^{2+/0}$). Additional scans show no current after the first, suggesting that a passivating layer covers the

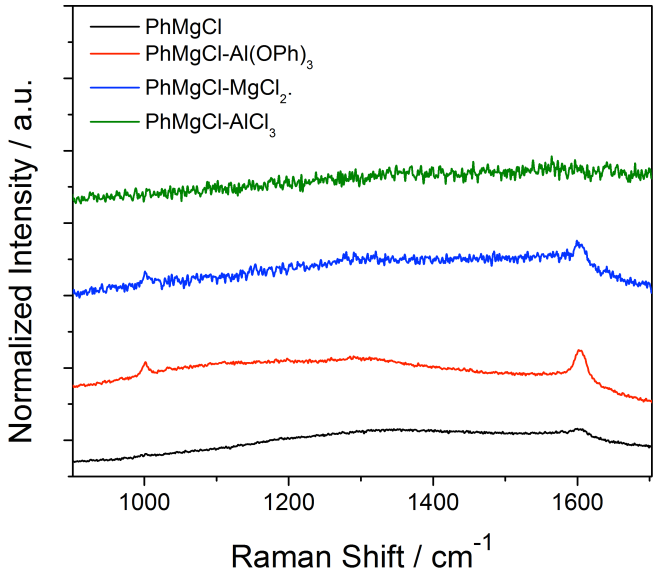

Figure 5.9. Raman spectroscopy of Pt-disk electrodes post 4 V (vs $Mg^{2+/0}$) for 16 hours within 0.5 M PhMgCl (black), 0.5 M PhMgCl and 0.125 M $Al(OPh)_3$ (red), 0.5 M PhMgCl and 0.25 M $MgCl_2$ (blue), and 0.4 M PhMgCl and 0.2 M $AlCl_3$ (green) in THF solutions.

carbon electrode completely. This conclusion is also consistent with the need for increased mechanical polishing of carbon over Pt-based electrodes between electrochemical experiments.

Chemical investigation of the electrode surface after 4 V (vs $Mg^{2+/0}$) electrolysis of PhMgCl, PhMgCl–$Al(OPh)_3$, and PhMgCl–$MgCl_2$ solutions shows two distinct Raman signals at 1600 and 1000 cm^{-1} (Figure 5.9). Theses vibrations are typical of aromatic ring vibrations and are absent when PhMgCl–$AlCl_3$ is electrolyzed. Additionally, upon dissolving the adsorbed species formed on platinum from electrolyzing a THF solution of 0.5 M PhMgCl and 0.125 M $Al(OPh)_3$ in acetonitrile-d_3 to carry out ^1H NMR spectroscopy (Figure 5.10), several peaks within the aromatic region (7–8 ppm) appear. Not only does this result suggest the aromatic nature of adsorbed species, but also the appearance of several multiplets in the aromatic region offers the possibility of a further substituted phenyl species rather than a single benzene unit.

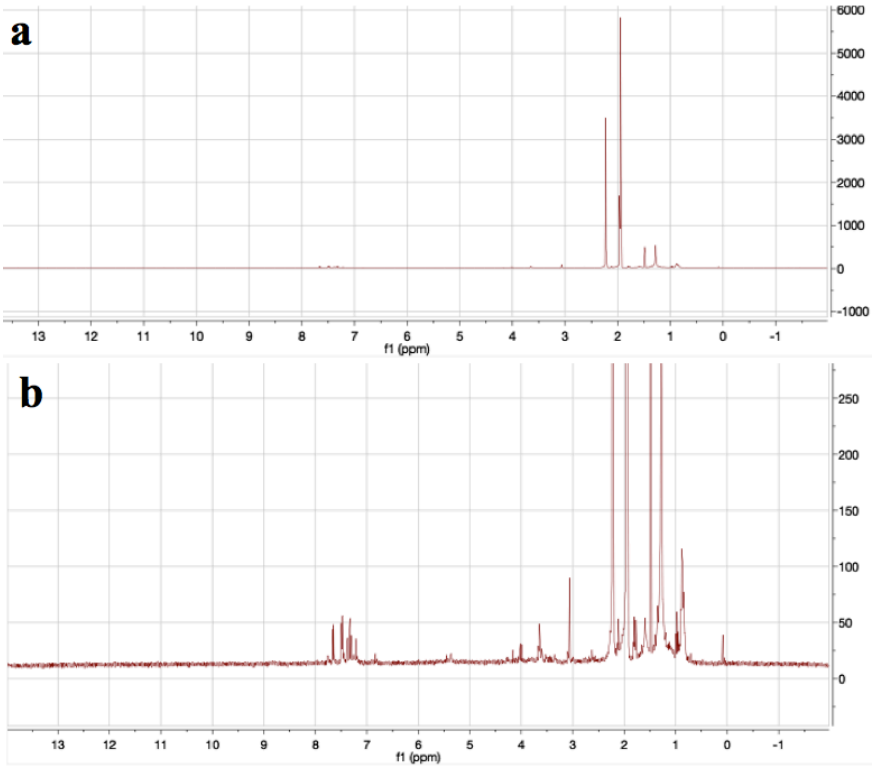

Figure 5.10. ^{1}H NMR spectrum from the dissolved electrode decomposition products on Pt-disk electrodes. (a) Full spectrum, (b) increased baseline to show low concentration aromatic product.

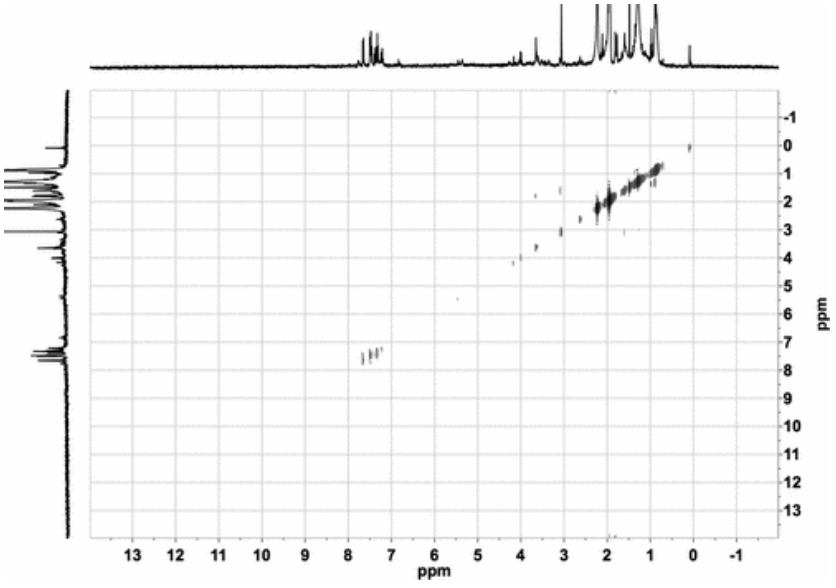

Figure 5.11. ^{1}H–^{1}H COSY NMR spectrum from the dissolved electrode decomposition products on Pt-disk electrodes.

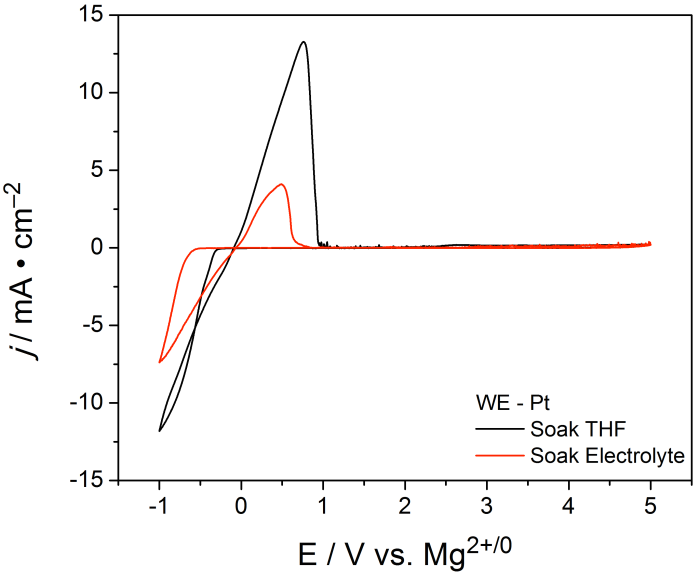

Figure 5.12. Cyclic voltammogram traces using a passivated Pt-disk, generated from a 4 V (vs $Mg^{2+/0}$) electrolysis for 5 minutes, after soaking 72 hours in 0.5 M PhMgCl and 0.125 M $Al(OPh)_3$ (red) and in neat THF (black).

Due to the difficulties of sample preparation, low signal (corresponding to coupled aromatics rather than baseline noise) of the decomposition product is observed. As a result, ^1H–^1H COSY NMR spectroscopy was employed to ensure no spin–spin coupling between those in the aromatic region and those arising from signals more upfield. As shown in Figure 5.11, only correlation between the aromatic regions exists, suggesting direct phenyl linkages of further substituted adsorbates.

In order to determine the stability of the adsorbed aromatic film, prepassivated Pt-disk electrodes, generated from an initial 4 V vs $Mg^{2+/0}$ electrolysis for 5 min, were immersed in either 1 mL of neat THF or a fresh solution of PhMgCl–$Al(OPh)_3$ in THF for 72 h. CV traces of the treated electrodes (Figure 5.12) show no response at potentials >1 V (vs $Mg^{2+/0}$) other than those resulting from the temporary break in the adsorbed layer. The electrode soaked in

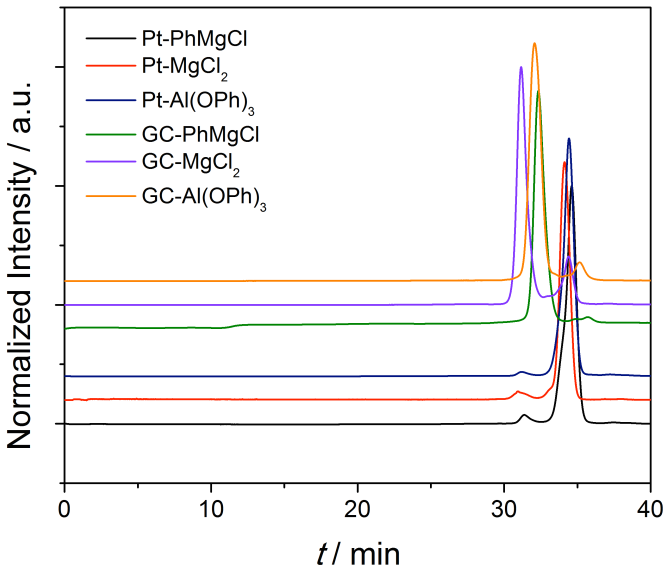

Figure 5.13. GPC traces of dissolved electrolysis products resulting from PhMgCl containing electrolyte solutions on Pt-disk electrodes (black, red, and navy) and glassy carbon disk electrodes (green, violet, orange) post 3 hour electrolysis.

PhMgCl–$Al(OPh)_3$ electrolyte shows decreased activity for $Mg^{2+/0}$ deposition/stripping, consistent with a passivated working electrode (Figure 5.1a, Cycle 5). In contrast, the electrode soaked in neat THF shows a current response for Mg deposition–stripping consistent with Cycle 1 of Figure 5.1a after being reimmersed in a fresh THF solution of PhMgCl–$Al(OPh)_3$ electrolyte. This result suggests slight desorption of the passivating layer results after long-term soaking. Since we do not observe an anodic wave between 2 and 4 V (vs $Mg^{2+/0}$) after soaking in either solutions, we conclude that the adsorbed layer is robust within typical battery cycling conditions.

To determine the chemical composition of the aromatic species formed on electrode surfaces, we estimated molar masses with gel permeation chromatography (GPC). In short, an extended electrolysis (4 V vs $Mg^{2+/0}$ for 3 h) was carried out on the various PhMgCl-containing

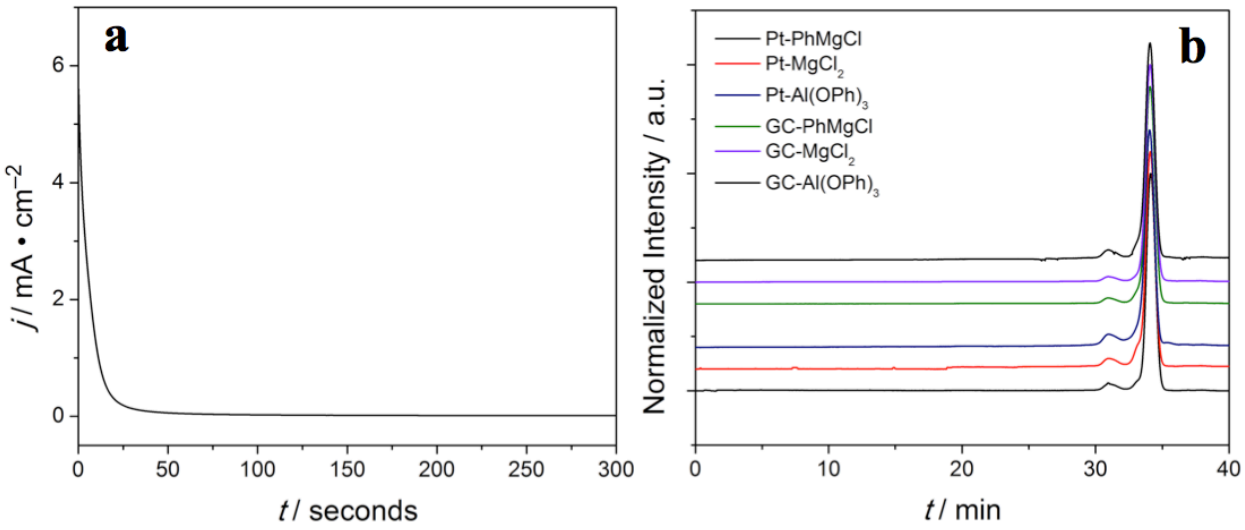

Figure 5.14. (a) Electrolysis profile of a 5 minute, 4 V (vs $Mg^{2+/0}$), electrolysis and (b) GPC traces of dissolved electrolysis products resulting from PhMgCl containing electrolyte solutions on Pt-disk electrodes (black, red, and navy) and glassy carbon disk electrodes (green, violet, orange) post 5 minute electrolysis.

solutions, followed by sonicating the working electrode in fresh THF solvent to remove the dissolved species. Figure 5.13 shows a drastic difference in the molar masses of the adsorbed species on platinum versus glassy carbon disk electrodes. Platinum electrodes predominantly generate species of lower molar masses (50–300 g mol^{-1} at ~35 min retention time), with minimal higher molar mass products (200–800 g mol^{-1} at ~30 min retention time). Conversely, glassy carbon electrodes largely produce species of higher molar mass. We do not observe molar masses lower than that of benzene (78 g mol^{-1}), due to either poor elution or a lack of those species being formed. To determine if extended electrolysis contributes to the molar mass of adsorbed species, the GPC experiment was repeated after just 5 min of constant potential coulometry, rather than 3 h. From the *j*–*t* electrolysis profile (Figure 5.14, left), significant current decay occurs after 20 s of applying 4 V vs $Mg^{2+/0}$ while employing a Pt-disk electrode, suggesting that most of the charge responsible for adsorbate formation is passed over this time.

GPC traces of the adsorbates formed on Pt-based electrodes after 5 min of electrolysis are consistent with the extended electrolysis results with primary species of ~50–300 g mol^{-1} (Figure 5.14, right). However, shorter electrolysis on carbon-based electrodes show lower molar mass compounds as the predominate species as well. This observation suggests further reaction of these lower molar mass adsorbates is possible with extended electrolysis.

5.3.3 Charge-Transfer Properties of Adsorbed Species on Working Electrode Surfaces

In order to determine the charge-transfer properties of the electrochemically formed passivating films, we employed electrochemical impedance spectroscopy (EIS). All three electrolyte solutions that show electron-insulating behavior were investigated (PhMgCl, PhMgCl–$Al(OPh)_3$, and PhMgCl–$MgCl_2$) in comparison to a clean Pt-disk electrode. A passivating film was generated on a Pt-disk electrode by constant potential coulometry at 4 V (vs $Mg^{2+/0}$) for 1 h. We then washed the electrode with THF and immersed it in a separate THF solution of 0.4 M PhMgCl and 0.2 M $AlCl_3$. PhMgCl−$AlCl_3$ was employed for two reasons: (1) this electrolyte does not generate any insulating decomposition products that would alter the impedance response and (2) the solution will provide a charge-transfer event, corresponding to electrolyte oxidation, at electrochemical potentials outside the stability window (>3.2 V vs $Mg^{2+/0}$). As a result, all solutions were examined with an alternating voltage signal about 3.5 V (vs $Mg^{2+/0}$).

Initial experiments show a depressed semicircle response for all electrodes that were electrochemically treated prior to impedance analysis (Figure 5.15)), suggesting porosity within the electrode surface.[8] Additionally, positive imaginary components (Z'') at low frequencies were observed for all electrodes that were subjected to initial electrolysis. Similar examples are

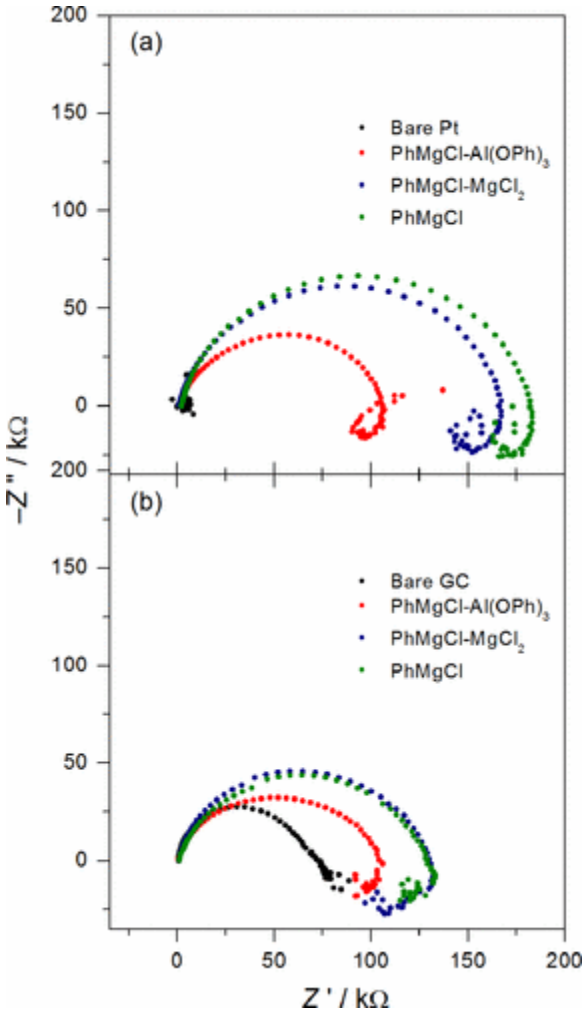

Figure 5.15. AC impedance spectroscopy results obtained using a (a) Pt-disk electrode and (b) glassy carbon-disk electrode in THF solutions of 0.4 M PhMgCl and 0.2 M $AlCl_3$ poised at 3.5 V (vs $Mg^{2+/0}$). Data from a pristine electrode are shown in black. Other electrodes were pre-electrolyzed in solutions of 0.5 M PhMgCl and 0.125 M $Al(OPh)_3$ (red), 0.5 M PhMgCl and 0.25 M $MgCl_2$ (blue), and 0.5 M PhMgCl (green).

reported within the corrosion literature[9] and in systems where electrode adsorption is possible.[10,11] Given that corrosion is unlikely for a Pt-disk working electrode, we attribute this positive Z'' component to the formation of an adsorbate. Although PhMgCl–$AlCl_3$ still shows minor decomposition, even on preadsorbed electrode surfaces, the electrode surface is

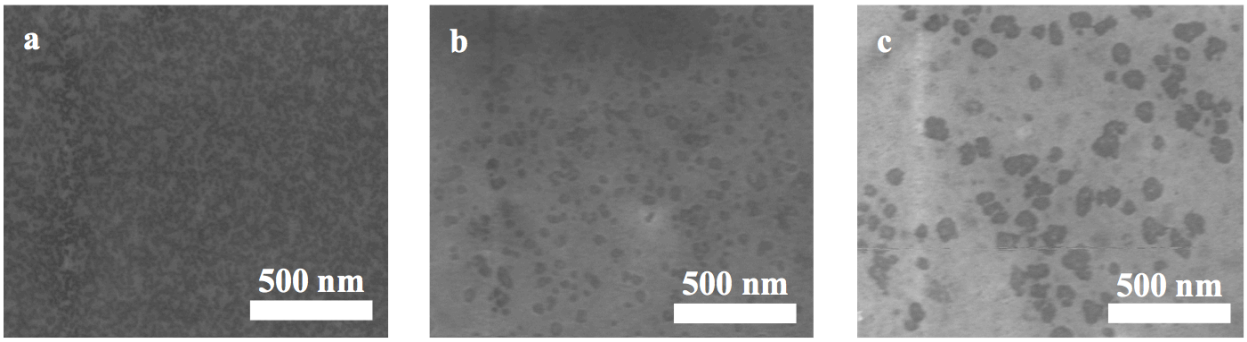

Figure 5.16. SEM images of Pt-foil post 4 V (vs $Mg^{2+/0}$) electrolysis from THF solutions composed of (a) 0.5 M PhMgCl and 0.125 M $Al(OPh)_3$, (b) 0.5 M PhMgCl and 0.25 M $MgCl_2$, and (c) 0.5 M PhMgCl.

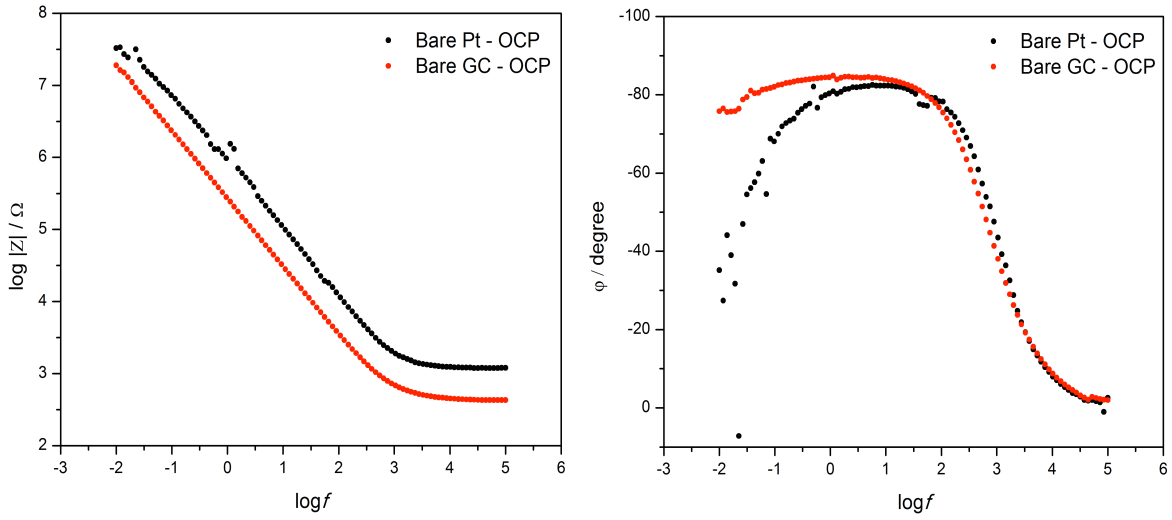

Figure 5.17. Bode Plots of bare Pt-disk (black, OCP 1.8 V vs $Mg^{2+/0}$) and bare glassy carbon disk (red, OCP 1.6 V vs $Mg^{2+/0}$) electrodes at their respective open circuit potentials.

likely changing. This is especially true at low frequencies with long data acquisition times. We note that the overall electrode impedance is lower from electrolyzed solutions of PhMgCl–$Al(OPh)_3$, which we surmise is the result of increased porosity of the generated films on the electrode surface (Figure 5.16). Qualitatively, the porosity of the adsorbed layer from the various THF solutions decreases in the order of: 0.5 M PhMgCl and 0.125 M $Al(OPh)_3$, 0.5 M PhMgCl

and 0.25 M $MgCl_2$, 0.5 M PhMgCl. Upon forming a passivation layer from either the PhMgCl–$Al(OPh)_3$, PhMgCl–$MgCl_2$, or PhMgCl in THF solutions, we observe a significant increase in electrode impedance, from ~10^3 Ω for bare platinum to ~10^5 Ω for the pretreated electrodes. This increased impedance is consistent with the reduced current densities observed with continued CV scans.

The same general trend is observed for impedance analysis when employing glassy carbon electrodes, with the notable exception that the overall impedance is lower in each case for the pretreated electrodes. The overall decrease in real and imaginary impedance for glassy carbon electrodes is the result of the increased resistance to charge transfer on a bare Pt-based electrode, compared to bare glassy carbon at their respective open-circuit potentials. Examining bare electrodes with an alternating voltage signal identical to their open-circuit potentials (Figure 5.17), glassy carbon shows lower overall impedance and increased capacitive behavior at low frequencies. Additionally, low frequency analysis is more sporadic with bare Pt electrode surfaces, consistent with developing a conductive black precipitate on the electrode surface when probing outside of the electrolyte stability window (>3.2 vs $Mg^{2+/0}$). While electrolyte decomposition does occur at similar potentials on glassy carbon, visual adsorption of this decomposition product is not observed.

5.4 Conclusion

While the early stages of development for rechargeable Mg-ion batteries have focused on improving the anodic stabilities of electrolyte solutions in order to reach compatibility with high voltage cathode materials, the possible decomposition products from these solutions have not been thoroughly investigated. With the strong adsorption of electron-insulating aromatic species,

resulting from the oxidation of anionic phenyl constituents, it appears advantageous to stray from phenyl-containing solutions. Although we note this phenomenon is not representative of every aromatic-based solution under the conditions presented, the possibility is still alarming. To avoid the complications presented by phenyl-based solutions, alkoxides, carboranyl salts, and amido-based electrolytes are all strong candidates moving forward.[12–14]

5.5 References

(1) Aurbach, D.; Suresh, G. S.; Levi, E.; Mitelman, A.; Mizrahi, O.; Chusid, O.; Brunelli, M. Progress in rechargeable magnesium battery technology *Adv. Mater.* **2007**, *19*, 4260–4267.

(2) Muldoon, J.; Bucur, C. B.; Oliver, A. G.; Zajicek, J.; Allred, G. D.; Boggess, W. C. Corrosion of magnesium electrolytes: chlorides – the culprit *Energy Environ. Sci.* **2013**, *6*, 482– 487.

(3) Nelson, E. G.; Brody, S. I.; Kampf, J. W.; Bartlett, B. M. A magnesium tetraphenylaluminate battery electrolyte exhibits a wide electrochemical potential window and reduces stainless steel corrosion *J. Mater. Chem. A* **2014**, *2*, 18194– 18198.

(4) Pour, N.; Gofer, Y.; Major, D. T.; Aurbach, D. Structural analysis of electrolyte solutions for rechargeable Mg batteries by stereoscopic means and DFT calculations *J. Am. Chem. Soc.* **2011**, *133*, 6270– 6278.

(5) Muldoon, J.; Bucur, C. B.; Gregory, T. Quest for nonaqueous multivalent secondary batteries: magnesium and beyond *Chem. Rev.* **2014**, *114*, 11683– 11720.

(6) Barile, C. J.; Barile, E. C.; Zavadil, K. R.; Nuzzo, R. G.; Gewirth, A. A. Electrolytic conditioning of a magnesium aluminum chloride complex for reversible magnesium deposition *J. Phys. Chem. C* **2014**, *118*, 27623– 27630.

(7) Liu, T.; Cox, J. T.; Hu, D.; Deng, X.; Hu, J.; Hu, M. Y.; Xiao, J.; Shao, Y.; Tang, K.; Liu, J. A fundamental study on the $[(\mu\text{-}Cl)_3Mg_2(THF)_6]^+$ dimer electrolytes for rechargeable Mg batteries *Chem. Commun.* **2015**, *51*, 2312– 2315.

(8) Lvovich, V. F. Impedance spectroscopy applications to electrochemical and dielectric phenomena; Wiley:NJ, **2012**.

(9) Mansfeld, F. Models for the impedance behavior of protective coatings and cases of localized corrosion *Electrochim. Acta* **1993**, *38*, 1891– 1897.

(10) Muller, J. T.; Urban, P. M.; Holderich, W. F. Impedance studies on direct methanol fuel cell anodes *J. Power Sources* **1999**, *84*, 157– 160.

(11) Song, J. Y.; Lee, H. H.; Wang, Y. Y.; Wan, C. C. Two- and three-electrode impedance spectroscopy of lithium-ion batteries *J. Power Sources* **2002**, *111*, 255– 267.

(12) Crowe, A. J.; Stringham, K. K.; Bartlett, B. M. Fluorinated alkoxide-based magnesium-ion battery electrolytes that demonstrate Li-ion-battery-like high anodic stability and solution conductivity *ACS Appl. Mater. Interfaces* **2016**, *8*, 23060– 23065.

(13) Kim, H. S.; Arthur, T. S.; Allred, G. D.; Zajicek, J.; Newman, J. G.; Rodnyansky, A. E.; Oliver, A. G.; Boggess, W. C.; Muldoon, J. Structure and compatibility of a magnesium electrolyte with a sulphur cathode *Nat. Commun.* **2011**, *2*, 427– 432.

(14) Tutusaus, O.; Mohtadi, R.; Arthur, T. S.; Mizuno, F.; Nelson, E. G.; Sevryugina, Y. V. An efficient halogen-free electrolyte for use in rechargeable magnesium batteries *Angew. Chem., Int. Ed.* **2015**, *54*, 7900– 7904.

Chapter 6

Conclusions and Potential Future Directions

Portions of this chapter have been published:

Crowe, A. J.; Bartlett, B. M. *J. Solid State Chem.* **2016**, *242*, 102–106.

6.1 Summary of Presented Work

The work presented in this thesis focuses on the development of non-aqueous electrolyte solutions for magnesium-ion batteries. Detailed synthesis, characterization, and analysis for novel electrolyte solutions are presented in Chapters 2 and 3. In both chapters, the reversible galvanostatic cycling of electrochemical cells employing the Chevrel-phase Mo_6S_8 and a magnesium metal anode is demonstrated. Chapter 4 probes further than the basic anodic stability and solution conductivity measurements, which are commonly featured in the reports of new electrolyte solutions. Specifically, we show through electrochemical impedance spectroscopy that during electrodeposition the largest resistance originates at the electrode–magnesium interface and the solution resistance itself, rather than the charge transfer between the interface and magnesium ions in solution for three previously reported magnesium-ion battery electrolyte solutions. The nature of electrolyte decomposition products that adhere to working electrodes from the 0.5 M PhMgCl and 0.125 M $Al(OPh)_3$ in THF electrolyte solution at positive (oxidizing) electrochemical potentials is assessed in Chapter 5. While considerable advances in the development and understanding of magnesium-ion battery electrolytes were discussed

throughout this thesis, several directions remain that may contribute the largest impact to the field remain and are described in the sections below.

6.2 Determination of Electrochemically Active Species

As presented in Chapter 3, through careful chronopotentiometric deposition coupled with ICP-AES analysis, the resulting Mg deposits from 1.2 M $((CF_3)_2CH_3)COMgCl$ and 0.2 M $AlCl_3$ in THF exceeds the theoretical change in Mg^{2+} concentration from Faraday's law considering a divalent cation (6.54 ppm measured compared to the theoretical value of 5.89 ppm). These results suggest that the presumed cationic species $[Mg_2(\mu\text{-}Cl)_3(THF)_6]^+$ contributes directly to Mg deposition. However, the discrepancy of recovered Mg deposits between electrolyte solutions after a constant current deposition suggests there may be additional chemical steps that lead to increased/decreased Faradaic efficiency. That is, Mg electrodeposition from these complex electrolyte solutions may not be as simple as a single 2 e^- transfer to an adsorbed species as shown within the purported mechanism[1]:

$$[Mg_2(\mu\text{-}Cl)_3\bullet 6(THF)]^+ + 3(THF) \rightleftharpoons [MgCl\bullet 5(THF)]^+ + [MgCl_2\bullet 4(THF)]$$

$$M(\text{electrode}) + [MgCl\bullet 5(THF)]^+ \longrightarrow [M{-}MgCl\bullet 5(THF)]^+_{ads}$$

$$[M{-}MgCl\bullet 5(THF)]^+_{ads} + 2e^- \longrightarrow [M{-}Mg]_{ads} + Cl^- + 5(THF)$$

$$[M{-}Mg]_{ads} \longrightarrow [M{-}Mg]_m$$

Specifically, a diminished Faradaic efficiency may be the result of a single e^- transfer to form a reduced intermediate that diffuses away from the electrode surface, resulting in a non-recoverable Mg^0 species. Additionally, reduction of non-magnesium-based species cannot be ignored within these complex solutions, since the reduction of Al^{3+} is possible at electrochemical potentials more negative than 0 V vs $Mg^{2+/0}$.[2,3] To investigate these possibilities, improved

transference number determination is possible after determining which species adsorb onto the electrode and/or are present at the solid-electrolyte interface using *in situ* Raman microscopy. Specifically, at potentials more negative than 0 V vs $Mg^{2+/0}$, what magnesium species beyond the commonly proposed $[Mg_2(\mu\text{-}Cl)_3(THF)_6]^+$ dimer are observed? In particular, is there experimental evidence of electrodeposition directly from $[Mg_2(\mu\text{-}Cl)_3(THF)_6]^+$? Furthermore, at potentials more positive than 0 V vs $Mg^{2+/0}$, what anions migrate to the working electrode to aid in the dissolution of previously deposited Mg? To guide this work, comparison to previously reported signal locations for measured Raman spectra of the 0.4 M PhMgCl and 0.2 M $AlCl_3$ in THF electrolyte solution will be of use.[4] The identity of any additional Raman features can be corroborated with vibrational mode analysis using density functional theory, as discussed within Chapter 3.

6.3 Magnesium Metal Conditioning to Pre-Generate a Mg^{2+} Permeable Solid-Electrolyte Interphase (SEI)

Although magnesium-ion batteries offer a two-fold increase in theoretical volumetric energy density, as well as improved safety when employing a pure metal anode, the chemistry associated with the divalent Mg^{2+} adds significant complexity that is not observed for lithium-ion predecessors. As mentioned in Chapter 1, attempts to employ a magnesium-based analog of electrolyte solutions currently employed within lithium-ion batteries has been unsuccessful due to the formation of a passivation layer in the presence of many common inorganic salts and solvents.[5] To circumvent this issue, alloy-based anodes composed of either bismuth or tin have been employed.[6–8] Within these cells, a conventional battery electrolyte composed of a commercially available Mg^{2+} salt such as magnesium bis(trifluoromethanesulfonimide) can

support reversible galvanostatic cycling. Unfortunately, bismuth (0.048 ppm) and tin (2.2 ppm) offer even lower elemental abundance in the earth's crust than their lithium (20 ppm) predecessor. Additionally, examples containing full cells (an intercalation cathode vs alloy anode) remain limited to the low voltage Chevrel phase-Mo_6S_8.

Recently, significant advances have been made in high-voltage cathode materials that show Mg^{2+} insertion/extraction within water-containing electrolytes. While oxide-based cathode materials demonstrate large electrode potentials for Mg^{2+} insertion/extraction, their affinity for the weakly polarizable Mg^{2+} cation results in slow ion diffusion. For this reason, water is often added to the electrolyte since water is a strong enough Lewis base to provide temporary solvation of Mg^{2+}, leading to enhanced diffusion kinetics of the highly charge dense ion.[9–11] However, aqueous solutions or even water-contaminated nonaqueous solutions will likely not be compatible with magnesium metal anodes due to the proclivity to react and form an insulating later:

$$Mg^0 + H_2O \rightarrow MgO + H_2$$

To take advantage of the high theoretical volumetric energy density and elemental abundance, an artificial ion-conductive interphase must be developed on the Mg metal surface. This approach may allow for use of water-containing electrolyte solutions, increasing the operating voltage of the electrochemical cell as oxide-based cathode materials are employed. However, an artificial solid-electrolyte interphase (SEI) must facilitate reversible deposition-dissolution of Mg at the anode with the simultaneous de-intercalation-intercalation processes

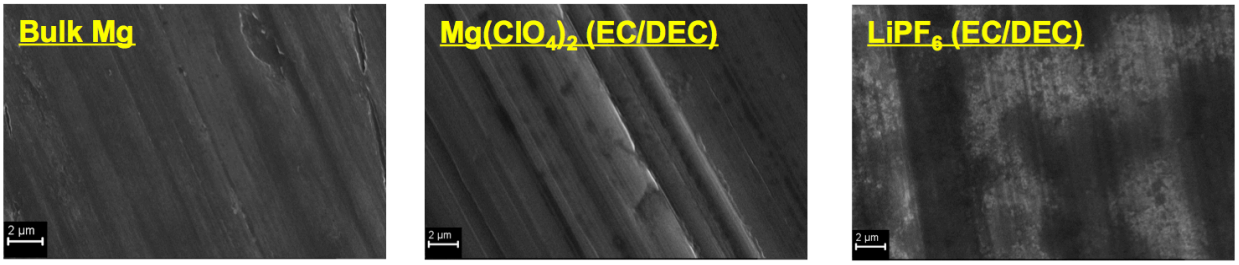

Figure 6.1. SEM images of Mg working electrodes prior to cycling (left), after cycling between -3 and 1.5 V (vs Pt) in 0.5 M $Mg(ClO_4)_2$ (middle) and -3.5 and 1 V (vs Pt) in 1 M $LiPF_6$ (right).

occurring at the cathode. A recent example employed a pyridine-based polyacrylonitrile matrix hybridized of multi-coordinated Mg^{2+} with $CF_3SO_3^-$. This pre-formed interphase enables the reversible cycling of a V_2O_5 cathode vs Mg anode in a water-containing, carbonate-based electrolyte.[12] However, the elevated temperatures (300 °C) in an Ar environment required for the interphase synthesis may render the manufacturing of large-scale energy storage systems difficult.

Proposed work to address these limitations includes investigating a Li-ion battery-based SEI pre-generated on a Mg metal anode. Recently, a SEI generated from a Li^+ containing electrolyte on ultrathin graphene electrodes shows efficient K^+ intercalation.[13] Preliminary studies for Mg^{2+} systems show that when a Mg working electrode is cycled in a ethylene carbonate-diethyl carbonate (50:50 v:v) solution (EC-DEC) of 1 M $LiPF_6$, texture similar a cycled Li-ion battery graphite anode results (Figure 6.1, right).[14] This is in stark contrast to the Mg electrode cycled within a solution of 0.5 M $Mg(ClO_4)_2$ in EC-DEC (Figure 6.1, middle), which is known to form a compact layer with significant passivating ability.[15]

To assess Mg^{2+} permeability, two Mg electrodes were cycled once as described above in either a $Mg(ClO_4)_2$ ($Mg_{Mg(ClO4)2}$) or $LiPF_6$-containing (Mg_{LiPF6}) EC-DEC-based

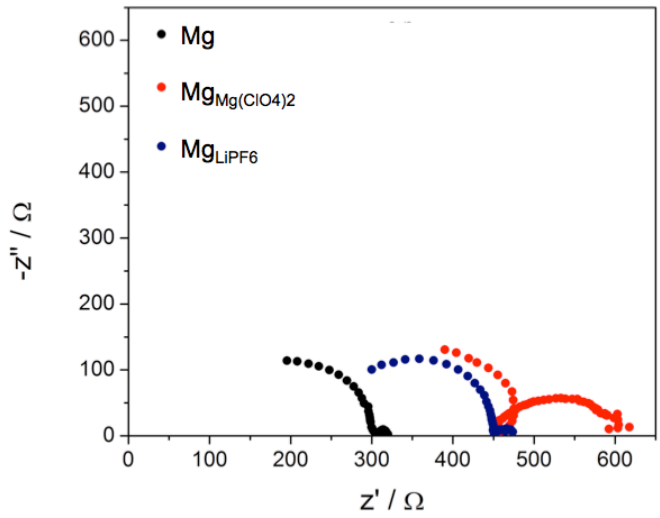

Figure 6.2. Nyquist plots of EIS results obtained from an untreated Mg (black), pretreated $Mg_{Mg(ClO4)2}$ (red), and pretreated Mg_{LiPF6} (blue) when poised about –1 V vs $Mg^{2+/0}$ within 0.4 M PhMgCl and 0.2 M $AlCl_3$ in THF; applied frequencies 1 MHz–1 Hz.

solution. Once an interphase was formed, they were immersed within 0.4 M PhMgCl and 0.2 M $AlCl_3$ in THF and poised about –1 V vs $Mg^{2+/0}$ during an electrochemical impedance spectroscopy experiment. In all cases, two approximate semi-circles result which were analyzed in a similar manner discussed in Chapter 4. That is, the first semicircle is attributed to a combination of charge-transfer resistance at an interface (R_{int}) and solution resistance (R_{sol}) and the second semicircle is attributed to charge transfer between the interface and solution (R_{ct}). As a control, a mechanically polished bulk Mg working electrode was also investigated. Shown in Figure 6.2, the largest impedance response results from the combination of $R_{sol} + R_{int}$. While the untreated electrode does not have a pre-generated SEI, Mg foil is covered in surface films even when freshly prepared within a glove box atmosphere.[15] As expected, when either pre-treated electrode is employed an increase in R_{int} is observed. However, a significant increase in R_{ct} is observed for $Mg_{Mg(ClO4)2}$, consistent with a $Mg(ClO_4)_2$/carbonate-based interphase being ion-insulating. In the case of Mg_{LiPF6}, R_{ct} appears effectively unchanged, which is promising for Mg

permeability. Future investigations must ensure the electrochemical process occurring at –1 V vs $Mg^{2+/0}$ within Figure 6.2 is magnesium electrodeposition occurring through the preformed interface. While these results only present initial studies employing a metal electrode pretreatment, consisting of a single cycle within a standard Li-ion battery electrolyte solution, future pretreatments may include various additives which have been previously identified for improving the stability of the *in situ* generated interphase within Li-based electrochemical cells.[16]

6.4 Summary and Concluding Remarks

The work presented within this thesis provides design principles that offer high anodic stability and solution conductivity for Lewis acid stabilized magnesium-ion electrolyte solutions. Additionally, the electrochemical characterization of the resulting electrode-electrolyte interface is presented. A thorough understanding of the structure and composition of active cationic species in solution has not been conclusively determined. In my opinion, determining which species migrate to the working electrode will allow for a more focused electrolyte design, allowing for omission of all non-participating (electrochemically) ions within these complex solutions. Despite the identification of magnesium-containing electrolyte solutions that display electrochemical stability and solution conductivities comparable to current lithium-ion standards, the corrosive nature of these solutions significantly hinders the possibility of application in high-voltage electrochemical cells. As a result, the continued investigation of artificial interphases on the magnesium metal anode surface aims to allow for the reversible cycling vs a metal oxide cathode in non-corrosive Mg^{2+} salts such as $Mg(TFSI)_2$, supported by the less volatile carbonate-

based solutions. In my opinion, exploration of these two directions will substantially impact to the field, bringing magnesium-ion battery technology closer to commercialization.

6.5 References

(1) Benmayza, A.; Ramanathan, M.; Arthur, T. S.; Matsui, M.; Mizuno, F.; Guo, J.; Glans, P. A.; Prakash, J. Effect of electrolytic properties of a magnesium organohaloaluminate electrolyte on magnesium deposition *J. Phys. Chem. C* **2013**, *117*, 26881– 26888.

(2) See, K. A.; Chapman, K. W.; Zhu, L.; Wiaderek, K. M.; Borkiewicz, O. J.; Barile, C. J.; Chupas, P. J.; Gewirth, A. A. The Interplay of Al and Mg speciation in advanced Mg battery electrolyte solutions *J. Am. Chem. Soc.* **2016**, *138*, 328– 337.

(3) Bachhav, M.; Hahn, N. T.; Zavadil, K. R.; Nelson, E. G.; Crowe, A. J.; Bartlett, B. M.; Chu, P.-W.; Araullo-Peters, V. J.; Marquis, E. A. Microstructure and chemistry of electrodeposited Mg films *J. Electrochem. Soc.* **2016**, *163*, D645– D650.

(4) Pour, N.; Gofer, Y.; Major, D. T.; Aurbach, D. Structural analysis of electrolyte solutions for rechargeable Mg batteries by stereoscopic means and DFT calculations *J. Am. Chem. Soc.* **2011**, *133*, 6270– 6278.

(5) Aurbach, D.; Gofer, Y.; Lu, Z.; Schechter, A.; Chusid, O.; Gizbar, H.; Cohen, Y.; Ashkenazi, V.; Moshkovich, M.; Turgeman, R.; Levi, E. A short review on the comparison between Li battery systems and rechargeable magnesium battery technology *J. Power Sources* **2001**, *97–98*, 28– 32.

(6) Singh, N.; Arthur, T. S.; Ling, C.; Matsui, M.; Mizuno, F. A high energy-density tin anode for rechargeable magnesium-ion batteries *Chem. Commun.* **2013**, *49*, 149– 151.

(7) Shao, Y.; Gu, M.; Li, X.; Nie, Z.; Zuo, P.; Li, G.; Liu, T.; Xiao, J.; Cheng, Y.; Wang, C.; Zhang, J.-G.; Liu, J. Highly reversible Mg insertion in nanostructured Bi for Mg ion batteries *Nano Lett.* **2014**, *14*, 255– 260.

(8) Arthur, T. S.; Singh, N.; Matsui, M. Electrodeposited Bi, Sb and $Bi_{1-x}Sb_x$ alloys as anodes for Mg-ion batteries *Electrochem. Commun.* **2012**, *16*, 103– 105.

(9) Spahr, M. E.; Novak, P.; Haas, O.; Nesper, R. Electrochemical insertion of lithium, sodium, and magnesium in molybdenum(VI) oxide *J. Power Sources* **1995**, *54*, 346– 351.

(10) Nam, K. W.; Kim, S.; Lee, S.; Salama, M.; Shterenberg, I.; Gofer, Y.; Kim, J.-S.; Yang, E.; Park, C. S.; Kim, J.-S.; Lee, S.-S.; Chang, W.-S.; Doo, S. G.; Jo, Y. N.; Jung, Y.;

Aurbach, D.; Choi, J. W. The high performance of crystal water containing manganese birnessite cathodes for magnesium batteries *Nano Lett.* **2015**, *15*, 4071– 4079.

(11) Novák, P.; Desilvestro, J. Electrochemical insertion of magnesium in metal oxides and sulfides from aprotic electrolytes *J. Electrochem. Soc.* **1993**, *140*(1) 140– 144.

(12) Son, S.-B.; Gao, T.; Harvey, S. P.; Steirer, K. X.; Stokes, A.; Norman, A.; Wang, C.; Cresce, A.; Xu, K.; Ban, C. An artificial interphase enables reversible magnesium chemistry in carbonate electrolytes *Nat. Chem.* **2018**, *10*, 532– 539.

(13) Hui, J.; Schorr, N. B.; Pakhira, S.; Qu, Z.; Mendoza-Cortes, J. L.; Rodríguez-López R. Achieving fast and efficient K^+ intercalation on ultrathin graphene electrodes modified by a Li^+ based solid-electrolyte interphase *J. Am. Chem. Soc.* **2018**, *140*(42), 13599– 13603.

(14) Verma, P.; Maire, P.; Novák, P. A review of the features and analyses of the solid electrolyte interphase in Li-ion batteries *Electrochim. Acta* **2010**, *55*, 6332– 6341.

(15) Lu, Z.; Schechter, A.; Moshkovich, M.; Aurbach, D. On the electrochemical behavior of magnesium electrodes in polar aprotic electrolyte solutions *J. Electroanal. Chem.* **1999**, *466*, 203– 217.

(16) Zhang, S. S. A review on electrolyte additives for lithium-ion batteries *J. Power Sources* **2006**, *162*, 1379– 1394.